NASA/TM–2010-216846

Aero-Heating of Shallow Cavities in Hypersonic Freestream Flow

Joel L. Everhart, Karen T. Berger, N. Ronald Merski, and William A. Wood
Langley Research Center, Hampton, Virginia

Kevin E. Hollingsworth
Aerospace Computing, Inc., Hampton, Virginia

Andrew J. Hyatt
Boeing Space Exploration, Houston, Texas

Ramadas K. Prabhu
Lockheed Martin Engineering & Sciences Company, Hampton, Virginia

September 2010

NASA STI Program . . . in Profile

Since its founding, NASA has been dedicated to the advancement of aeronautics and space science. The NASA scientific and technical information (STI) program plays a key part in helping NASA maintain this important role.

The NASA STI program operates under the auspices of the Agency Chief Information Officer. It collects, organizes, provides for archiving, and disseminates NASA's STI. The NASA STI program provides access to the NASA Aeronautics and Space Database and its public interface, the NASA Technical Report Server, thus providing one of the largest collections of aeronautical and space science STI in the world. Results are published in both non-NASA channels and by NASA in the NASA STI Report Series, which includes the following report types:

- TECHNICAL PUBLICATION. Reports of completed research or a major significant phase of research that present the results of NASA programs and include extensive data or theoretical analysis. Includes compilations of significant scientific and technical data and information deemed to be of continuing reference value. NASA counterpart of peer-reviewed formal professional papers, but having less stringent limitations on manuscript length and extent of graphic presentations.

- TECHNICAL MEMORANDUM. Scientific and technical findings that are preliminary or of specialized interest, e.g., quick release reports, working papers, and bibliographies that contain minimal annotation. Does not contain extensive analysis.

- CONTRACTOR REPORT. Scientific and technical findings by NASA-sponsored contractors and grantees.

- CONFERENCE PUBLICATION. Collected papers from scientific and technical conferences, symposia, seminars, or other meetings sponsored or co-sponsored by NASA.

- SPECIAL PUBLICATION. Scientific, technical, or historical information from NASA programs, projects, and missions, often concerned with subjects having substantial public interest.

- TECHNICAL TRANSLATION. English-language translations of foreign scientific and technical material pertinent to NASA's mission.

Specialized services also include creating custom thesauri, building customized databases, and organizing and publishing research results.

For more information about the NASA STI program, see the following:

- Access the NASA STI program home page at *http://www.sti.nasa.gov*

- E-mail your question via the Internet to help@sti.nasa.gov

- Fax your question to the NASA STI Help Desk at 443-757-5803

- Phone the NASA STI Help Desk at 443-757-5802

- Write to:
  NASA STI Help Desk
  NASA Center for AeroSpace Information
  7115 Standard Drive
  Hanover, MD 21076-1320

Aero-Heating of Shallow Cavities in Hypersonic Freestream Flow

Joel L. Everhart, Karen T. Berger, N. Ronald Merski, and William A. Wood
Langley Research Center, Hampton, Virginia

Kevin E. Hollingsworth
Aerospace Computing, Inc., Hampton, Virginia

Andrew J. Hyatt
Boeing Space Exploration, Houston, Texas

Ramadas K. Prabhu
Lockheed Martin Engineering & Sciences Company, Hampton, Virginia

September 2010

Table of Contents

List of Tables

List of Figures

Abstract

The purpose of these experiments and analysis was to augment the heating database and tools used for assessment of impact-induced shallow-cavity damage to the thermal protection system of the Space Shuttle Orbiter. The effect of length and depth on the local heating disturbance of rectangular cavities tested at hypersonic freestream conditions has been globally assessed using the two-color phosphor thermography method. These rapid-response experiments were conducted in the Langley 31-Inch Mach 10 Tunnel and were initiated immediately prior to the launch of STS-114, the initial flight in the Space Shuttle Return-To-Flight Program, and continued during the first week of the mission. Previously-designed and numerically-characterized blunted-nose baseline flat plates were used as the test surfaces. Three-dimensional computational predictions of the entire model geometry were used as a check on the design process and the two-dimensional flow assumptions used for the data analysis. The experimental boundary-layer-state conditions were inferred using the measured heating distributions on a no-cavity test article. Two test plates were developed, each containing 4 equally-spaced spanwise-distributed cavities. The first test plate contained cavities with a constant length-to-depth ratio of 8 with design point depth-to-boundary-layer-thickness ratios of 0.1, 0.2, 0.35, and 0.5. The second test plate contained cavities with a constant design point depth-to-boundary-layer-thickness ratio of 0.35 with length-to-depth ratios of 8, 12, 16, and 20. Cavity design parameters and the test condition matrix were established using the computational predictions. Preliminary results indicate that the floor-averaged Bump Factor (local heating rate nondimensionalized by upstream reference) at the tested conditions is approximately 0.3 with a standard deviation of 0.04 for laminar-in/laminar-out *conditions when the cavity length-to-boundary-layer thickness is between 2.5 and 10 and for cavities in the depth-to-boundary-layer-thickness range of 0.3 to 0.8. Over this same range of conditions and parameters, preliminary results also indicate that the maximum Bump Factor on the cavity centerline falls between 2.0 and 2.75, as long as the cavity-exit conditions remain laminar. Cavities with length-to-boundary-layer-thickness ratio less than 2.5 can not be easily classified with this approach and require further analysis.*

Introduction

The Final Report of the Columbia Accident Investigation Board (CAIB) was released in August 2003. The CAIB identified "*a breach in the Thermal Protection System of the leading edge of the left wing, caused by a piece of insulating foam ...*" as the probable event resulting in the loss of the Space Shuttle Columbia during flight STS-107 on February 1, 2003. Many possibilities were investigated prior to reaching this assessment, among them the creation of impact-induced cavities in the thermal protection system (TPS) tiles, resulting in local augmentation of the heating and eventual burn-through of the aluminum substructure. Though impact-induced damage to the tiles was eventually excluded as the cause, the CAIB recommended that NASA "*Develop, validate, and maintain physics-based computer models to*

evaluate Thermal Protection System damage from debris impacts. These tools should provide realistic and timely estimates of any impact damage from possible debris from any source that may ultimately impact the Orbiter. Establish impact damage thresholds that trigger responsive corrective action, such as on-orbit inspection and repair, when indicated." Langley Research Center, operating in concert with the Damage Assessment Aeroheating Team at Johnson Space Center, has provided for analysis and modeling an experimental cavity heating database consisting of nearly 775 wind tunnel runs[1,2,3], along with many computational simulations of this complex fluid dynamic and aeroheating environment. The predominance of these data and simulations are for non-surface-breaching, impact damage situations where near-zero pressure gradients occur, such as on the windward surface tile acreage. Additionally, most of the data were acquired in the Langley 20-Inch Mach 6 Wind Tunnel[4] for cavities with depth-to-boundary-layer-thickness ratios greater than 0.5 where the surface temperature rise is higher because the cavity disturbance is larger for these conditions, resulting in higher accuracy heating measurements. Recognizing the over-conservatism in the application of the initial heating data that could force unnecessary extra-vehicular activity (EVA, i.e., spacewalk) for repair in some scenarios, a rapid-response experiment addressing these concerns was planned and executed immediately prior to the launch of STS-114, the first Return-To-Flight (RTF) Space Shuttle mission, and testing continued through the first week of the mission. The experiment was conducted on an extremely compressed schedule, occurring over a two-week period from conception through model design, fabrication, testing, and data delivery. Because there was insufficient time to complete the normal review and certification processes required by the Space Shuttle Program, the experimental results were to be used initially for "guidance-only" in case damage occurred on launch.

The purpose of this report is to present wind test results focusing on the local heating augmentation of shallow cavities of depth-to-boundary-layer-thickness ratios less than 0.5. They were acquired in the Langley 31-Inch Mach 10 Tunnel[4] where the freestream temperatures are higher than those of the previous cavity flow studies conducted in the 20-Inch Mach 6 Tunnel. These higher freestream temperatures result in a greater surface temperature rise on the model, yielding lower data uncertainties. Based on the outcome of the analysis, allowances for these effects will be required in the engineering modeling tools[5] developed to assess potential heating augmentation resulting from damaged surfaces. Results from these analyses directly impact Damage Assessment Team decisions during a mission.

List of Symbols

C_p	pressure coefficient
h	heat transfer coefficient, $h=q/(H_{aw}-H_w)$, ($lbm/ft^2/s$)
L, W, H	cavity length, width, and depth (in)
M	Mach number
Mj	Wind tunnel test models, j=1, 2
p	pressure (psi)
q	surface heat transfer rate ($btu/ft^2/s$)
Rn	model reference nose radius (in)
Re	unit Reynolds number (1/ft)
Re_θ	momentum thickness Reynolds number
Sij	Shallow cavity designator with j=1,2,3,4 representing the cavity number on test model number i=1,2
s	distance along the streamline (ft)

T	temperature (R)
t	time (s)
U	velocity magnitude (ft/s)
x	axial distance from model leading edge (in)
y	spanwise distance from model centerline (in)
z	distance normal to x-y plane (in)
α	angle-of-attack (deg)
γ	ratio of specific heats
δ	boundary layer thickness (in)
θ	boundary layer momentum thickness (in)
Θ	Normalized temperature in heating equation
Λ	Normalized time in heating equation
ρ	density (lbm/ft^3)

Acronyms

BF	Bump Factor. Local heating normalized by upstream reference heating.
$BF_{floor\ avg}$	Bump Factor average on cavity floor.
BF_{CL}	maximum Bump Factor on the cavity end wall
CAIB	Columbia Accident Investigation Board
LAURA	Langley Aerothermodynamic Upwind Relaxation Algorithm
RTF	Return-to-Flight

Subscripts

avg	average
aw	adiabatic wall conditions
FR	stagnation point conditions from Fay-Riddell calculation for a hemisphere
local	local condition
ref	reference condition
t1	reservoir conditions
w	wall conditions
∞	freestream static conditions

Literature Assessment

The supersonic/hypersonic cavity flow literature (particularly that for laminar test conditions), while helpful, is particularly sparse on both the local and downstream effects of many fundamental flow parameters. Fletcher, et al.[6] published the survey paper "A Review of Heat Transfer in Separated and Reattached Flows" in 1970. Nestler[7] updated this survey with more recent work in 1985 in "The Effects of Surface Discontinuities on Convective Heat Transfer in Hypersonic Flow." Together, these papers include much of the existing, pertinent cavity flow literature. They cited theoretical models of cavity flow developed by Burggraf[8], Chapman[9], Carlson[10], Chang[11], and Lamb[12]; however, none of the theories adequately capture the physics of laminar and turbulent three-dimensional cavity flows as will be demonstrated via global surface heating distributions presented herein, though they offer a framework for experimental studies.

Numerical studies were conducted by Adams[13], Morgenstern and Chokani[14], Zhang, et al.[15], and more recently for the CAIB and the Shuttle RTF program by (for example) Wood, et al.[16] and Pulsonetti, et

al.[17]. The computational work presented by Wood uses the recently acquired RTF experimental open cavity results of References 2 and 3 for CFD comparison and validation of the numerical modeling, while Pulsonetti's work deals with flight traceability.

Experimentally, laminar two-dimensional flows were addressed by Galenter[18] and Nestler[19]; laminar axisymmetric flows were addressed by Nestler[20], Nicoll[21,22], and Wyborny, et al.[23]; and, laminar three-dimensional flows were examined by Cheatwood, et al.[24], Hahn[25], and Nestler[26]. The impact of a known, controlled pressure gradient on laminar-entry cavity heating was presented by Everhart, et al.[1]. Experimental studies with cavities tested in transitional boundary layers or to determine the onset of transition were presented by Charbonnier and Boerrigter[27], Boerrigter and Charbonnier[28], Hollis and Liechty[29-31], Larson and Keating[32], Liechty, et al.[33], and Rhudy and Magnan[34]. Turbulent two-dimensional experiments were presented by Charwat, et al.[35,36], Chin and Seban[37], Emery[38], Hunt[39], Lamb[40-42], Nestler[43-45,20], Shchukin, et al.[46], and Stallings and Wilcox[47]; turbulent axisymmetric experiments were conducted by Hunt[48] and Netterfield[49]; and turbulent three-dimensional experiments were published by Wilcox[50,51]. In general, the heating measurements were obtained with sparsely-spaced discrete sensors, the exception being those global phosphor thermography measurements presented by Cheatwood, et al., and Hollis and Liechty for circular cavities. Because of this spatial measurement sparseness, much of the three-dimensional nature of the surface heating profile is missed, as is in many cases the important peak heating value. While most of the idealized cavity geometries are rectangular with a flat bottom profile (a few have an arc bottom), the paper by Emery is of particular significance because heating profiles are presented for models with notched, cutback profile geometries that may be more representative of potential impact damage conditions. Two papers by Blair and Stallings[52] and Stallings, et al.[53] are significant because they present oil flow visualizations in and around the cavity and vapor screen visualizations of the cavity crossflow plane, clearly showing the growth and development of the cavity vortex structure. Gaps are an important class of cavities that have a length-to-depth ratio less than 1. Gaps have been examined by Coats, et al.[54], Johnson[55], Throckmorton[56], and Weinstein, et al.[57].

As demonstrated above, many cavity research studies are available in the published literature. However, until recently there existed only a limited amount of laminar flow experimental data for evaluating heating effects in supersonic/hypersonic cavities, and most of the existing parametric variations and correlations were developed using turbulent heating measurements. Further, turbulent methods have typically been used for thermal assessments of damage on the Space Shuttle, even though much of the re-entry trajectory provides laminar edge conditions on the vehicle. The use of these turbulent methods may be overly conservative and restrictive for thermal assessment of shuttle tile damage for the laminar conditions.

Supersonic/Hypersonic Cavity Flow Physics

Based on the literature survey, the following overview of cavity flow physics is presented. Length- to-depth ratio is typically used to distinguish between and classify different cavity flow regimes, as depicted in Figure 1. Very short or deep cavities with *L/H<1* are known as gaps. In this case, shearing induced by the main stream flow causes the development of a column of counter-rotating vortices within the gap numbering approximately *H/L*. Alternating hot spots occur in the gap when the vortices directionally align and impinge on the sidewall. Two stable flow conditions exist for cavities with length *L/H>1*. The first is a short cavity of length *1≤L/H≤10*, known as an open cavity. The mainstream flow does not enter the cavity directly, though there may be some mass interchange with the low-energy vortical flow inside the cavity. In this case, the cavity pressure is typically above the ambient and climbs to a peak at the downstream lip. The heating drops significantly below the undisturbed value and rises slowly to a peak on

the downstream lip. The other stable solution is a long cavity, known as a closed cavity, with length *L/H>14*. In this case, three distinct flows may develop if the cavity is long enough. First, the upstream flow is able to turn into the cavity and impinge on the floor, creating an aft-facing-step flow field. Next, a boundary layer on the floor may develop and recover to the ambient level outside the cavity. Finally, as the flow approaches the end wall it will turn outward and create a forward-facing-step flow field. For long, deep cavities, the pressure gradients may be severe where the flow turns and strong expansion and shock waves will be generated. Viscous shearing generated by this flow turning will augment the heating to levels significantly higher than the ambient levels on both the cavity floor and the end wall. The pressure in these long cavities will decrease below the ambient and steadily increase downstream, reaching large values of over-pressure behind the shocks. Vortices will develop on the cavity sidewalls as the flow expands around the corner into the cavity and on the floor after flow impingement, further augmenting the heating, which may extend laterally around the cavity in the most severe cases. These vortices will interact with the cavity end wall and spill into the downstream region beyond the cavity. Given laminar inflow, analysis of the heating profiles indicates that most any type of outflow may occur, depending on the cavity and its environmental state. The in-cavity flow may remain laminar, become transitional, or transition to fully turbulent flow; the downstream possibilities are equally varied and are currently the subject of extensive analysis and testing[58] in support of Shuttle RTF. Cavities for the range *10≤L/H≤14* are typically unsteady as the flow alternates between the two bounding conditions; these are known as transitional cavities.

Boundaries between different cavity flow regimes are nominal, at best. For example, *L/H* values have been measured from 9 to 11 as the upper limit for open cavities and from 12 to 15 as the lower limit for closed cavity flow. These limits should therefore be taken only as a guide. Also, it is important to note that most of the reported cavity data were acquired in air ($\gamma = 1.4$) with some in helium ($\gamma = 1.67$). Since turning angle is a function of both Mach number and γ, conceivably, open/closed cavity boundaries will vary during re-entry as vehicle boundary layer edge conditions change. At present, experimental data are insufficient to estimate the strength of this effect on the aeroheating.

Establishing the Testing Environment

When few (if any) direct measurements of the cavity geometry are available and when the exact location of the cavity (implying local flow conditions) is unknown, defining the heating environment of an Orbiter damage-scenario cavity presents a significant challenge. Many possible variables and parameters exist. Following the literature, the gross geometric parameter space includes: length (L), width (W), and depth (H), and planform, cross-sectional, and profile variations. Sidewall and upstream end-wall entry angles may play an important role on the flow expansion into the cavity, while sidewall and end-wall exit angles may affect recompression on the downstream wall and further expansion around the end-wall corner – all parameters having a direct influence on the heating. The depth distribution along the cavity profile may potentially affect how or if the flow enters the cavity and impinges on the floor. The impact of roughness caused by irregular surfaces, protuberances, gap fillers between tiles (present or missing), embedded objects, etc. in and upstream of the cavity is unknown, but the roughness may significantly impact the shear layer/boundary layer transition process[59]. Local flow conditions and parameters include boundary layer thickness (δ), momentum thickness (θ), edge Mach number (M_e), momentum thickness Reynolds number (Re_θ), stream direction with respect to the cavity major axis, chemistry effects reflected in the ratio of specific heats (γ), wall temperature ratio (T_w/T_{aw}), boundary layer state (laminar, transitional, or turbulent) entering/leaving the cavity, and pressure gradient.

Shuttle Orbiter windward surface flow conditions are presented in graphical format in Reference 60.

Recently, surface flow conditions for the Shuttle Orbiter[61] have been computed using the DPLR code[62] for the STS-107 re-entry trajectory. The range of surface edge flow conditions from these sources over the windward acreage at Mach 18 where the pressure gradients are small (nominally zero) are presented in Table 1.

Given the infinite number of potential geometric variations for impact damage, the Shuttle Damage Assessment Team has defined a simplified cavity representation. This rectangular geometry (called the "shoebox" geometry due to its shape) consists of a flat bottom bounded by straight sides and end walls. Entry, exit, and sidewall angles are prescribed for the general case. However, for the sake of simplicity, vertical sides and ends are used for the present designs. According to existing literature, the governing parameters for a cavity are the length-to-depth ratio L/H, and the depth-to-boundary-layer-thickness ratio H/δ. Lack of detailed width-effect information in the literature leads to the decision to scale the width by the depth W/H.

Two different surveys of the shallow-cavity depth effect are desired. The nondimensional design conditions for the first are a variation of nondimensional depth H/δ at constant nondimensional length L/H; the design conditions for the second is a variation of length L/H at constant depth H/δ. For the first variation, the non-dimensional length of the cavity is chosen as 8 to ensure an open cavity flow field and to allow for dimensionally deeper cavities and physically longer cavities to enhance the optical access. Four cavities of non-dimensional depths of 0.1, 0.2, 0.35, and 0.5 were selected. For the second variation, a non-dimensional depth of 0.35 was selected with non-dimensional lengths of 8, 12, 16, and 20. Theoretically, this length variation will yield an open cavity, a transitional cavity, and two closed cavity flow fields, respectively. A cavity design width W/H of 3.6 was selected for all cavities to enhance the optical access.

Experiment Design

This section outlines the experiment design process. First, the design philosophy is presented, along with physical constraints imposed on the process. This is followed by the characterization of the model test surface using two-dimensional CFD simulations. Finally, the cavity design is generated, yielding the corresponding, available test space for these models.

Design Philosophy and Constraints

A flat-plate geometry where dC_p/dx is approximately 0 was selected for installation of the cavities, allowing consistency with existing data. A tunnel-installation schematic of the model is presented in Figure 2 that will be further discussed in the models section. A blunted nose model was required to reduce the edge Mach numbers to target values at smaller angles of attack, thus minimizing the possibility of partial or complete tunnel-flow blockage[63]. Several different leading-edge-radius nose values were evaluated, and the variation of the surface flow properties of the plate were mapped for each as a function of model test conditions and attitude (i.e. Pt_1, Tt_1, α, M_e, and Re_θ). Based on an analysis of these computations, a nose radius, R_n, of 0.125 inches was selected. For this nose, the actual leading edge point will occur at 0.8245 inches downstream of the virtual origin defined at the x=0 inch station. The shoulder intersection between the nose and the beginning of the flat upper surface occurs at the 0.9495-inch station. According to Micol[4], the 31-Inch Mach 10 Tunnel test core is safely 10 inches at the smallest freestream Reynolds number. Therefore, a model width of 10 inches was selected to minimize possible interference of side-edge vortices on the model test region and to minimize spanwise flow-gradient effects across the model. With proper mounting, models as long as 30 inches can be injected through the tunnel sidewall.

Model length was defined during the design as nominally 20 inches. Finally, the cavity test location on the plate, X_{cav}, was established at the 8-inch station, downstream of the rapidly varying pressure gradients that occur as flow expands over the leading edge. This location was selected so that the desired scaled cavity with prescribed H/δ, W/H, and L/H yielded reasonable dimensions in geometric space (H, W, L) for measurement resolution. Since computational solutions were used to design the test articles, the available test domain was developed naturally as a part of the design process.

Two-Dimensional Surface Modeling

Two-dimensional baseline surface characterization was performed using the LAURA computational fluid dynamics code[64,65]. Best practices as defined in Ref. 66 were used to define the computational grid. Solutions for the flat surface were computed for leading edge nose radius values of 0.0625, 0.1250, and 0.1875 inches for a range of stream conditions covering tunnel Re = 0.5 x10^6, 1.0 x10^6, 1.8 x10^6, and 2.0x10^6 per foot at anticipated model angles of attack, α, ranging from -25 to 10 degrees. Boundary layer thickness, δ, was determined at the location where the enthalpy ratio had achieved 99.5 percent of the freestream value. As presented in Ref. 67, boundary layer thickness values computed with the LAURA code are typically 2-4% lower than experiment with a 10% standard deviation. Most of the expected initial large change in the pressure was completed by the 5-inch station for all conditions, particularly for the expanding flow conditions that occur around the test surface for positive angles of attack, though some slight gradient effects remain as the boundary layer continued to grow on the plate. The smallest nose radius was not selected because of fabrication concerns. Overall, relatively small differences were observed when comparing the effects of the 0.1250-inch nose radius to the 0.1875-inch nose radius on the boundary layer edge conditions. For consistency with other experiments, the 0.1250-inch nose was selected. Sample surface flow computations for the flat surface are presented in Figure 3.

Test Condition Selection and Cavity Design

The flow conditions at the location of the leading edge of the cavity are needed to determine the final cavity dimensions. The 8-inch station was selected as the cavity leading edge position based on the following factors: 1) the constant pressure gradient location begins at approximately 5 inches (see Figure 2), 2) thicker boundary layers allow larger cavities, 3) the target-condition requirement for the magnitude and range of Re_θ, and 4) the downstream narrowing of the plate side-edge vortices. Test conditions at this location were interpolated from the CFD surface flow distributions, and they are presented in terms of performance charts for the flat surfaces in Figure 4. In this figure, M_e, Re_θ, δ, and θ are plotted versus P_{T1} for various angles of attack. The effect of T_{T1} for the range of conditions considered was second order; therefore, it was neglected when determining the boundary layer edge properties. For each test surface, three nominal edge Mach number conditions (2.25, 2.50, and 2.85) covering the target range were specified. At each edge Mach number condition, the available Re_θ space was determined from the curves, along with the α required to achieve these entry conditions; then, the corresponding δ and θ were determined to help scale the cavities. The boundary layer edge conditions were re-evaluated using the actual test conditions, and these conditions were used for final data reduction and post-test analysis. The resulting boundary layer thickness at this condition was used as the scaling factor for the cavity depth, H/δ.

Experimental Method

The experimental methods are presented, beginning with a description of the test facility and nominal

tunnel flow conditions. This is followed by a description of the model fabrication process, a discussion of the phosphor coating used for making the heating measurements, and the model mounting. An overview of the phosphor data system used to acquire the global heating measurements is next presented, followed by a discussion of the post-test data mapping and scaling.

Facility

The 31-Inch Mach 10 Air Tunnel was selected as the test facility because the higher surface temperature rise during a run would provide lower uncertainties in heat transfer measurements[68]. This is a blowdown facility in which heated, filtered air is used as the test gas. The tunnel has a square, contoured nozzle, which opens into a 31-inch square test section. Models are supported on a hydraulically operated, sidewall-mounted injection system that can transfer a model from the sealed isolation box outside the flow to the tunnel center-line in less than 1.5 seconds. Tunnel run times of approximately 60 seconds can be achieved, but typical heating studies require only a few seconds. The nominal reservoir conditions are stagnation pressures of 150 psi to 1450 psi at stagnation temperatures of about 1825°R. These reservoir conditions very nearly produce perfect gas ($\gamma = 1.4$) freestream flows with a Mach number of approximately 10 and Reynolds numbers of 0.2×10^6/ft to 2.2×10^6/ft. Nominal flow conditions are provided in Table 2 and a detailed description of this facility is presented by Micol[14].

Models

The general manufacturing process for ceramic test articles is described in Buck, et al.[69]. Specific changes to this process for previous cavity heating experiments[2,3] are described in Buck, et al.[70]. In this later manufacturing method, a rapid prototyping stereolithography (SLA) system at NASA Langley Research Center was used to make a resin mold pattern for casting cavities in flat 4-inch wide by 18-inch long ceramic insert models. These ceramic inserts were then installed in a 10-inch wide by 28-inch long steel flat-plate model for testing.

The present experiment further improves this manufacturing process by eliminating the insert requirement. Here, the flat plate models were nominally 10-inches wide by 20-inches long and they were cast as a single piece to remove the step and gap mounting problems experienced with the previous method. Referring to Figure 2, all models had a 0.125-inch radius nose with a 15° aft-swept wedge on the lower nose surface. As schematically shown, the ceramic castings were then bonded to an aluminum backing plate that is at 0° incidence relative to tunnel centerline for the flat plate.

Using the previously described cavity design process, three ceramic models were developed:

1) a baseline flat plate model with no cavities;
2) a model with four spanwise-distributed L/H=8 cavities with design-point depths of H/δ of 0.1, 0.2, 0.35, and 0.5; and
3) a model with four spanwise-distributed design-point-depth H/δ=0.35 cavities of lengths L/H of 8, 12, 16, and 20.

The models (shown schematically in Figure 5) were laser-ablated at a longitudinal location of x=8 inches, yielding the as-built cavity dimensions and spanwise location as presented in Table 3. Shallow-cavity model M1 represented the depth variation at constant design length L/H=8, while shallow-cavity model M2 represented the length variation at constant design depth H/δ=0.35. Also noted in Figure 5 is the nomenclature used for cavity identification. Here, each cavity is identified as Sij where i is 1 or 2,

8

depending on the model, and j is 1 to 4, depending on the cavity. For example, S23 represents model 2 cavity 3. Note that cavity S11 is on the starboard side of M1 and that S21 is on the port side of M2. The common-geometry L/H=8, H/δ=0.35 reference cavities (S13 and S21) are highlighted in black.

Both models were coated with a 27μm[68] thick mixture of phosphors suspended in a silica-based colloidal binder and sent to quality assurance for measurement and application of small circular locating markers, known as fiducial marks. These fiducial marks aid in data reduction and model orientation, and they can be seen in the run images as dark dots. Even though fiducial marks do not influence the flow over the model surface, they will influence the local heating measurement because the ink used in the process will wick into the phosphor coating over a small circular region about the application point and locally change the calibration. Their influence on the data, notably in line cuts passing through them, is to produce a very short, very sharp-peaked sinusoidal signature covering the diameter of the marking.

When mounted in the tunnel, the aluminum backing plate was attached to a 0° spacer block surface used to position the model on tunnel centerline and align the model to zero incidence. Finally, this entire assembly was attached from the leeward side to an existing model support strut and mounted to the tunnel sidewall injection plate. An offset angle wedge is placed under the strut base when required to extend the angle testing range of the model. A picture of the model mounted in the 31-Inch Mach 10 Tunnel with the phosphor thermography camera and lighting system is given in Figure 6.

Thermographic Phosphor Measurement System

Global surface heating distributions were calculated using the two-color, relative-intensity, phosphor-thermography aeroheating measurement method[71]. This is the standard method for obtaining aeroheating data in NASA Langley's hypersonic wind tunnels, and it can be used to identify the surface heating effects of complex three-dimensional flow phenomena, which are difficult to examine using conventional discrete-sensor methods. With this method, ceramic wind tunnel models are coated with phosphor crystals that fluoresce in the red and green regions of the visible light spectrum when illuminated by ultraviolet (UV) light. During a wind tunnel run, the phosphor-coated model is exposed to the heated flow of the tunnel, and the resulting changes in fluorescence intensity of the model are recorded and digitized through a 640 by 480 resolution color-CCD (charge coupled device) camera and a state-of-the-art video acquisition system. The fluorescence intensity is dependent on both the intensity of the incident UV light and the local model surface temperature. The UV dependence is removed by taking the ratio of the green to red intensity images, from which surface temperature distributions are determined through prior calibrations. Images are acquired before the wind tunnel run and after injection of the model to the tunnel centerline during a run.

Data Reduction

Global mappings of the surface temperature obtained with the thermographic phosphor data acquisition system were reduced to surface heating distributions using the IHEAT data reduction software[71]. In this method, phosphor images are acquired shortly after injection of the model to the tunnel centerline. With this software, temperature images acquired through the run are used to obtain heat transfer images. This is done by applying one-dimensional, semi-infinite-solid heat conduction theory assuming a constant heat-transfer coefficient, and by making empirical corrections to account for temperature changes in model substrate thermal properties. The results are presented in terms of a non-dimensional heat transfer coefficient ratio, h/h_{ref}, where h_{ref} is generally taken as h_{FR}, the theoretical stagnation-point heating computed with the Fay-Riddell[72] theory. For this experiment, h_{FR} was computed

using a 0.125-inch radius sphere (the test model nose radius) and a reference stagnation temperature of 540ºR. At this point, IHEAT was used to extract preliminary analysis data along lines from the two-dimensional heating images. Also, these images were mapped onto a three- dimensional representation of the test article using IHEAT's MAP3D photogrammetry program[68] for further global analysis.

Data for this experiment were translated such that the leading edge of the cavity is at x=0. The (x, y, z) data were then scaled to (x/H, y/H, z/δ) using the measured cavity depth and the computed boundary layer thickness. This yields a scaled-geometry cavity of (L/H, W/H, H/δ). Note again that the boundary layer edge conditions for each run are determined from the LAURA computations for matching tunnel and model conditions.

The impact of the cavity on the local undisturbed environment was assessed by converting the local heating data to heating augmentation or bump factor (BF) format by normalizing h_{local}/h_{ref} by a reference-location average heating h_{avg}/h_{ref}, yielding $BF=h_{local}/h_{avg}$. The reference-location heating on the baseline models (no cavity) is computed over a plate-centered strip located $-2 \leq x/\delta \leq 0$ by $-2 \leq y/\delta \leq 2$. (Note that $x/\delta = 0$ corresponds to the location of the cavity leading edge when cavities are present, since the coordinates have been translated.) In this format, BF=1 is the nominal undisturbed condition for a flat plate. For analysis consistency and to avoid the heating peak due to expansion into the cavity at the upstream edge, (h_{avg}/h_{ref}) is computed ahead of each cavity over an area two cavity depths long by one cavity width wide, and this region is located at $-3 \leq x/H \leq -1$ by $-0.5 \leq y/H \leq -0.5$.

Presentation of Test Data

The as-run test matrix for the baseline flat plate model, including tunnel conditions, is presented in Table 4. These runs were obtained during Test 406 following the acquisition of the shallow cavity test data during Test 404. The shallow cavity test used two flat plates, each containing 4 discrete cavities. The test matrix for Shallow Cavity Model 1 containing a depth sweep at constant length is presented in Table 5, while the test matrix for Shallow Cavity Model 2 containing a length sweep at constant depth is presented in Table 6. Computationally-generated boundary layer edge conditions and parameters at station x=8 inches (the cavity entrance) are presented in Table 7. This table provides the computed cavity entry conditions M_e, Re_θ, Re_θ/M_e, δ, and θ, as well as the cavity depth, width, and length normalized by the boundary layer thickness. Three types of runs were made for each cavity plate. The first type is a global heating run with the phosphor camera set to view the entire plate; the second type is a view of the plate with the camera capturing only the top two cavities; and, the third type is a view of the plate with the camera capturing only the bottom two cavities. Constraints on the cavity views were that upstream and downstream fiducials must be in each image for reference.

Bump Factor images for the baseline runs acquired during Test 406 are presented in Figure 7. The data represented in these images provide the undisturbed heating profile of the entire plate, allowing an assessment of the flow uniformity and the boundary layer state. The global heating images for the cavity model plates are presented in Figure 8 and Figure 9. These images allow an assessment of the extent of the cavity flow field interactions over the plate surface. Because most cavities were very small, these global image data were of insufficient resolution for mapping; therefore, they are presented in terms of h/h_{FR}. Also noted on the first image of each figure is the cavity identifier (ex. S21 on Figure 8a). This nomenclature was previously discussed in the Models section. Finally, the local, mapped, scaled Bump Factor distributions for each cavity are presented in Figure 10 through Figure 17. Here, x/δ is referenced from the cavity-entrance location using local conditions. The first image in Figure 10 identifies the location of the cavity and the fiducial marks for reference for all other figures.

Uncertainty Analysis

Merski[68] published the uncertainties for the phosphor thermography method as a whole in 2001. A more quantitative understanding of the uncertainty levels for this experiment were obtained by adding phosphor heat-transfer bump-factor uncertainty algorithms to the MAP3D code, resulting in global uncertainty surface maps similar to the three-dimensional heat transfer maps. The process is outlined below.

The solution of the heat conduction equation (i.e. the data reduction equation) used in the IHEAT code is given by

$$\frac{\Theta}{H_{aw}\left(T_w/H_w - T_{init}\right)} = 1 - e^{\Lambda^2} erfc(\Lambda)$$

where

$$\Theta(x,y,t) = T(x,y,t) - T(x,y,0) = T(x,y,t) - T_{init} \quad \text{and} \quad \Lambda = \frac{h\left(H_{aw}/T_w\right)}{\beta}$$

h is the convective heat transfer coefficient, H_{aw} is the adiabatic wall enthalpy, H_w is the wall enthalpy, T_w is the corresponding wall temperature, and t is the effective time of data acquisition. β is the thermal product of the substrate materials and it is equal to the square root of the product of the material density, specific heat, and thermal conductivity.

Bias and precision uncertainty values for the time, temperature, and thermal product used in the data reduction equation were developed at the 95 percent confidence level and they are given in Table 8. The 5.9% bias uncertainty quoted there for β is the maximum deviation observed across the temperature range. Uncertainties for each free parameter in the heat transfer coefficient resulting from the variation in each parameter were determined by individually inserting the parameter uncertainty range endpoints into the data reduction equation. The bias uncertainty, B, and the precision uncertainty, P, for the heat transfer coefficient were determined by obtaining the root-sum-square (RSS) from each of the component uncertainties using

$$B = \left(\sum_j B_j^2\right)^{\frac{1}{2}} \quad \text{and} \quad P = \left(\sum_j P_j^2\right)^{\frac{1}{2}}$$

where j is the number of component uncertainties. Total uncertainties are obtained by taking the RSS of the bias and precision uncertainties. Bias and total uncertainties of the heat transfer coefficients are determined at every pixel point imaged on the model.

Bump factors extracted from the mappings were used in two ways: 1) as line cuts when selecting specific data, and 2) as regions of interest over which all of the data were averaged. In the first case, the total uncertainties are applicable and in the latter, bias uncertainties are applicable. Precision uncertainties are removed during averaging, since they are primarily due to random pixel scatter. Accordingly, the average heat transfer coefficient h_{avg} used to compute bump factors was assumed to have only a bias

uncertainty. Typically, as shown in Ref. 73, total uncertainties in the bump factors are determined using

$$\left(\frac{U_{BF}}{BF} \right)^2 = \left(\frac{U_{h_{local}}}{h_{local}} \right)^2 + \left(\frac{U_{h_{avg}}}{h_{avg}} \right)^2$$

For nominally flat models of this type, very low heating rates are obtained during a run and the resulting uncertainty calculations were initially very high. Yet, comparisons of line cuts were more consistent than the uncertainty analysis seemed to suggest. While conservatism is important, excessive conservatism is undesirable. Therefore, the phosphor temperature lookup table data were re-examined and it was determined that since there was minimal variation of incident UV intensities on the models during the tunnel runs, and because of the low heating measurements, the data were typically confined to one very small segment of the temperature range. Thus, the bias uncertainties for the data used in calculating h_{local} and h_{avg} were unidirectional and determinate. Therefore, the bias uncertainties in h_{local} had to be excluded from the bias uncertainties in h_{avg} when computing bias uncertainties for the bump factors. Similarly, total uncertainties in bump factors were then obtained simply by taking the RSS of the bias and precision uncertainties in h_{avg} and by excluding the bias uncertainties in h_{local}.

Representative bias uncertainties for cavity S12 (Run 03) are shown in Figure 18a, corresponding total uncertainties are shown in Figure 18b. Similarly, uncertainties for cavity S14 are shown in Figure 19. These open cavity flows represent some of the more challenging measurement configurations from an accuracy standpoint because the flow does not directly enter the cavity, resulting in a very small floor temperature rise relative to the pre-run condition. Here, total and bias uncertainties are typically less than 10% over the plate surface. In the cavity where the lowest temperatures are experienced, the bias uncertainties are about 10%, while the total uncertainties approach 20%. A closed condition is presented for cavity S24 for Run 28 in Figure 20. As expected, the temperature rise is generally greater, resulting in lower bias uncertainties (3-4 percent or lower) with the exception of the low temperature regions on the cavity floor. Total uncertainties are in the 10-20 percent range.

Results

The objective of the present report is to provide a data set focused on the heating augmentation in the near field region of impact-induced shallow cavities. The results presented in this section represent a preliminary evaluation of the test data, recognizing that more extensive analysis and certification must be conducted prior to its inclusion in the engineering tools developed for damage assessment during flight operations. Two metrics are used. The first is the average bump factor on the entire cavity floor obtained by using the Region-of-Interest tool contained in the IHEAT data reduction program. The second is the endwall maximum bump factor obtained from centerline data slices through the cavity, again from the IHEAT program. A tabulation of these metrics is presented for each run in Table 9.

Considering the open (L/H=8) cavity data presented first in Figure 21a, the $BF_{floor\ avg}$ is plotted as a function of H/δ. The results from each cavity are color coded and a line representing a least-squares fit is provided. Length L/H=8 cavity data from Model 1 (S13) are compared with L/H=8 cavity data from Model 2 (S21) as a consistency check on the manufacturing, measurement, and data reduction processes. An exceptionally good comparison is demonstrated by the overlap of most of the discrete data at matching conditions and by the line-fit results. Recall that each test point generates data from two cavities, either S11 and S12 or S13 and S14, and that two runs are required to generate matching entry conditions for all four cavities on a single plate. Also, recall that the data for each cavity were acquired

over a wide range of M_e and Re_θ and, as shown, that overlapping depth conditions were acquired for adjacent cavities. Prior to the test, it was anticipated that $BF_{floor\,avg}$ would regularly vary from 1 at zero depth to some asymptotically realized average value at larger depths. This has not occurred. The cavity-floor average data from each cavity are constant with depth and different cavities tested at the same depth generate a different constant. It is appropriate to note that no correlation was found when plotting this metric versus other flow parameters, including H/θ, W/H, Re, Re_θ, and Re_δ. A consistent stratification in H/δ (longitudinal shift) for each cavity was found when the data were identified according to M_e; however, further analysis is required for the inclusion of this effect in a correlation.

The variation of $BF_{floor\,avg}$ for different L/H cavities is plotted as a function of H/δ in Figure 21b. These data exhibit the expected variation in that long cavities (L/H>14) allow the hotter external flow to enter, thereby increasing the heating. $BF_{floor\,avg}$ values for the open cavities cluster around 0.3, while values for the closed cavities cluster near 0.5. Data from cavity S23 (L/H=16) are clearly transitional, switching from the open to the closed $BF_{floor\,avg}$ levels. While not definitive and only after examining the behavior of S23, data from cavity S22 appear to be at least partially transitional. For comparison, cavity S13 from Model 1 and cavity S21 from Model 2 again generate nearly the same results, establishing consistency as previously discussed for Figure 21a.

Poor correlation of the $BF_{floor\,avg}$ data was demonstrated when plotted versus H/δ and L/H (not shown). However, the correlation was much improved when the cavity floor averaged data were plotted as a function of viscous length parameter L/δ, which is equivalent to $(L/H)(H/\delta)$, as shown in Figure 22. This presentation implies that $BF_{floor\,avg}$=0.291 with a standard deviation of 0.041 for fully-laminar flow conditions (i.e. laminar-in/laminar-out) conditions when $2.5 \leq L/\delta \leq 10$. Using Figure 21 and working backwards, if cavities are restricted in depth to the range $0.3 \leq H/\delta \leq 0.8$, then potentially, the relationship $3 \leq L/H \leq 33$ is also a valid constraint - if the L/δ constraint is maintained.

The maximum values of the endwall centerline Bump Factor, BF_{CL}, plotted as a function of H/δ are presented in Figure 23 for all cavities. No clear correlation exists with this parameter. However, plotting BF_{CL} versus L/δ in Figure 24 is more revealing. Cavities that maintain a laminar-in/laminar-out boundary layer state typically have a BF_{CL} values clustering between 2.0 and 2.75 for $L/\delta \geq 2.5$. A close examination of the S24 (L/H=20) data when $L/\delta \geq 7$ indicate that the boundary layer state on exit is either transitional or turbulent, generating BF_{CL} values of 3.5 or larger. Cavity S23 with L/H=16 exhibits two distinct BF_{CL} variations indicated by the dashed fairing lines: open flow characteristic values of 2.3 and closed flow characteristics trending toward transitional/turbulent boundary layer heating values on exit. This behavior is consistent with this cavity being near the upper end of the transitional-cavity limit. Solid-line power-law fairings through the Model 1 (L/H=8) results (cavities S11, S12, S13 and S14) provide an apparent trend with increasing physical size. Since each line represents a matching range of M_e and Re_θ test conditions and since H/δ variations do not collapse the data, additional research is required to understand this behavior at small L/δ.

Conclusions

An experiment to evaluate the heating augmentation induced by shallow cavities under fully laminar flow conditions has been conducted in the NASA Langley 31-Inch Mach 10 Tunnel in support of the Space Shuttle Return-to-Flight Program. Two-dimensional viscous flow solutions on a flat plate model were determined using the LAURA code, providing boundary-layer edge properties that were used to design a family of rectangular-planform cavities. Three ceramic models were developed:

1) a baseline flat plate model with no cavities;
2) a model with four spanwise L/H=8 cavities with depths H/δ of 0.1, 0.2, 0.35, and 0.5; and
3) a model with four spanwise H/δ=0.35 cavities of lengths L/H of 8, 12, 16, and 20.

Phosphor thermography was used to map the heating distribution over the model surface. The heating data for each cavity and its surrounding field were converted to augmentation or Bump Factor format by referencing the measurements to a site upstream of each cavity. Test results are presented in graphical and tabular formats in this report, and they have been electronically transmitted to the Damage Assessment Aeroheating Team at Johnson Space Center. Preliminary results indicate that the floor-averaged Bump Factor is 0.291 with a standard deviation of 0.041 for fully-laminar flow conditions when $2.5 \leq L/\delta \leq 10$ for cavities in the depth range $0.3 \leq H/\delta \leq 0.8$. Over this same range of flow conditions and parameters, preliminary results also indicate that the maximum centerline cavity Bump Factor falls between 2.0 and 2.75. Cavities with $L/\delta \leq 2.5$ can not be easily classified with this approach and, accordingly, require further analysis.

Acknowledgement

References

[1] Everhart, Joel L., Alter, Stephen J., Merski, N. Ronald, Wood, William A., and Prabhu, Ramadas K.: "Pressure Gradient Effects on Hypersonic Cavity Flow Heating," AIAA 2006-0185, Presented at 44th AIAA Aerospace Sciences Meeting and Exhibit, Reno, NV, January 9-12, 2006.

[2] Everhart, Joel L., Berger, Karen T., Bey, Kim S., Merski, N. Ronald, and Wood, William A.: "Cavity Heating Experiments Supporting Shuttle Columbia Accident Investigation," NASA TM 2006-214528.

[3] Everhart, Joel L., Berger, Karen T., Brauckmann, Gregory J, Merski, N. Ronald, and Wood, William A.: "Parametric Cavity Heating Experiments Supporting Shuttle Orbiter Return To Flight," NASA TP (to be published).

[4] Micol, J.R.: "Hypersonic Aerodynamic/Aerothermodynamic Testing Capabilities at Langley Research Center: Aerothermodynamic Facilities Complex," AIAA Paper 95-2107, June 1995.

[5] Anderson, Brian, Hyatt, Jay, Wang, K.C., Everhart, Joel, Greene, Frank, Pulsonetti, Maria, Wood, Bill, Bourland, Gary, and Cassady, Amy, " The Cavity Heating Tool," Boeing Technical Memorandum ATA-AH-TM-2005-079, The Boeing Company, NASA Space Systems, Houston, TX, Dec. 7, 2005.

[6] Fletcher, L.S., Briggs, D.G., and Page, R.H., "A Review of Heat Transfer in Separated and Reattached Flows," AIAA 70-767, July 1970.

[7] Nestler, D.E., "The Effects of Surface Discontinuities on Convective Heat Transfer in Hypersonic Flow," AIAA Paper 85-0971, AIAA 20th Thermophysics Conference, Williamsburg, VA, June 1985.

[8] Burggraf, O.R., "A Model of Steady Separated Flow in Rectangular Cavities at High Reynolds Number," Proceedings of the 1965 Heat Transfer and Fluid Mechanics Conference, Stanford University Press, 1965, pp. 190-229.

[9] Chapman, D., "A Theoretical Analysis of Heat Transfer in Separated Flow," NACA TN-3792, October 1956.

[10] Carlson, W.O., "A Solution to Heat Transfer in Laminar Separated and Wake Flow Regions," General Electric R59 SD-356, March 1959.

[11] Chang, P.K., "The Reattachment of Laminar Cavity Flow with Heat Transfer at Hypersonic Speed," AFOSR-66-0135, 1966.

[12] Lamb, J.P., "An Approximate Theory for Developing Turbulent Free Shear Layers," Trans. ASME, Series D. Vol. 89, No. 3, 1967, pp. 633-642.

[13] Adams, J.C., Jr., "Numerical Calculation of Hypersonic Laminar Cavity Flows," AIAA Paper 74-707, ASME 74-HT-27, AIAA/ASME 1974 Thermophysics and Heat Transfer Conference, Boston, Mass., July 1974.

[14] Morgenstern, A. and Chokani, N., "Hypersonic Flow Past Open Cavities," AIAA Journal, Vol. 32, pp. 2387-2393, 1994.

[15] Zhang, J., Morishita, E., Okunuki, T., and Itoh H., "Experimental and Computational Investigation of Supersonic Cavity Flows," AIAA Paper 2001-1755, Presented at AIAA/NAL-NASDA-ISAS 10th International Space Planes and Hypersonic Systems and Technologies Co.

[16] Wood, William A., Pulsonetti, Maria V., Everhart, Joel L., and Bey, Kim S., "Assessment of Laura for Laminar Supersonic Shallow Cavities," Presented at 34th AIAA Fluid Dynamics Conference, Portland OR, June 28-July 1, 2004.

[17] Pulsonetti, M.V. and Wood, W.A., "Computational Aerothermodynamic of Space Shuttle Orbiter Tile Damage – Open Cavities", AIAA 2005-4679, 38th AIAA Thermo-physics Conference, Toronto, Canada, June 6-9, 2005.

[18] Galenter, S.A., "An Experimental Summary of Plasma Arc Exposures of Space Shuttle High-Temperature Reusable Surface Insulation Tile Array with a Single Missing Tile (Conducted at the Ames Research Center)," NASA SP-379, Paper 18, 1975.

[19] Nestler, D.E., "Laminar Heat Transfer to Cavities in Hypersonic Low Density Flow," Proceedings 3rd International Heat Transfer Conference, Chicago, IL, Vol. 2, 1966.

[20] Nestler, D.E., "Hypersonic Laminar Cavity Heat Transfer," Presented at 4th International Heat Transfer Conference, August 31-September 5, 1970, Versailles, France.

[21] Nicoll, K.M., "An Experimental Investigation of Laminar Hypersonic Cavity Flows Part II, Heat Transfer and Recovery Factors Measurements," ARL 63-73.

[22] Nicoll, K.M., "A Study of Laminar Hypersonic Cavity Flows," AIAA Journal, Vol. 2, No. 9, September 1964.

[23] Wyborny, W., Kabelitz, H.P. and Schepers, H.J., "Hypersonic Investigation on the Local and Average Heat Transfer in Cavities and after Steps of Bodies of Revolution," AGARD Conference Proceedings No. 19, Fluid Physics of Hypersonic Wakes, 1967.

[24] Cheatwood, F. McNeil, Merski, N. Ronald, Jr., Riely, Christopher J., and Mitcheltree, Robert A., "Aerothermodynamic Environment Definition for the Genesis Sample Return Capsule," AIAA 2001-2889, Presented at 35th AIAA Thermophysics

Conference, Anaheim, CA, June 11-14, 2001.

[25] Hahn, Mansop, "Experimental Investigation of Separated Flows over a Cavity at Hypersonic Speed," AIAA No. 68-672, AIAA Journal, Vol. 7, No. 6, June 1969, pp. 1092-1098.

[26] Nestler, D.E., "An Experimental Study of Cavity Flow on Sharp and Blunt Cones at Mach 8," AIAA 81-0335, AIAA 19th Aerospace Sciences Meeting, St. Louis, Missouri, January 12-15, 1981.

[27] Charbonnier, J.-M., and Boerrigter, H.L., "Contribution to the study of gap induced boundary layer transition in hypersonic flow," AIAA Paper 93-5111, presented at AIAA and DGLR, 5th International Aerospace Planes and Hypersonic Technologies Conference, Munich, Germany, November 30-December 3, 1993.

[28] Boerrigter, Herman and Charbonnier, Jean-Marc, "Roughness-induced transition in hypersonic flow," Space Scientific Research in Belgium, Volume 4; 51-52; D/1996/1191/5-Vol-4/ (SEE 19970005230)

[29] Hollis, Brian R. and Liechty, Derek S., "Boundary Layer Transition Correlations and Aeroheating Predictions for Mars Smart Lander," AIAA 2002-2745, Presented at 32nd AIAA Fluid Dynamics Conference and Exhibit, St. Louis, Missouri, 24-26 June 2002.

[30] Hollis, Brian R. and Liechty, Derek S., "Correlations for Boundary Layer Transition on Mars Science Laboratory Entry Vehicle due to Heat-Shield Cavities," NASA TP-2008-215317, 2008.

[31] Hollis, Brian R. and Liechty, Derek S., "Mars Science Laboratory Experimental Aerotherodynamics with Effects of Cavities and Control Surfaces" JSR Vol. 43, No. 2 Mar-Apr 2006, pp340-353.

[32] Larson, H.K. and Keating, Jr., S.L., "Transition Reynolds Numbers of Separated Flows at Supersonic Speeds," NASA TN D-349, December 1960.

[33] Liechty, Derek S., Horvath, Thomas J., and Berry, Scott A., "Shuttle Return to Flight Experimental Results, Cavity Effects on Boundary Layer Transition," NASA TM-2006-214305, 2006.

[34] Rhudy, J.P. and Magnan, Jr., J.D., "Investigation of Heat-Transfer Distribution in Several Cavity and Step Configurations at Mach 10," AEDC Technical Documentary Report No. AEDC-TDR-64-220, October 1964.

[35] Charwat, A.F., Roos, J.N., Dewey, C.F., Jr., and Hitz, J.A., "An Investigation of Separated Flows – Part I, The Pressure Field," Journal of Aerospace Sciences, Vol. 28, No. 6, June 1961, pp. 457-470.

[36] Charwat, A.F., Dewey, C.F., Roos, J.N., and Hitz, J.A., "An Investigation of Separated Flows – Part II, Flow in the Cavity and Heat Transfer," Journal of Aerospace Sciences, Vol. 28, No. 7, pp. 513-527, July 1961.

[37] Chin, E., Rafiinejad and Seban, R.A., "Prediction of the Flow and Heat Transfer in a Rectangular Wall Cavity with Turbulent Flow," Transactions of the ASME, Journal of Applied Mechanics, Vol. 39, Series E, No. 2, pp. 351-358, June 1972.

[38] Emery, A.F., "Recompression Step Heat Transfer Coefficients for Supersonic Open Cavity Flow," Journal of Heat Transfer, 1969, pp. 168-170.

[39] Hunt, L.R., "Aerodynamic Heating in Large Cavities in an Array of RSI Tiles," NASA TN D-8400, 1977.

[40] Lamb, J.P. and Bass, R.L., "Some Correlations of Theory and Experiment for Developing Turbulent Free Shear Layers," Trans. ASME, Series D, Vol. 90, No. 4, pp. 572-580, 1968.

[41] Lamb, J.P., "Convective Heat Transfer Correlations for Planar, Supersonic, Separated Flows", Trans. ASME, Series C, Vol.

102, No. 2, May 1980, pp. 351-356.

[42] Lamb, J.P., "Analysis and Correlation of Convective Heat Transfer Measurements for Open Cavities in Supersonic Flow," AIAA 80-1526, July 1980.

[43] Nestler, D.E., Saydah, A.R., and Auxer, W.L., "Heat Transfer to Steps and Cavities in Hypersonic Turbulent Flow," AIAA Paper No. 68-673, 1968.

[44] Nestler, D.E., Saydah, A.R., and Auxer, W.L., "Heat Transfer to Steps and Cavities in Hypersonic Turbulent Flow," AIAA Journal, Vol. 7, No. 7, July 1969, pp. 1368-1370.

[45] Nestler, D.E., "Hypersonic Boundary Layers and Selected Heat Flux Problems," Short Course on Technology of Space Shuttle Vehicles and Space Stations at the University of Tennessee Space Institute, April 1970.

[46] Shchukin, V.K., Gortyshov, Yu. F., Varfolomeev, I.M., and Nadyrov, N.A., "Influence of Relative Depth and Reynolds Number on Heat Transfer in Cavities in Compressible Gas Flow," Soviet Aeronaut., Vol. 23, No. 3, 1980, pp. 83-86.

[47] Stallings, Robert L., Jr. and Wilcox, Floyd J., Jr., "Experimental Cavity Pressure Distributions at Supersonic Speeds", NASA TP 2683, June 1987.

[48] Hunt, L.R., "Aerodynamic Heating and Loading within Large Open Cavities in Cone and Cone-Cylinder-Flare Models at Mach 6.7," NASA TN D-7403, March 1974.

[49] Netterfield, M.P. and Hilier, R., "Experiment and computation in hypersonic cavity flows," AIAA Paper 89-1842, Presented at 20th AIAA Fluid Dynamics, Plasma Dynamics and Lasers Conference, Buffalo, NY, June 12-14, 1989.

[50] Wilcox, Floyd J., Jr., "Experimental Investigation of Porous-Floor Effects on Cavity Flow Fields at Supersonic Speeds," NASA TP 3032, November 1990.

[51] Wilcox, Floyd J., Jr., "Tangential, Semi-submerged, and Internal Store Carriage and Separation at Supersonic Speeds," AIAA Paper 91-0198, Presented at 29th Aero-space Sciences Meeting, Reno NV., January 1991.

[52] Blair, A.B., Jr. and Stallings, R.L., Jr., "Supersonic Axial-Force Characteristics of a Rectangular-Box Cavity with Various Length-to-Depth Ratios in a Flat Plate," NASA TM-87659, 1986.

[53] Stallings, Robert L., Jr., Wilcox, Floyd J., Jr., and Forrest, Dana K., "Measurements of Forces, Moments, and Pressures on a Generic Store Separating From a Box Cavity at Supersonic Speeds," NASA TP 3110, Sept. 1991.

[54] Coats, Jack D., Rhudy, R.W., and Edmunds, E.W., "Effects of Surface Gaps and Steps on Laminar Heat-Transfer Rates at Local Mach Numbers from 3 to 10," AEDC-TR-70-17, February 1970.

[55] Johnson, C.B., "Heat Transfer Data to Cavities between Simulated RSI Tiles at Mach 8," NASA CR 128770, June 1973.

[56] Throckmorton, D.A.: "Heat Transfer to Surface and Saps of RSI Tile Arrays in Turbulent Flow at Mach 10.3," NASA-TM-X-71945, April 1974.

[57] Weinstein, Irving, Avery, Don E., and, Chapman Andrew J., "Aerodynamic Heating to the Gaps and Surfaces of Simulated Reusable-Surface-Insulation Tile Arrays in Turbulent Flow at Mach 6.6," NASA TM X-3225, November 1975.

[58] Berry, Scott. A., Horvath, Thomas J., Greene, Francis A., Kinder, Gerald R., and Wang, K. C., "Overview of Boundary Layer Transition Research in Support of Orbiter Return To Flight." AIAA Paper 2006-2918, June 2006.

[59] Liechty, Derek S., Berry, Scott A., and Horvath, Thomas J.: "Shuttle Return to Flight Experimental Results: Protuberance Effects on Boundary Layer Transition," NASA TM-2006-214306, June 2006.

[60] Campbell, Charles H., Wang, K. C., An, Michael Y., Tam, Luen T., Bouslog, Stanley A., "Orbiter Boundary-Layer Working Group, Numerical Flow Field Analysis Data," JSC-26816, December, 1994.

[61] Reuther, J., McDaniel, R., Brown, J.,Prabhu, D., and Saunders, D.: "External Computational Aerothermodynamic Analysis of the Space Shuttle Orbiter at STS-107 Flight Conditions," 37th AIAA Thermophysics Conference, Portland, OR, June 28-1, 2004.

[62] Wright, M.J., Candler, G., and Bose, D.: "Data-Parallel Line Relaxation Method for the Navier-Stokes Equations," AIAA Journal, Vol. 36, No. 9, 1998, pp. 1603-1609.

[63] Dye, Thomas P., Everhart, Joel L., Hodge, J.A.: "Blockage Induce by Large Test Technique Demonstrator Models with Propulsion Simulation in the NASA Langley 31-Inch Mach 10 Tunnel," NASP Technical Memorandum 1163, 1992.

[64] Gnoffo, P.A., Gupta, R.N., and Shinn, J.L., "Conservation Equations and Physical Models for Hypersonic Air Flows in Thermal and Chemical Nonequilibrium," NASA TP 2867, February 1989.

[65] Gnoffo, P.A., "An Upwind-Biased, Point-Implicit Relaxation Algorithm for Viscous, Compressible Perfect Gas Flows," NASA TP 2953, February 1990.

[66] Palmer, Grant; Alter, Steve; Everhart, Joel; Wood, William; Driver, Dave; Brown, Jim; and, Prabhu, Ramadas: "CFD Validation for Long and Short Cavity Flow Simulations." Presented at 39th AIAA Thermophysics Conference, Miami, FL, June 25-28, 2007, AIAA-2007-4254.

[67] External Aerothermal Analysis Team Report to the Orbiter Configuration Control Board, "Smooth Outer Mold Line Aerothermal Solution Database for Orbiter Windside Acreage Environments During Nominal Entry Conditions," NASA Johnson Space Center Engineering Note, EG-SS-06-1, 2005.

[68] Merski, N.R.: "An Improved Two-Color Relative-Intensity Phosphor Thermography Method for Hypersonic Wind Tunnel Aeroheating Measurements," NASA CDTP-1017, February 2001.

[69] Buck, G.M., and Vasques, P., "An Investment Ceramic Slip-Casting Technique for Net-Form, Precision, Detailed Casting of Ceramic Models," U.S. Patent 5,266,252, November 1993.

[70] Buck, G.M., Powers, M.A., Nevins, S.C., Griffith, M.S., Verneris, P.H., and Wainwright, G.A., "Rapid Fabrication of Flat Plate Cavity Phosphor Thermography Test Models for Shuttle Return-to-Flight Aero-Heating," NASA TM 2006-214508.

[71] Merski, N.R., "Global Aeroheating Wind Tunnel Measurements Using Improved Two-Color Phosphor Thermography Method," Journal of Spacecraft and Rockets, Vol. 36, No. 2, 1999, pp. 160-170.

[72] Fay, J.A. and Riddell, F.R., "Theory of Stagnation Point Heat Transfer in Dissociated Air," Journal of Aeronautical Sciences, Vol. 25, No. 2, 1958, pp. 73-85.

[73] Coleman, Hugh W. and Steele, W. Glenn: "Experimentation and Uncertainty Analysis for Engineers," John Wiley & Sons, New York, 1989.

Tables

Table 1.-Typical range of windward surface flow conditions at Mach 18.

M_e	2.2 - 3.2
Re_θ	120 - 700
δ	1 - 6 inches

Table 2.- Nominal flow conditions for the 31-Inch Mach 10 Air Tunnel.

P_{T1} psi	T_{T1} ºR	$P_\infty \times 10^2$ psi	T_∞ ºR	q_∞ psi	V_∞ ft/s	M_∞	$R_\infty \times 10^{-6}$ ft^{-1}	P_{T1} psi	Test Core in.
348	1800	0.992	95.2	0.650	4628	9.67	0.568	1.205	10x10
723	1825	1.867	94.2	1.259	4670	9.81	1.104	2.334	12x12
1452	1800	3.509	90.7	2.430	4643	9.94	2.240	4.503	12x12

Table 3.- As-built cavity geometries.

	Cavity	y (inch)	H (inch)	W (inch)	L (inch)	W/H	L/H
Model M1	**S11**	3	0.018	0.060	0.118	3.33	6.6
	S12	1	0.036	0.165	0.333	4.58	9.3
	S13	-1	0.063	0.270	0.550	4.29	8.7
	S14	-3	0.099	0.391	0.800	3.95	8.1
Model M2	**S21**	-3	0.068	0.272	0.530	4.00	7.8
	S22	-1	0.074	0.277	0.793	3.74	10.7
	S23	1	0.071	0.278	1.065	3.92	15.0
	S24	3	0.067	0.282	1.360	4.21	20.3

Note: Cavities S13 and S21 were designed as a common reference cavity between Models M1 and M2.

Table 4.-Baseline model run matrix from Test 406.

Run	Zoom	Model View	Config	P_{T1} (psia)	T_{T1} (ºF)	Re (x10^{-6}) (ft^{-1})	α (deg)	Comments
68	35	Global	Base	602.66	1314.80	0.94	-7.77	
69	35	Global	Base	823.28	1323.09	1.23	-7.20	
70	35	Global	Base	1096.83	1333.19	1.59	-6.53	
71	35	Global	Base	1377.99	1337.74	1.96	-6.29	
74	35	Global	Base	1152.81	1319.22	1.69	-11.42	
73	35	Global	Base	782.86	1319.56	1.18	-17.89	
72	35	Global	Base	1215.85	1338.86	1.74	-15.57	
75	35	Global	Base	1379.18	1330.20	1.97	-6.29	Random Repeat

Table 5.- Test 404 run matrix for cavity-plate model 1.

Run	Zoom	Model View	Config	P_{T1} (psia)	T_{T1} (°F)	Re $(\times 10^{-6})$ (ft^{-1})	α (deg)	Comments
1	18	Global	M1	641.28	1324.51	0.985	-7.77	Re high. Lower Pr
2	18	Global	M1	593.04	1329.40	0.914	-7.77	
3	70	Top	S11	592.44	1324.56	0.916	-7.77	
	70	Top	S12	592.44	1324.56	0.916	-7.77	
4	70	Bottom	S13	593.04	1332.72	0.911	-7.77	
	70	Bottom	S14	593.04	1332.72	0.911	-7.77	
7	18	Global	M1	802.11	1336.51	1.193	-7.20	
6	70	Top	S11	802.40	1328.00	1.203	-7.20	
	70	Top	S12	802.40	1328.00	1.203	-7.20	
5	70	Bottom	S13	801.64	1328.44	1.202	-7.20	
	70	Bottom	S14	801.64	1328.44	1.202	-7.20	
8	18	Global	M1	522.97	1343.67	0.806	-14.18	
9	70	Top	S11	523.16	1346.34	0.804	-14.18	
	70	Top	S12	523.16	1346.34	0.804	-14.18	
10	70	Bottom	S13	523.35	1344.15	0.806	-14.18	
	70	Bottom	S14	523.35	1344.15	0.806	-14.18	
13	18	Global	M1	834.57	1331.40	1.243	-12.39	
12	70	Top	S11	834.66	1329.63	1.245	-12.39	
	70	Top	S12	834.66	1329.63	1.245	-12.39	
11	70	Bottom	S13	834.66	1329.32	1.247	-12.39	
	70	Bottom	S14	834.66	1329.32	1.247	-12.39	
14	18	Global	M1	1194.51	1335.36	1.725	-15.57	Re low. Raise Pr
15	18	Global	M1	1218.78	1328.26	1.768	-15.57	Re slightly high - use
17	70	Top	S11	1214.31	1345.15	1.736	-15.57	
	70	Top	S12	1214.31	1345.15	1.736	-15.57	
16	70	Bottom	S13	1216.02	1343.06	1.740	-15.57	
	70	Bottom	S14	1216.02	1343.06	1.740	-15.57	
24	70	Top	S11	1082.78	1328.56	1.585	-6.53	
	70	Top	S12	1082.78	1328.56	1.585	-6.53	
23	70	Bottom	S13	1083.54	1332.89	1.579	-6.53	
	70	Bottom	S14	1083.54	1332.89	1.579	-6.53	
25	144	Top	S11	1082.02	1332.61	1.578	-6.53	Examining zoom and pixelation
	144	Top	S12	1082.02	1332.61	1.578	-6.53	Examine zoom and pixelation
20	70	Top	S11	1126.56	1333.84	1.636	-11.42	
	70	Top	S12	1126.56	1333.84	1.636	-11.42	
21	70	Bottom	S13	1125.42	1335.16	1.631	-11.42	
	70	Bottom	S14	1125.42	1335.16	1.631	-11.42	
18	70	Top	S11	773.85	687.63	2.269	-17.89	T_{T1} too low during run
	70	Top	S12	773.85	687.63	2.269	-17.89	T_{T1} too low during run
19	70	Top	S11	782.41	1329.20	1.174	-17.89	
	70	Top	S12	782.41	1329.20	1.174	-17.89	
22	70	Bottom	S13	781.84	1331.32	1.172	-17.89	
	70	Bottom	S14	781.84	1331.32	1.172	-17.89	

Table 6.- Test 404 run matrix for cavity-plate model 2.

Run	Zoom	Model View	Config	P_{T1} (psia)	T_{T1} (°F)	Re $(\times 10^{-6})$ (ft^{-1})	α (deg)	Comments
26	18	Global	M2	-	-	-	-7.77	No tunnel conditions.
27	18	Global	M2	591.21	1324.55	0.92	-7.77	Repeat of run 26
29	70	Bottom	S21	591.78	1323.87	0.92	-7.77	
	70	Bottom	S22	591.78	1323.87	0.92	-7.77	
28	70	Top	S23	592.45	1324.41	0.92	-7.77	
	70	Top	S24	592.45	1324.41	0.92	-7.77	
30	70	Bottom	S21	-	-	-	-7.20	Heater problem
	70	Bottom	S22	-	-	-	-7.20	Heater problem
31	70	Bottom	S21	802.21	1319.50	1.21	-7.20	Repeat of run 30
	70	Bottom	S22	802.21	1319.50	1.21	-7.20	
32	70	Top	S23	801.26	1322.53	1.21	-7.20	
	70	Top	S24	801.26	1322.53	1.21	-7.20	
36	70	Bottom	S21	522.21	1346.69	0.80	-14.18	
	70	Bottom	S22	522.21	1346.69	0.80	-14.18	
37	70	Top	S23	523.16	1349.63	0.80	-14.18	
	70	Top	S24	523.16	1349.63	0.80	-14.18	
33	18	Global	M2	835.33	1326.14	1.25	-12.39	
35	70	Bottom	S21	834.57	1324.02	1.25	-12.39	
	70	Bottom	S22	834.57	1324.02	1.25	-12.39	
34	70	Top	S23	837.71	1328.62	1.25	-12.39	
	70	Top	S24	837.71	1328.62	1.25	-12.39	
38	18	Global	M2	1214.41	1345.21	1.73	-15.57	
40	70	Bottom	S21	1217.74	1337.28	1.75	-15.57	
	70	Bottom	S22	1217.74	1337.28	1.75	-15.57	
39	70	Top	S23	1215.36	1332.45	1.76	-15.57	
	70	Top	S24	1215.36	1332.45	1.76	-15.57	
47	70	Bottom	S21	780.89	1332.37	1.17	-17.89	
	70	Bottom	S22	780.89	1332.37	1.17	-17.89	
48	70	Top	S23	780.32	1325.80	1.77	-17.89	
	70	Top	S24	780.32	1325.80	1.77	-17.89	
46	70	Bottom	S21	1125.61	1331.86	1.64	-11.42	
	70	Bottom	S22	1125.61	1331.86	1.64	-11.42	
45	70	Top	S23	1125.70	1333.29	1.64	-11.42	
	70	Top	S24	1125.70	1333.29	1.64	-11.42	
42	70	Bottom	S21	1082.78	1328.89	1.58	-6.53	
	70	Bottom	S22	1082.78	1328.89	1.58	-6.53	
41	70	Top	S23	1083.26	1335.78	1.58	-6.53	
	70	Top	S24	1083.26	1335.78	1.58	-6.53	
43	70	Bottom	S21	1356.21	1327.07	1.95	-6.29	
	70	Bottom	S22	1356.21	1327.07	1.95	-6.29	
44	70	Top	S23	1355.45	1328.13	1.95	-6.29	Camera misaligned-Cavities 22 and 23.
	70	Top	S24	1355.45	1328.13	1.95	-6.29	Camera misaligned-Cavities 22 and 23.
49	70	Top	S23	1356.31	1338.32	1.93	-6.29	
	70	Top	S24	1356.31	1338.32	1.93	-6.29	

Table 7.- Cavity flow conditions and parameters, x_{cav}=8 inches.

Run	Cavity	y, cavity (inch)	M_e	Re_θ	Re_θ/M_e	δ (inch)	θ (inch)	H/δ	W/δ	L/δ
GLOBAL										
1	M1	Global	2.78	170	61	0.1882	0.0226			
2	M1	Global	2.78	165	59	0.1942	0.0233			
7	M1	Global	2.81	182	65	0.1768	0.0211			
8	M1	Global	2.37	191	80	0.1505	0.0200			
13	M1	Global	2.43	210	86	0.1343	0.0176			
14	M1	Global	2.19	260	118	0.1004	0.0140			
15	M1	Global	2.19	262	119	0.0997	0.0139			
27	M2	Global	2.78	260	94	0.1945	0.0234			
38	M2	Global	2.19	261	119	0.0999	0.0139			
CAVITY S11										
3	S11	3	2.78	165	59	0.1943	0.0233	0.09	0.31	0.61
6	S11	3	2.81	182	65	0.1768	0.0211	0.10	0.34	0.67
9	S11	3	2.37	191	80	0.1505	0.0200	0.12	0.40	0.78
12	S11	3	2.43	210	86	0.1343	0.0176	0.13	0.45	0.88
17	S11	3	2.19	261	119	0.0999	0.0139	0.18	0.60	1.18
18	S11	3	2.12	241	114	0.1118	0.0159	0.16	0.54	1.06
19	S11	3	2.12	242	114	0.1113	0.0159	0.16	0.54	1.06
20	S11	3	2.48	228	92	0.1247	0.0161	0.14	0.48	0.95
24	S11	3	2.85	200	70	0.1623	0.0192	0.11	0.37	0.73
25	S11	3	2.85	200	70	0.1624	0.0192	0.11	0.37	0.73
CAVITY S12										
3	S12	1	2.78	165	59	0.1943	0.0233	0.19	0.85	1.71
6	S12	1	2.81	182	65	0.1768	0.0211	0.20	0.93	1.88
9	S12	1	2.37	191	80	0.1505	0.0200	0.24	1.10	2.21
12	S12	1	2.43	210	86	0.1343	0.0176	0.27	1.23	2.48
17	S12	1	2.19	261	119	0.0999	0.0139	0.36	1.65	3.33
18	S12	1	2.12	241	114	0.1118	0.0159	0.32	1.48	2.98
19	S12	1	2.12	242	114	0.1113	0.0159	0.32	1.48	2.99
20	S12	1	2.48	228	92	0.1247	0.0161	0.29	1.32	2.67
24	S12	1	2.85	200	70	0.1623	0.0192	0.22	1.02	2.05
25	S12	1	2.85	200	70	0.1624	0.0192	0.22	1.02	2.05
CAVITY S13										
4	S13	-1	2.78	165	59	0.1942	0.0233	0.32	1.39	2.83
5	S13	-1	2.81	182	65	0.1768	0.0211	0.36	1.53	3.11
10	S13	-1	2.37	191	80	0.1505	0.0200	0.42	1.79	3.65
11	S13	-1	2.43	210	86	0.1343	0.0176	0.47	2.01	4.10
16	S13	-1	2.19	261	119	0.0998	0.0139	0.63	2.70	5.51
21	S13	-1	2.48	228	92	0.1248	0.0161	0.50	2.16	4.41
22	S13	-1	2.12	242	114	0.1113	0.0159	0.57	2.43	4.94
23	S13	-1	2.85	200	70	0.1623	0.0192	0.39	1.66	3.39

Table 7.- Continued.

Run	Cavity	y, cavity (inch)	M_e	Re_θ	Re_θ/M_e	δ (inch)	θ (inch)	H/δ	W/δ	L/δ
CAVITY S14										
4	S14	-3	2.78	165	59	0.1942	0.0233	0.51	2.01	4.12
5	S14	-3	2.81	182	65	0.1768	0.0211	0.56	2.21	4.52
10	S14	-3	2.37	191	80	0.1505	0.0200	0.66	2.60	5.32
11	S14	-3	2.43	210	86	0.1343	0.0176	0.74	2.91	5.96
16	S14	-3	2.19	261	119	0.0998	0.0139	0.99	3.92	8.01
21	S14	-3	2.48	228	92	0.1248	0.0161	0.79	3.13	6.41
22	S14	-3	2.12	242	114	0.1113	0.0159	0.89	3.51	7.19
23	S14	-3	2.85	200	70	0.1623	0.0192	0.61	2.41	4.93
CAVITY S21										
29	S21	-3	2.78	165	59	0.1944	0.0234	0.35	1.40	2.73
30	S21	-3	2.81	182	65	0.1768	0.0211	0.38	1.54	3.00
31	S21	-3	2.81	182	65	0.1769	0.0211	0.38	1.54	3.00
35	S21	-3	2.43	210	86	0.1343	0.0176	0.51	2.03	3.95
36	S21	-3	2.37	191	80	0.1506	0.0200	0.45	1.81	3.52
40	S21	-3	2.19	262	119	0.0998	0.0139	0.68	2.73	5.31
42	S21	-3	2.85	200	70	0.1623	0.0192	0.42	1.68	3.26
43	S21	-3	2.86	218	76	0.1502	0.0177	0.45	1.81	3.53
46	S21	-3	2.48	228	92	0.1248	0.0161	0.55	2.18	4.25
47	S21	-3	2.12	242	114	0.1114	0.0159	0.61	2.44	4.76
CAVITY S22										
29	S22	-1	2.78	165	59	0.1944	0.0234	0.38	1.42	4.08
30	S22	-1	2.81	182	65	0.1768	0.0211	0.42	1.57	4.49
31	S22	-1	2.81	182	65	0.1769	0.0211	0.42	1.57	4.48
35	S22	-1	2.43	210	86	0.1343	0.0176	0.55	2.06	5.91
36	S22	-1	2.37	191	80	0.1506	0.0200	0.49	1.84	5.26
40	S22	-1	2.19	262	119	0.0998	0.0139	0.74	2.78	7.95
42	S22	-1	2.85	200	70	0.1623	0.0192	0.46	1.71	4.89
43	S22	-1	2.86	218	76	0.1502	0.0177	0.49	1.84	5.28
46	S22	-1	2.48	228	92	0.1248	0.0161	0.59	2.22	6.36
47	S22	-1	2.12	242	114	0.1114	0.0159	0.66	2.49	7.12
CAVITY S23										
28	S23	1	2.78	165	59	0.1943	0.0233	0.37	1.43	5.48
32	S23	1	2.43	210	86	0.1342	0.0176	0.53	2.07	7.93
34	S23	1	2.43	210	87	0.1341	0.0175	0.53	2.07	7.94
37	S23	1	2.37	191	80	0.1505	0.0200	0.47	1.85	7.08
39	S23	1	2.19	261	119	0.0998	0.0139	0.71	2.78	10.67
41	S23	1	2.85	200	70	0.1623	0.0192	0.44	1.71	6.56
44	S23	1	2.86	218	76	0.1502	0.0177	0.47	1.85	7.09
45	S23	1	2.48	228	92	0.1247	0.0161	0.57	2.23	8.54
48	S23	1	2.12	242	114	0.1114	0.0159	0.64	2.49	9.56
49	S23	1	2.15	218	101	0.0943	0.0123	0.75	2.95	11.30

Table 7.- Concluded.

Run	Cavity	y, cavity (inch)	M_e	Re_θ	Re_θ/M_e	δ (inch)	θ (inch)	H/δ	W/δ	L/δ
CAVITY S24										
28	S24	3	2.78	165	59	0.1943	0.0233	0.34	1.45	7.00
32	S24	3	2.43	210	86	0.1342	0.0176	0.50	2.10	10.13
34	S24	3	2.43	210	87	0.1341	0.0175	0.50	2.10	10.14
37	S24	3	2.37	191	80	0.1505	0.0200	0.45	1.87	9.03
39	S24	3	2.19	261	119	0.0998	0.0139	0.67	2.82	13.62
41	S24	3	2.85	200	70	0.1623	0.0192	0.41	1.74	8.38
44	S24	3	2.86	218	76	0.1502	0.0177	0.45	1.88	9.05
45	S24	3	2.48	228	92	0.1247	0.0161	0.54	2.26	10.90
48	S24	3	2.12	242	114	0.1114	0.0159	0.60	2.53	12.20
49	S24	3	2.15	218	101	0.0943	0.0123	0.71	2.99	14.43

Table 8.- Variable uncertainty values.

Uncertainty Type	Bias Uncertainty	Precision Uncertainty
Initial model wall temperature	1.43 °C	1.0 °C
Model run wall temperature at reference location	1.93 °C	n/a
Model run wall temperature	3.36 °C	1.0 °C
Effective time	0.02 s	0.05 s
Thermal product, β	5.9%	n/a

Table 9.- Summary Cavity Data.

Run	Cavity	δ (inch)	L (inch)	H (inch)	L/δ	H/δ	L/H	Avg Floor BF	Max CL BF
3	S11	0.2504	0.1500	0.0187	0.599	0.075	8.02	0.652	3.26
3	S12	0.2504	0.2977	0.0396	1.189	0.158	7.52	0.446	3.00
4	S13	0.2504	0.5296	0.0662	2.115	0.264	8.00	0.328	3.74
4	S14	0.2504	0.7578	0.1021	3.026	0.408	7.42	0.248	2.26
5	S13	0.2245	0.5296	0.0662	2.359	0.295	8.00	0.352	2.13
5	S14	0.2245	0.7578	0.1021	3.375	0.455	7.42	0.318	2.49
6	S11	0.2245	0.1500	0.0187	0.668	0.083	8.02	0.720	1.73
6	S12	0.2245	0.2977	0.0396	1.326	0.176	7.52	0.391	4.59
9	S11	0.1903	0.1500	0.0187	0.788	0.098	8.02	0.634	1.85
9	S12	0.1903	0.2977	0.0396	1.564	0.208	7.52	0.421	1.44
10	S13	0.1903	0.5296	0.0662	2.783	0.348	8.00	0.264	2.03
10	S14	0.1903	0.7578	0.1021	3.982	0.536	7.42	0.254	2.69
11	S13	0.1663	0.5296	0.0662	3.185	0.398	8.00	0.269	2.23
11	S14	0.1663	0.7578	0.1021	4.558	0.614	7.42	0.269	2.41
12	S11	0.1663	0.1500	0.0187	0.902	0.112	8.02	0.704	1.58
12	S12	0.1663	0.2977	0.0396	1.791	0.238	7.52	0.415	2.61
16	S13	0.1220	0.5296	0.0662	4.342	0.543	8.00	0.316	2.10
16	S14	0.1220	0.7578	0.1021	6.212	0.837	7.42	0.330	2.73
17	S11	0.1220	0.1500	0.0187	1.230	0.153	8.02	0.664	1.68
17	S12	0.1220	0.2977	0.0396	2.441	0.325	7.52	0.462	1.59
19	S11	0.1463	0.1500	0.0187	1.025	0.128	8.02	0.630	1.27
19	S12	0.1463	0.2977	0.0396	2.035	0.271	7.52	0.469	1.89
20	S11	0.1501	0.1500	0.0187	1.000	0.125	8.02	0.662	1.19
20	S12	0.1501	0.2977	0.0396	1.984	0.264	7.52	0.455	1.91
21	S13	0.1501	0.5296	0.0662	3.529	0.441	8.00	0.272	1.85
21	S14	0.1501	0.7578	0.1021	5.050	0.680	7.42	0.239	2.09
22	S13	0.1463	0.5296	0.0662	3.620	0.453	8.00	0.321	2.08
22	S14	0.1463	0.7578	0.1021	5.180	0.698	7.42	0.269	2.49
23	S13	0.2009	0.5296	0.0662	2.636	0.329	8.00	0.247	2.54
23	S14	0.2009	0.7578	0.1021	3.771	0.508	7.42	0.198	2.25
24	S11	0.2009	0.1500	0.0187	0.747	0.093	8.02	0.711	2.05
24	S12	0.2009	0.2977	0.0396	1.482	0.197	7.52	0.410	2.62
25	S11	0.2009	0.1500	0.0187	0.747	0.093	8.02	0.689	2.51
25	S12	0.2009	0.2977	0.0396	1.482	0.197	7.52	0.434	3.31

Table 9.- Concluded.

Run	Cavity	δ (inch)	L (inch)	H (inch)	L/δ	H/δ	L/H	Avg Floor BF	Max CL BF
28	S23	0.2504	1.0616	0.0676	4.239	0.270	15.70	0.415	2.35
28	S24	0.2504	1.3277	0.0670	5.302	0.268	19.82	0.521	2.29
29	S21	0.2504	0.5246	0.0666	2.095	0.266	7.88	0.342	2.00
29	S22	0.2504	0.7971	0.0652	3.183	0.260	12.23	0.397	2.08
31	S21	0.2245	0.5246	0.0666	2.336	0.297	7.88	0.255	2.14
31	S22	0.2245	0.7971	0.0652	3.550	0.290	12.23	0.328	2.67
32	S23	0.2245	1.0616	0.0676	4.728	0.301	15.70	0.440	2.73
32	S24	0.2245	1.3277	0.0670	5.913	0.298	19.82	0.546	2.45
34	S23	0.1663	1.0616	0.0676	6.385	0.407	15.70	0.486	3.23
34	S24	0.1663	1.3277	0.0670	7.986	0.403	19.82	0.553	4.43
35	S21	0.1663	0.5246	0.0666	3.155	0.401	7.88	0.275	2.34
35	S22	0.1663	0.7971	0.0652	4.794	0.392	12.23	0.275	2.08
36	S21	0.1903	0.5246	0.0666	2.756	0.350	7.88	0.301	2.04
36	S22	0.1903	0.7971	0.0652	4.188	0.343	12.23	0.320	2.05
37	S23	0.1903	1.0616	0.0676	5.578	0.355	15.70	0.343	2.92
37	S24	0.1903	1.3277	0.0670	6.976	0.352	19.82	0.552	4.36
39	S23	0.1220	1.0616	0.0676	8.703	0.554	15.70	0.345	2.26
39	S24	0.1220	1.3277	0.0670	10.885	0.549	19.82	0.501	3.50
40	S21	0.1220	0.5246	0.0666	4.301	0.546	7.88	0.301	2.20
40	S22	0.1220	0.7971	0.0652	6.535	0.535	12.23	0.342	2.34
41	S23	0.2009	1.0616	0.0676	5.283	0.336	15.70	0.349	2.33
41	S24	0.2009	1.3277	0.0670	6.608	0.333	19.82	0.525	2.58
42	S21	0.2009	0.5246	0.0666	2.611	0.331	7.88	0.288	2.62
42	S22	0.2009	0.7971	0.0652	3.967	0.324	12.23	0.267	2.08
43	S21	0.1854	0.5246	0.0666	2.830	0.359	7.88	0.302	2.44
43	S22	0.1854	0.7971	0.0652	4.300	0.352	12.23	0.284	2.28
45	S23	0.1501	1.0616	0.0676	7.075	0.450	15.70	0.305	2.19
45	S24	0.1501	1.3277	0.0670	8.848	0.446	19.82	0.502	4.64
46	S21	0.1501	0.5246	0.0666	3.496	0.444	7.88	0.270	2.14
46	S22	0.1501	0.7971	0.0652	5.312	0.434	12.23	0.282	2.12
47	S21	0.1463	0.5246	0.0666	3.586	0.455	7.88	0.291	2.22
47	S22	0.1463	0.7971	0.0652	5.449	0.446	12.23	0.363	2.90
48	S23	0.1463	1.0616	0.0676	7.257	0.462	15.70	0.488	3.59
48	S24	0.1463	1.3277	0.0670	9.076	0.458	19.82	0.580	3.67
49	S23	0.1854	1.0616	0.0676	5.727	0.365	15.70	0.346	2.49
49	S24	0.1854	1.3277	0.0670	7.162	0.361	19.82	0.523	2.85

Figures
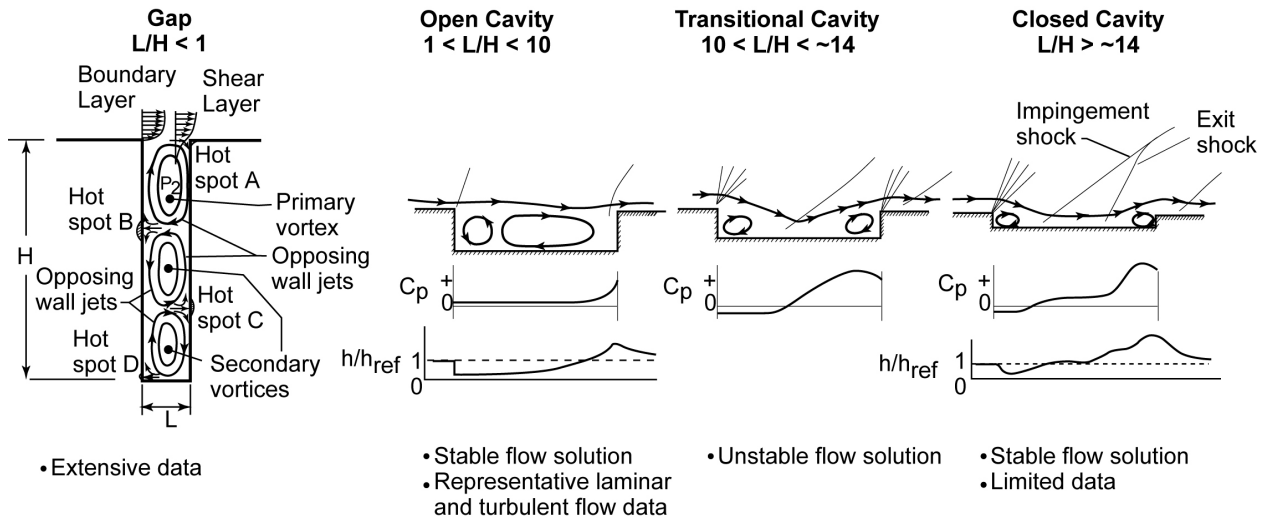
Figure 1.- Cavity flow regimes.
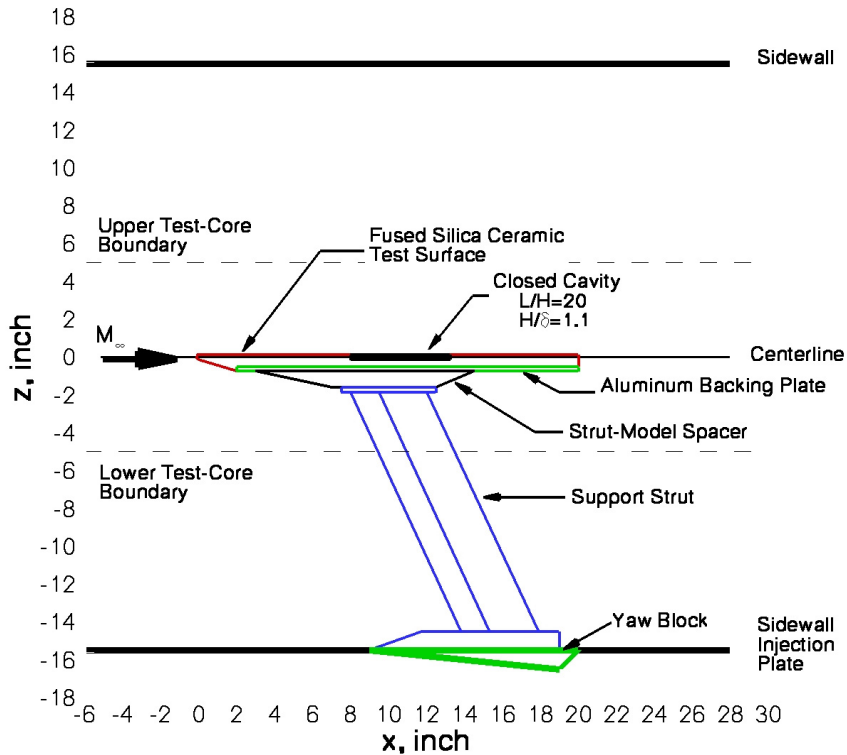
Figure 2.- Schematic of model mounting.
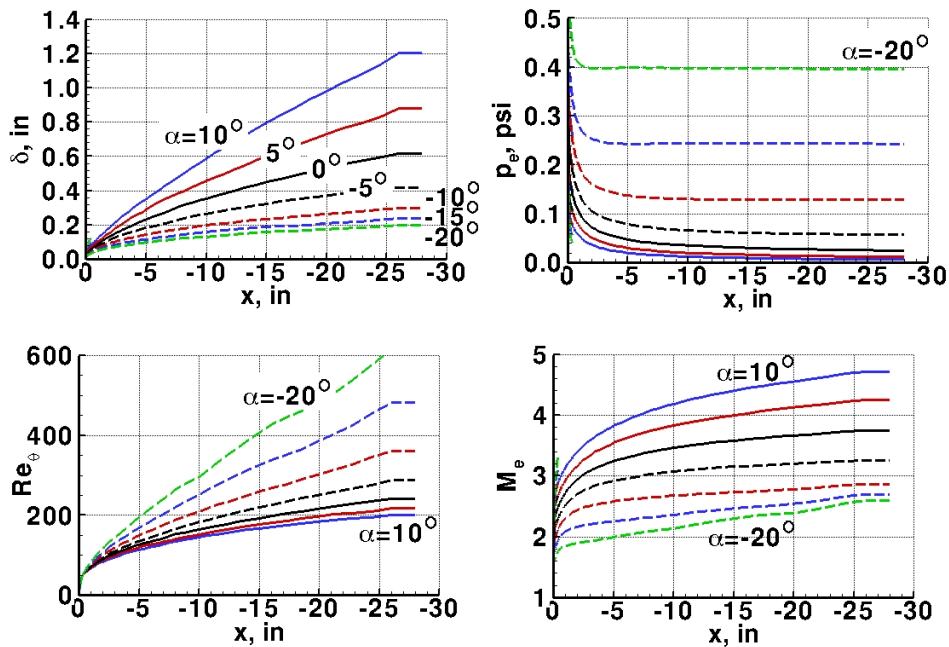
Figure 3.- Representative flat plate surface flow properties. Re=1x10^6 per foot.
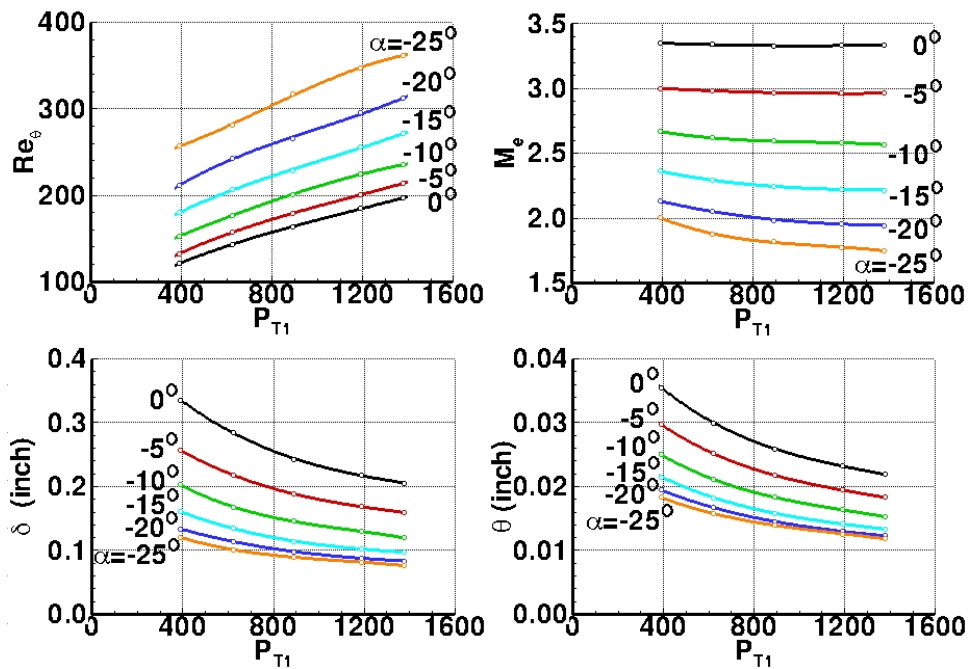
Figure 4.- Flat plate performance chart.
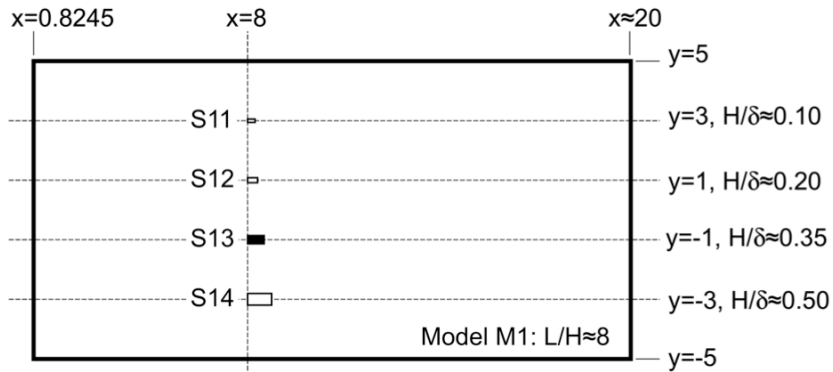
a) Shallow Cavity Model M1: Depth Variation.
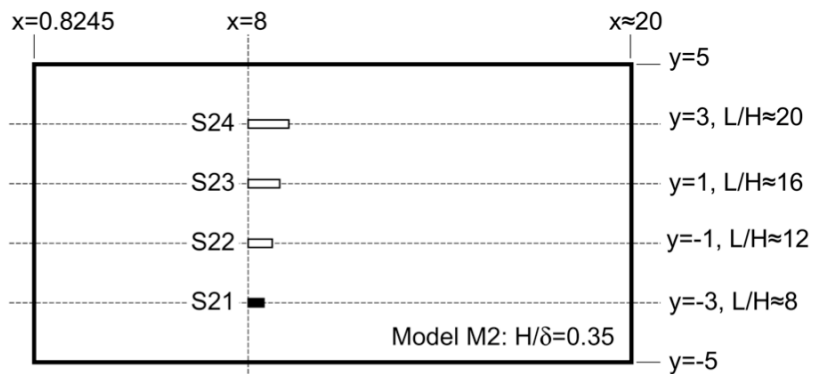
b) Shallow Cavity Model M2: Length Variation.

Figure 5.- Schematic of cavity locations. Design W/H=3.6. All dimensions are in inches. Filled cavity is common to both models.
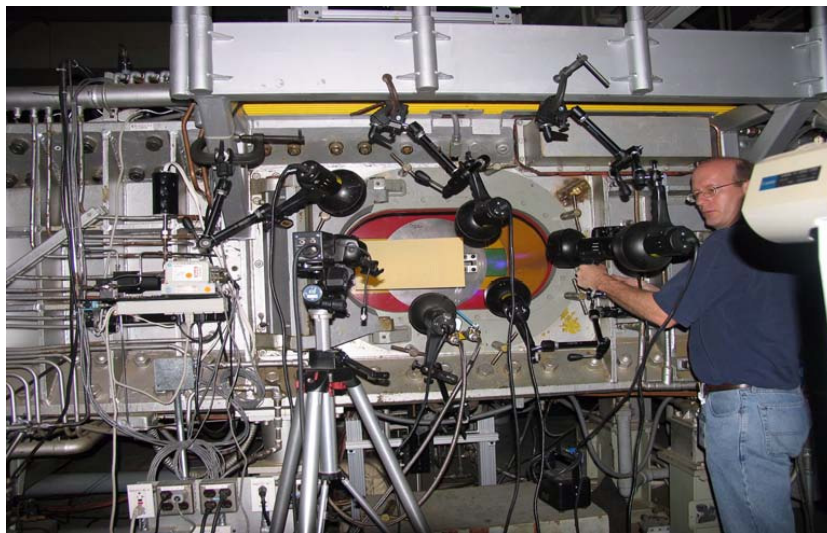
Figure 6.-Test model installed in 31-Inch Mach 10 Tunnel with TGP lighting and camera system.
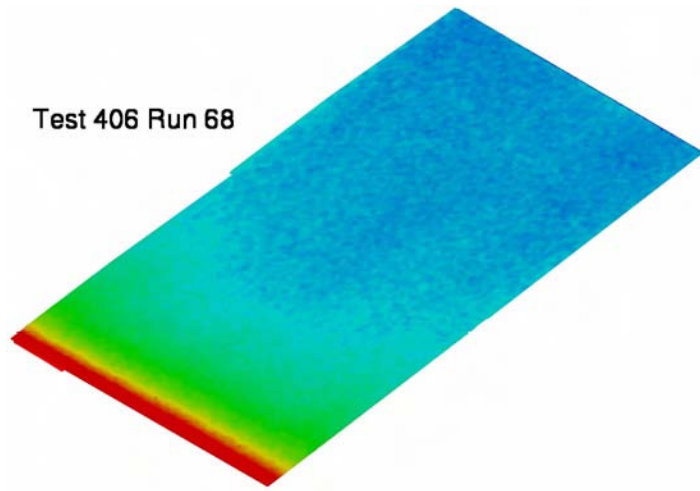
a) Test 406 Run 68.
Figure 7.- Baseline Bump Factor Images.
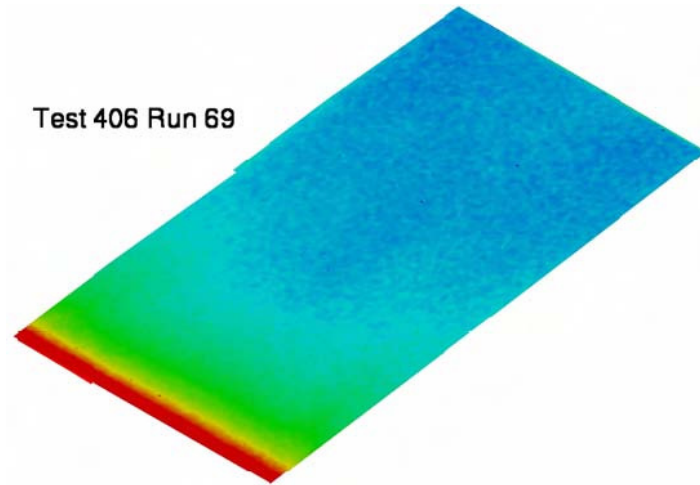
b) Test 406 Run 69.
Figure 7.- Continued.
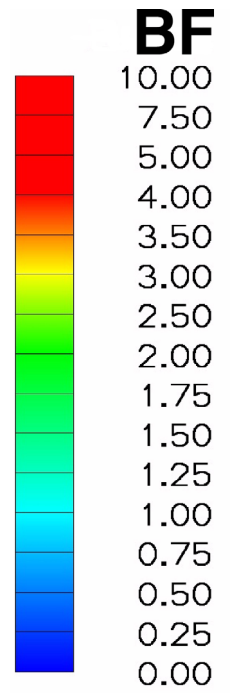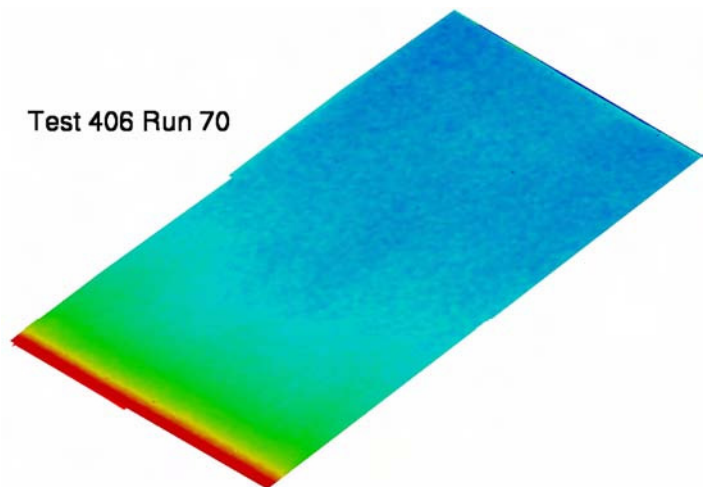
c) Test 406 Run 70.
Figure 7.- Continued.
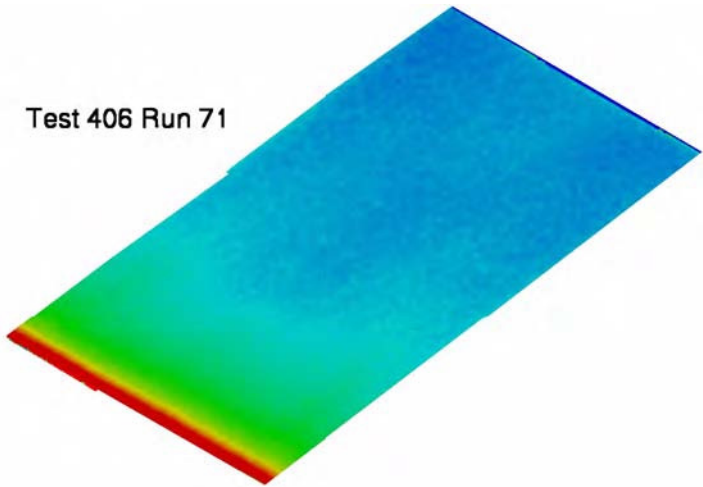
d) Test 406 Run 71.
Figure 7.- Continued.
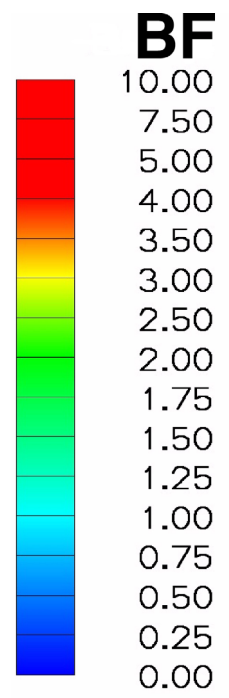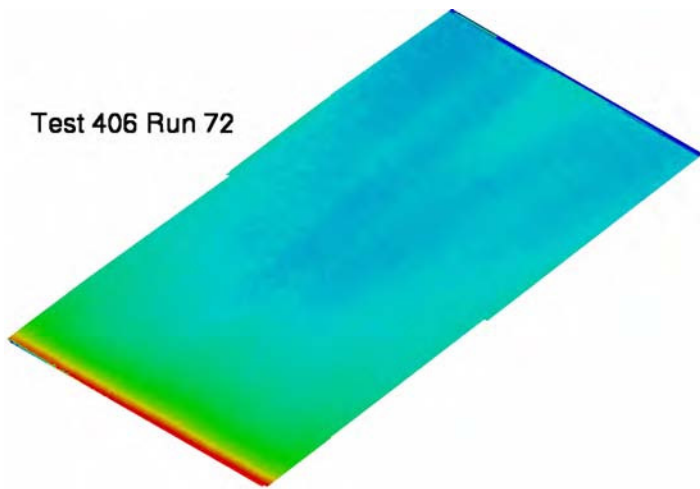
e) Test 406 Run 72.
Figure 7.- Continued.
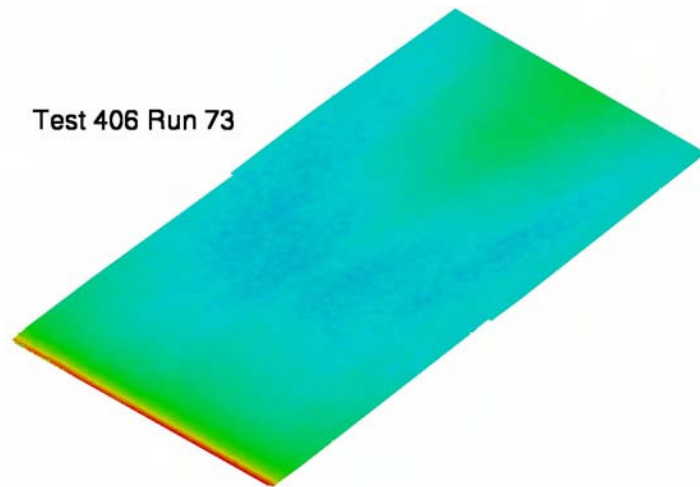
f) Test 406 Run 73.
Figure 7.- Continued.
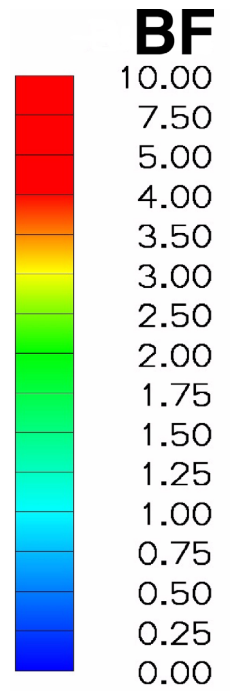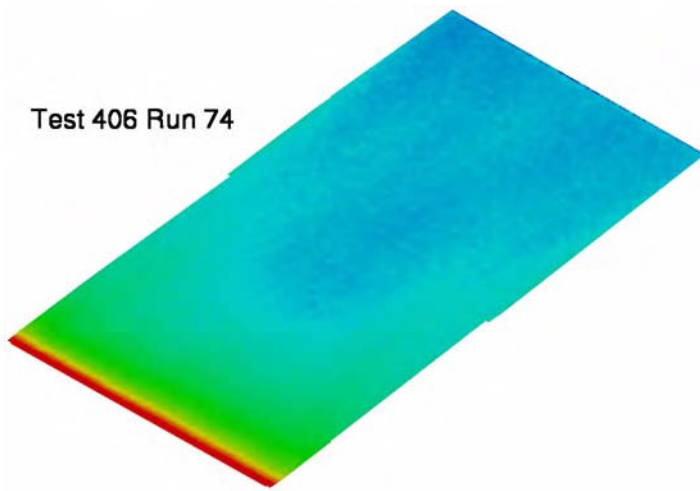
g) **Test 406 Run 74**.
Figure 7.- Continued.
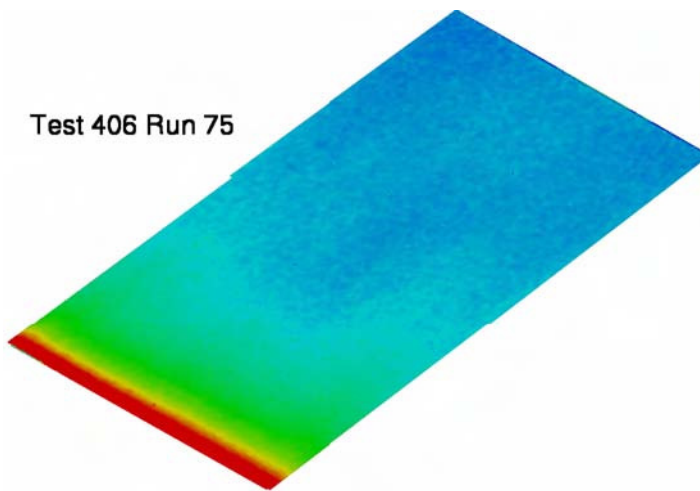
h) **Test 406 Run 75.**
Figure 7.- Concluded.
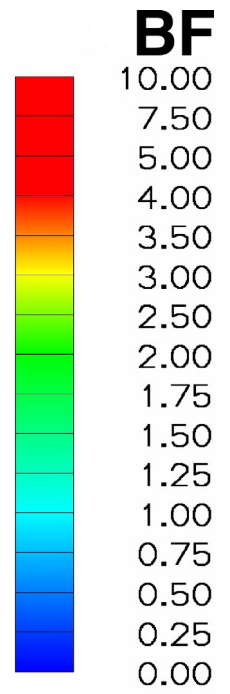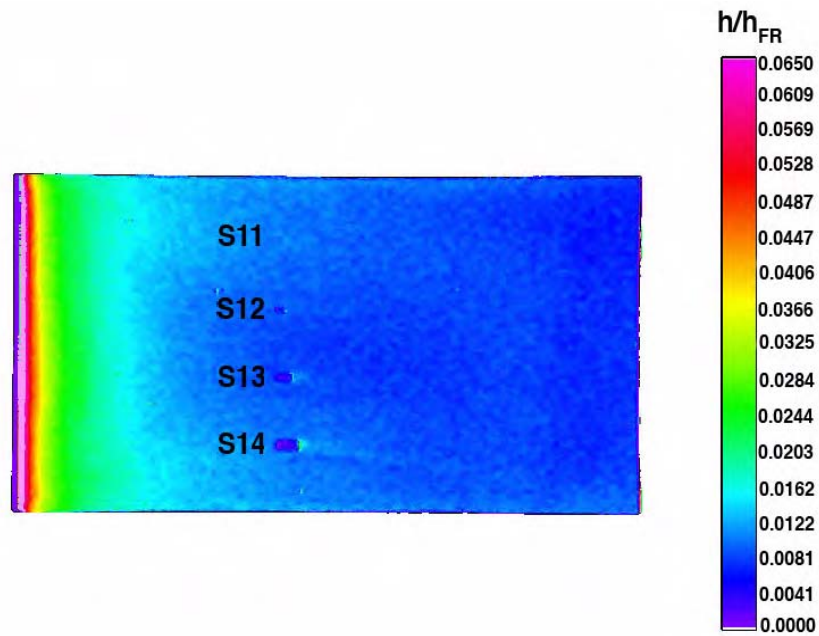
a) Test 404 Run 02 −− M_∞=9.7, α=-7.77°, Re_∞=0.92x10^6/ft.

Figure 8.- Global heating images of Cavity Model 1.
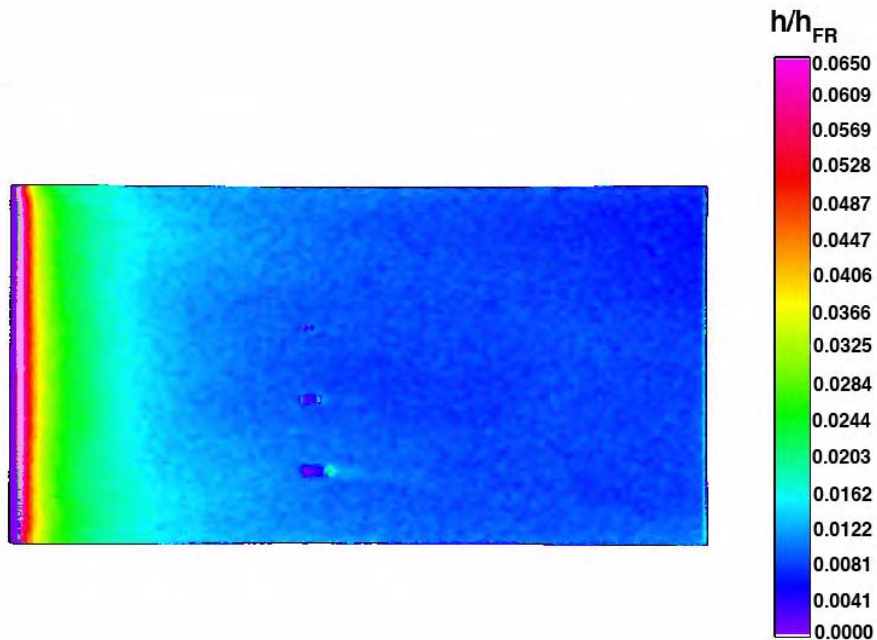
b) Test 404 Run 07 −− M_∞=9.7, α=-7.20°, Re_∞=1.19x10^6/ft.
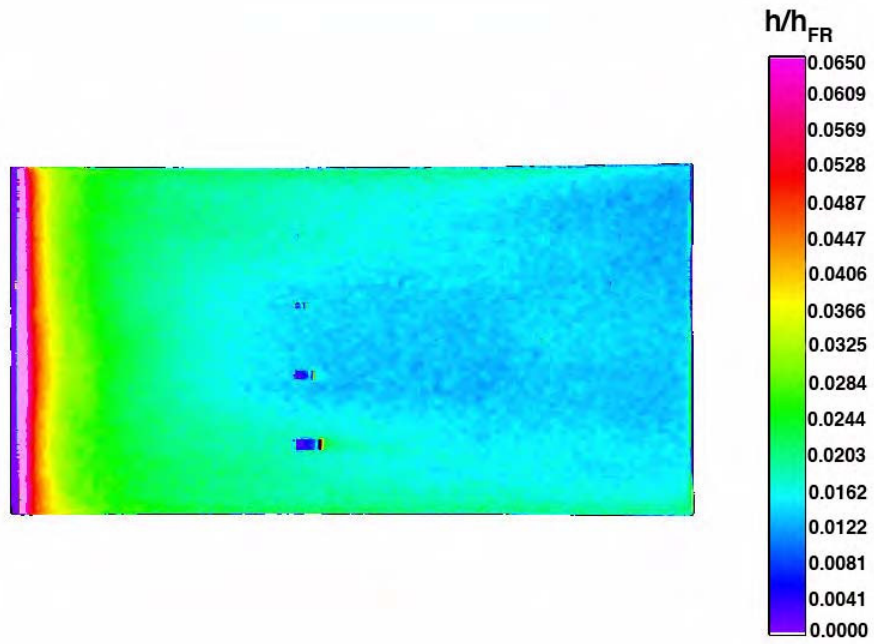
Figure 8.- Continued.

c) **Test 404 Run 08** −− M_∞=9.5, α=-14.18°, Re_∞=0.80x10^6/ft.
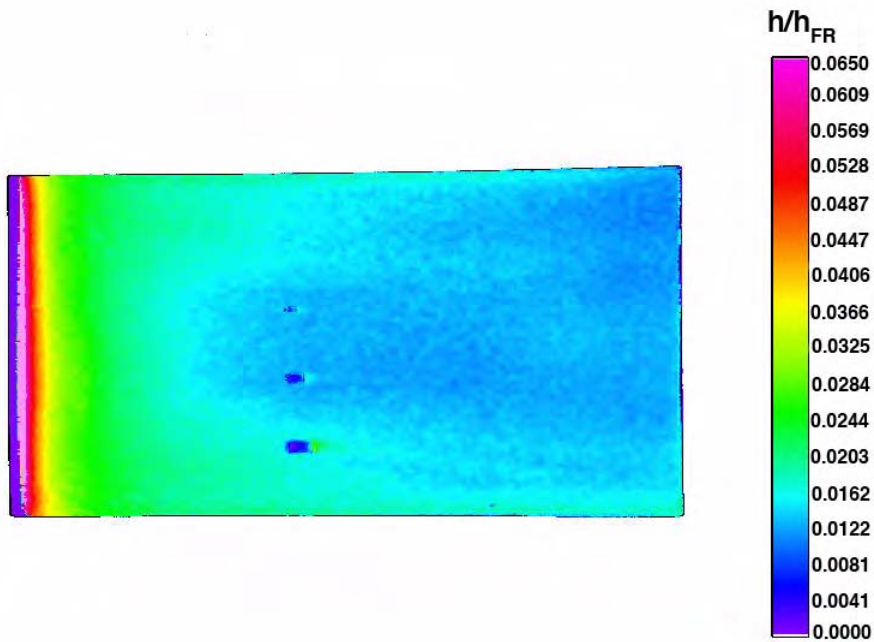
Figure 8.- Continued.

d) **Test 404 Run 13** −− M_∞=9.7, α=-12.39°, Re_∞=1.24x10^6/ft.
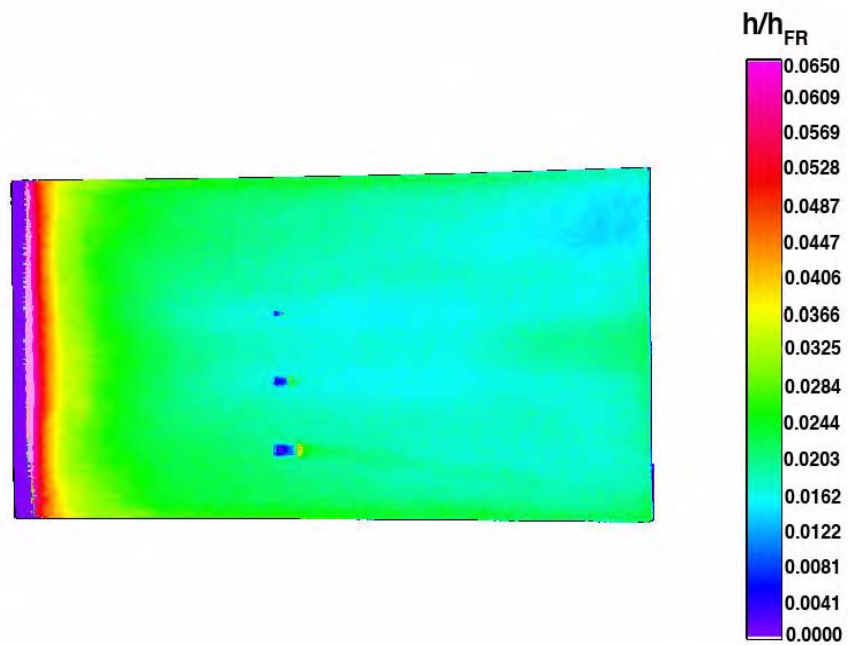
Figure 8.- Continued.

e) Test 404 Run 14 −− M_∞=9.8, α=-15.57°, Re_∞=1.73x10^6/ft.
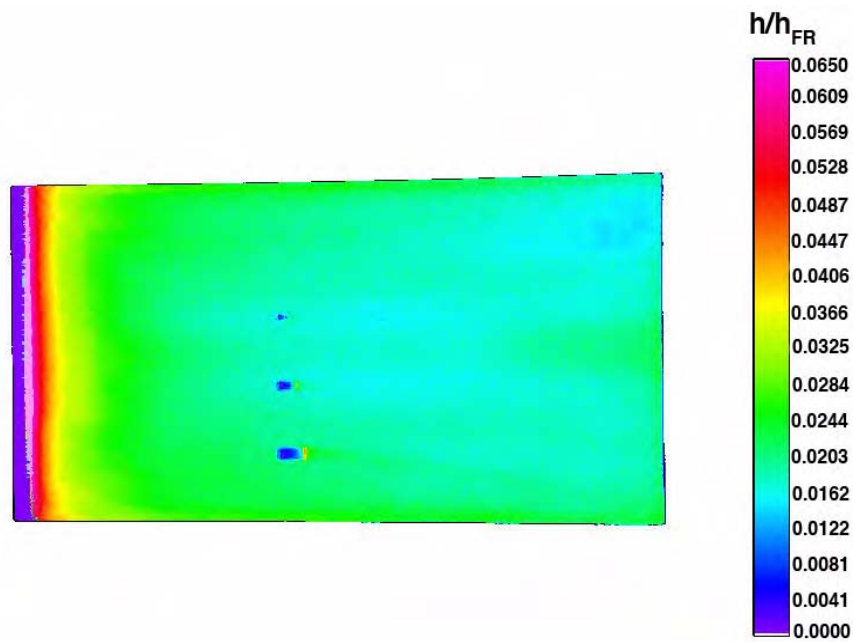
Figure 8.- Continued.

f) Test 404 Run 15 −− M_∞=9.8, α=-15.57°, Re_∞=1.77x10^6/ft.

Figure 8.-Concluded.
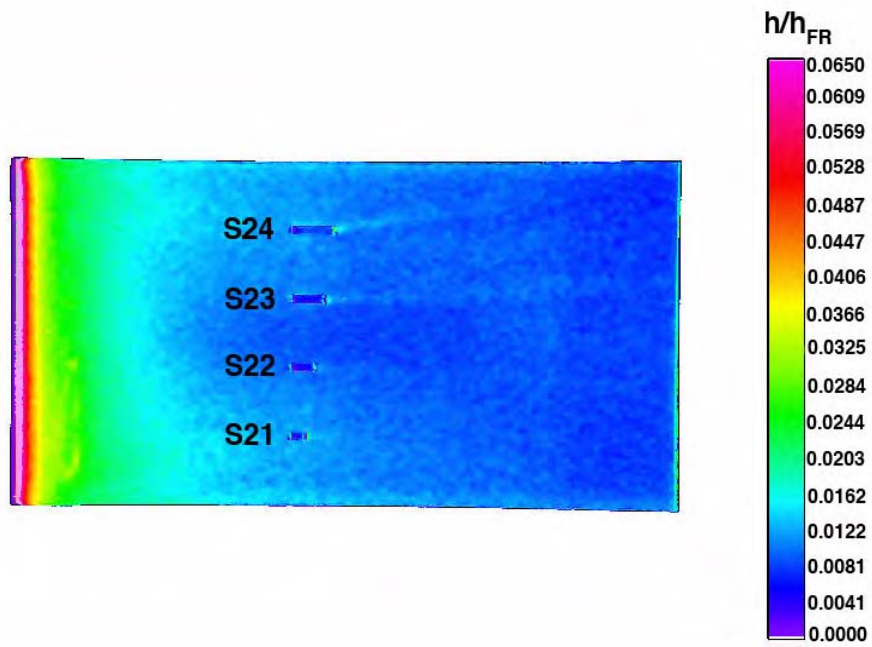
a) Test 404 Run 27 −− M_∞=9.6, α =-7.77°, Re_∞=0.92x10^6/ft.

Figure 9.- Global heating images of Cavity Model 2.
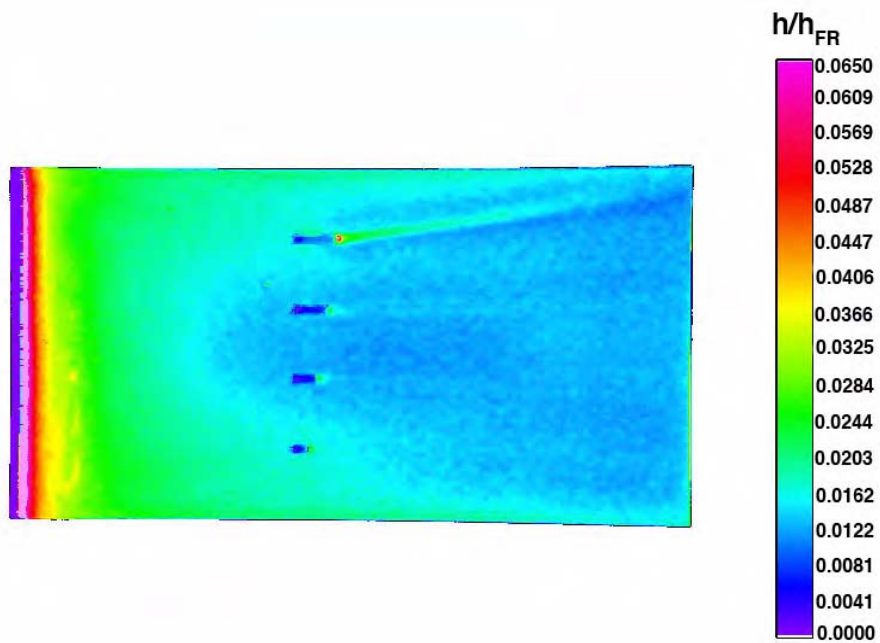
b) Test 404 Run 33 −− M_∞ =9.7, α=-12.39°, Re_∞=1.25x10^6/ft.

Figure 9.- Continued.
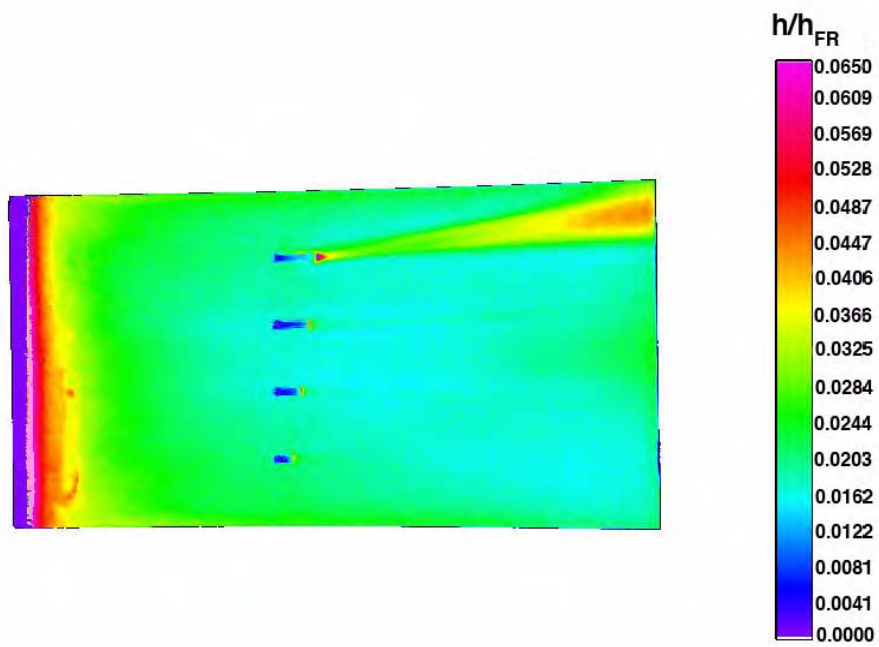
c) Test 404 Run 38 −− M_∞=9.8, α=-15.57°, Re_∞=1.74x10^6/ft.

Figure 9.-Concluded.
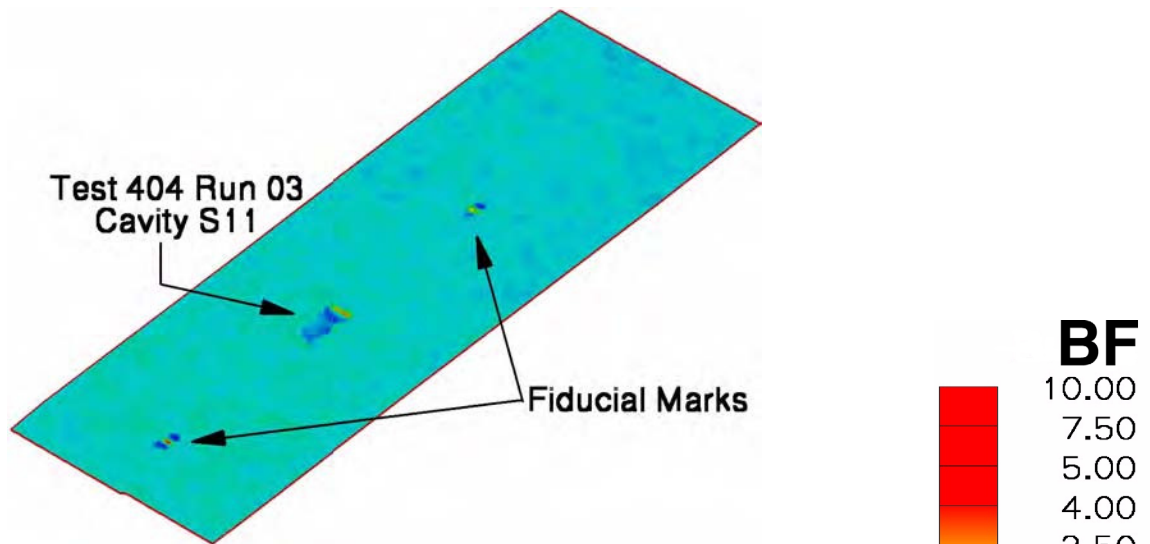
a) Test 404 Run 03 - H/δ=0.093.

Figure 10.- Bump factor distributions for Cavity S11 - L/H=6.6, W/H=3.33.
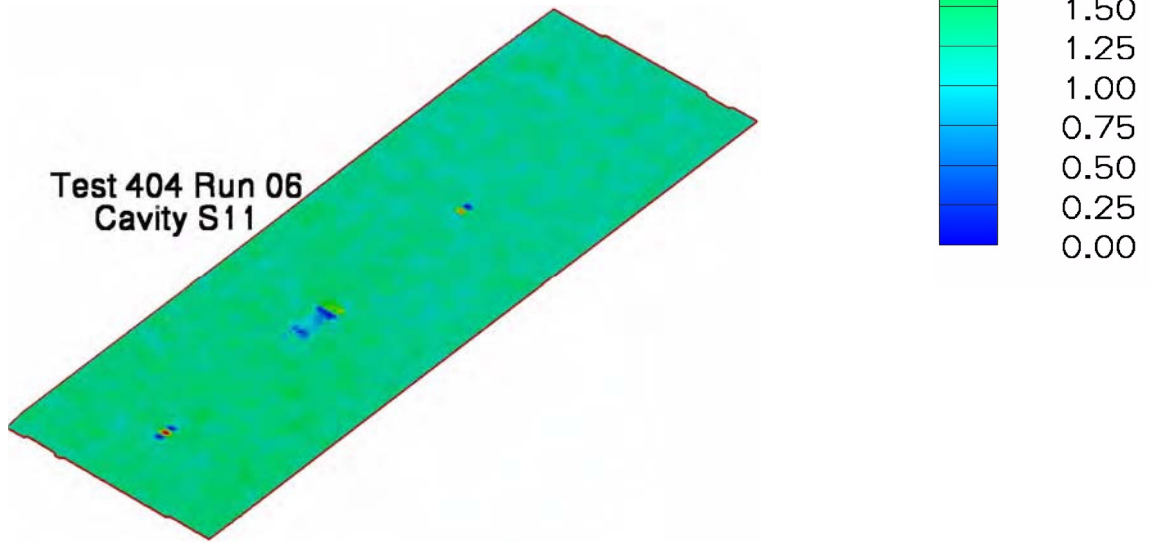
b) Test 404 Run 06 -H/δ=0.102.

Figure 10.- Continued.
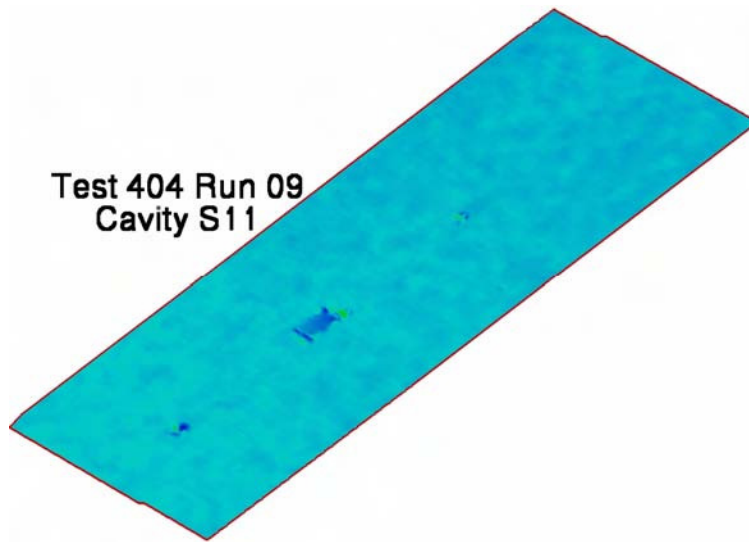
c) Test 404 Run 09 - H/δ=0.120.

Figure 10.- Continued.
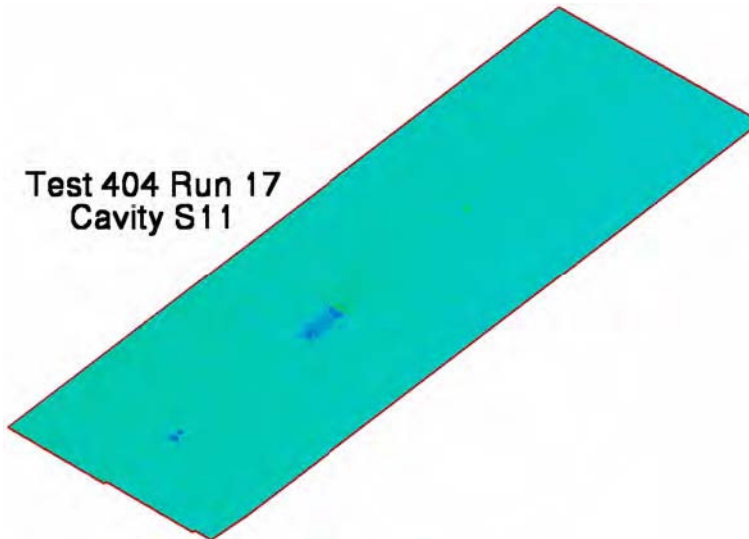
d) Test 404 Run 17 -H/δ=0.180.

Figure 10.- Continued.
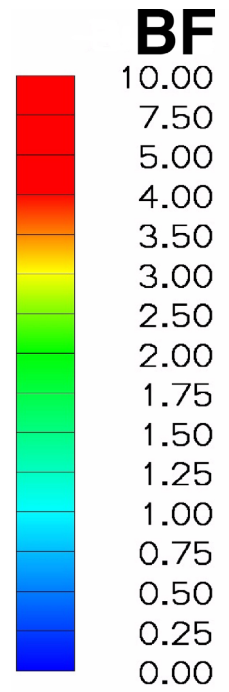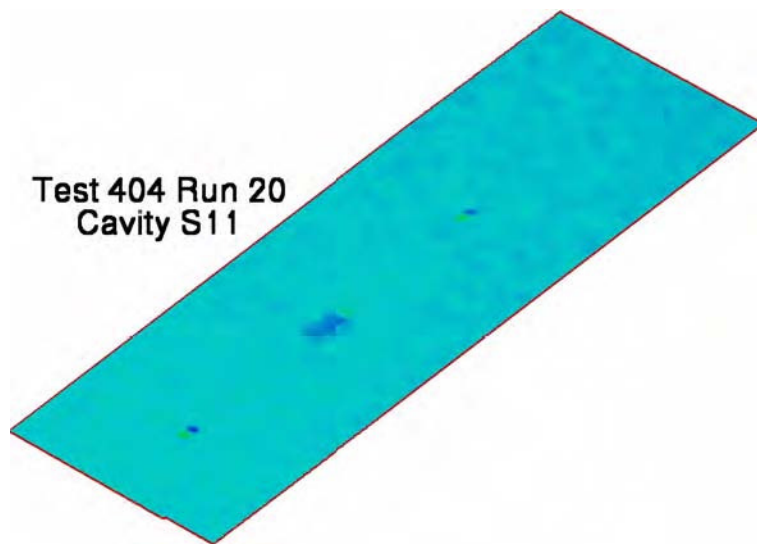
Test 404 Run 20
Cavity S11

BF
10.00
7.50
5.00
4.00
3.50
3.00
2.50
2.00
1.75
1.50
1.25
1.00
0.75
0.50
0.25
0.00

e) Test 404 Run 20 - H/δ=0.144.

Figure 10.- Continued.
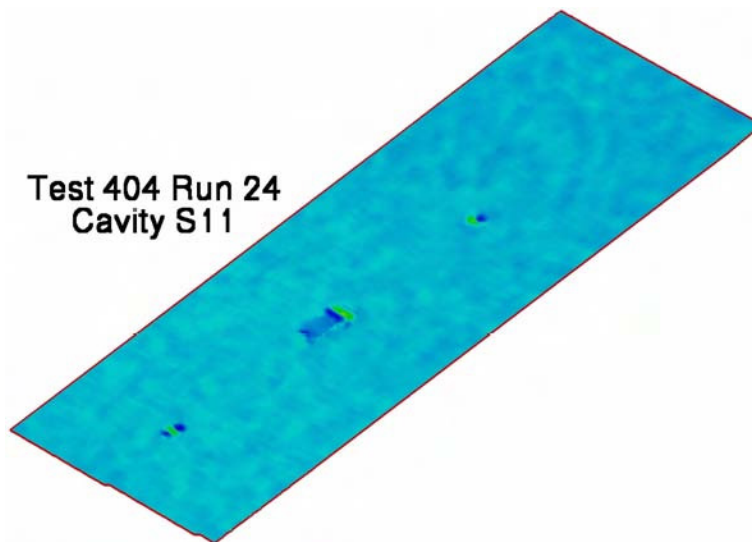
Test 404 Run 24
Cavity S11

f) Test 404 Run 24 - H/δ=0.111.

Figure 10.- Continued.
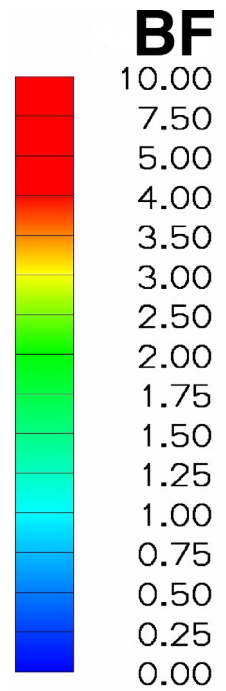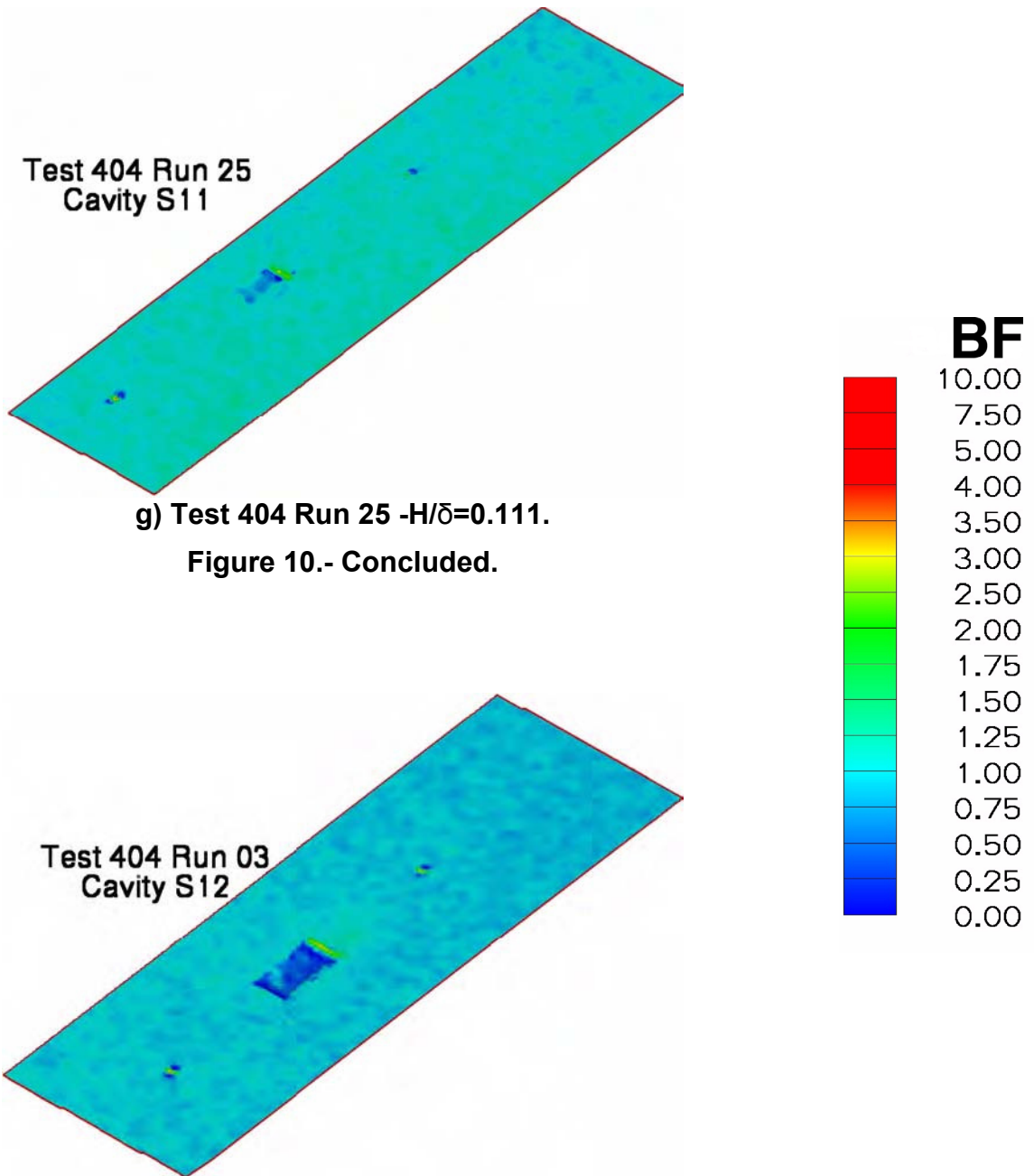
g) Test 404 Run 25 -H/δ=0.111.

Figure 10.- Concluded.

a) Test 404 Run 03 - H/δ=0.185.

Figure 11.- Bump Factor images for Cavity S12 - L/H=9.3, W/H=4.58.
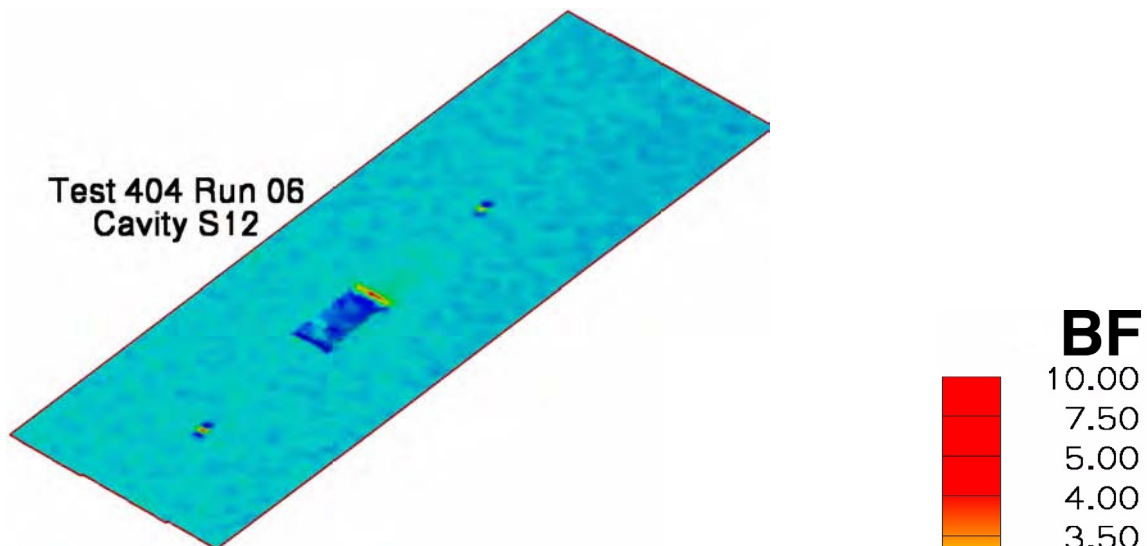
b) Test 404 Run 06 -H/δ=0.204.

Figure 11.- Continued.
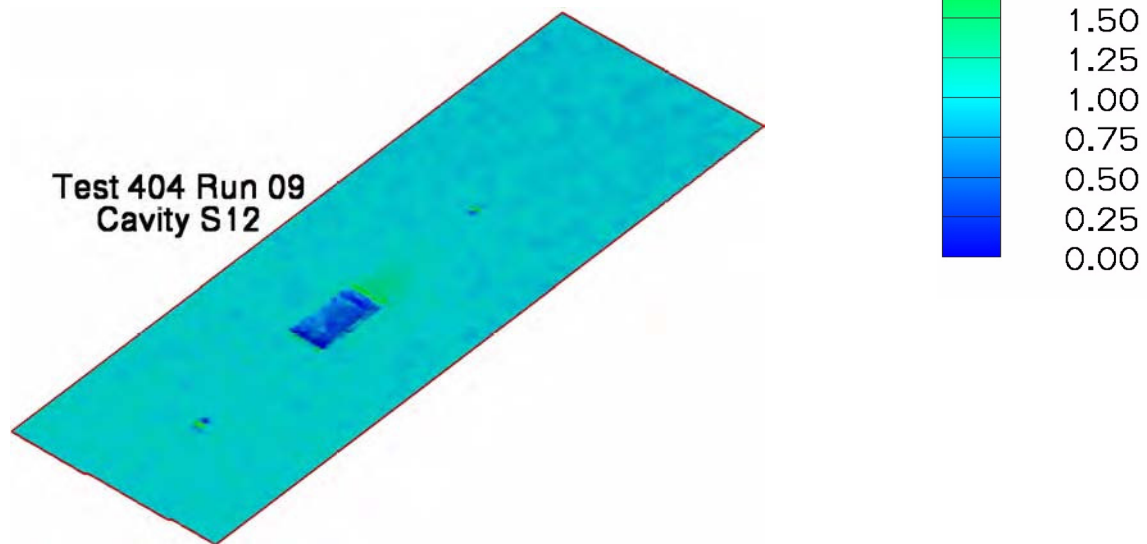
c) Test 404 Run 09 - H/δ=0.239.

Figure 11.- Continued.
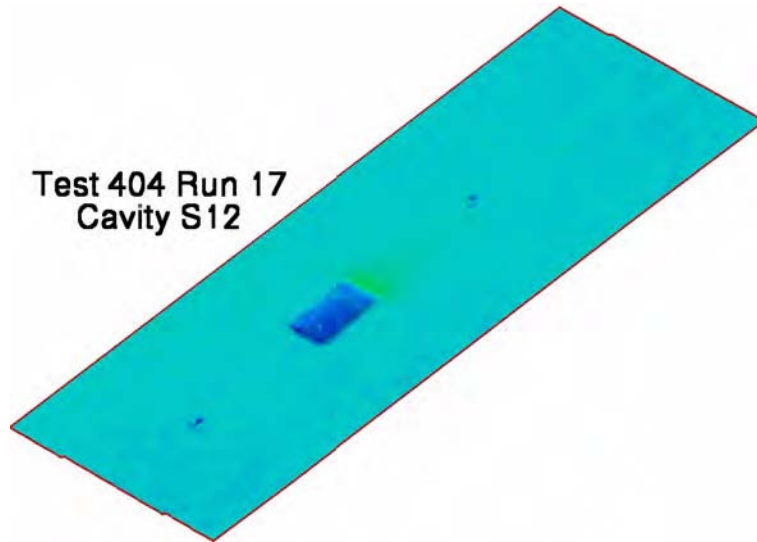
d) Test 404 Run 17 -H/δ=0.360.

Figure 11.- Continued.
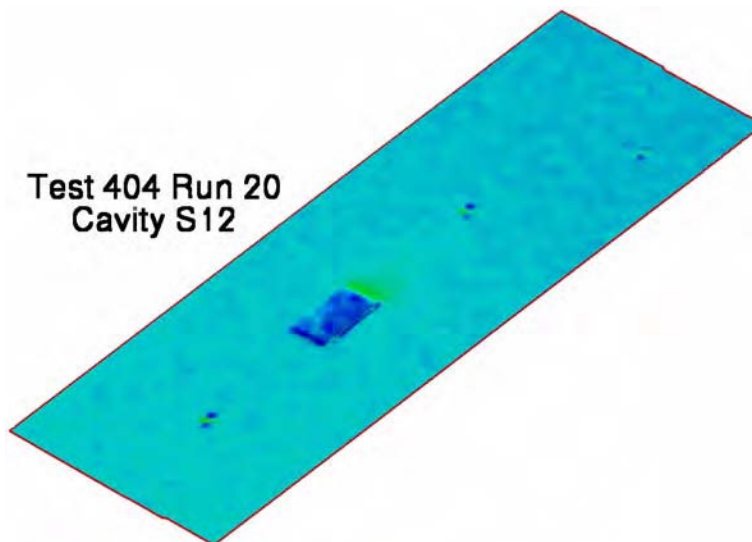
e) Test 404 Run 20 - H/δ=0.289.

Figure 11.- Continued.
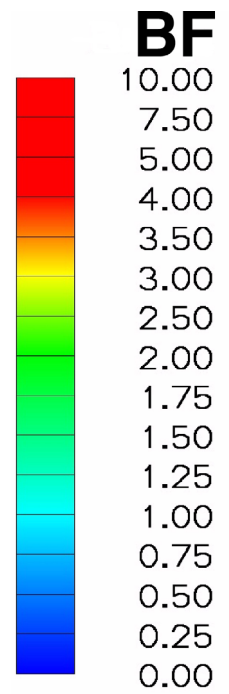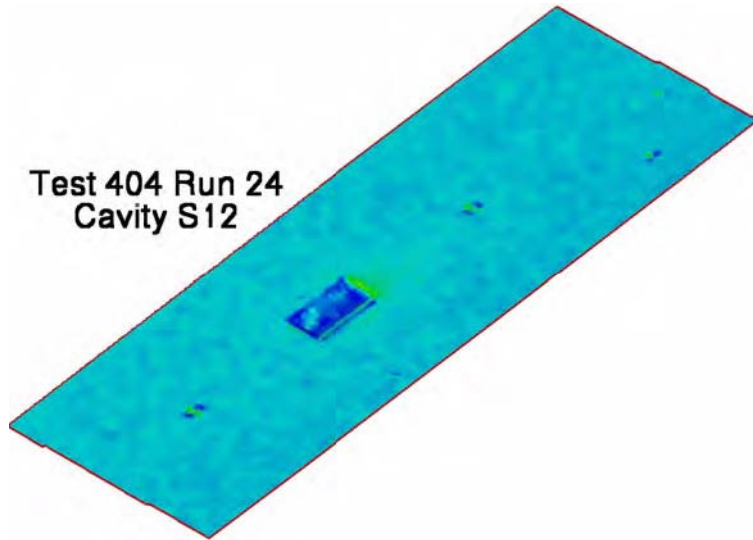
f) Test 404 Run 24 - H/δ=0.222.

Figure 11.- Continued.
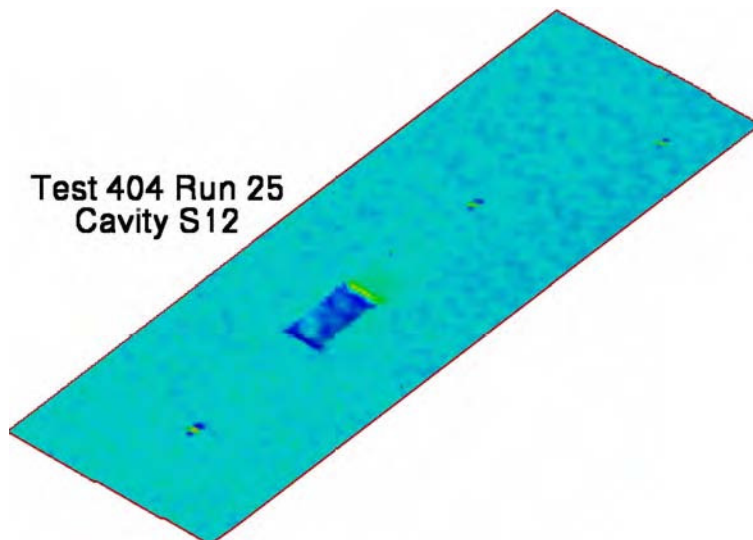
g) Test 404 Run 25 - H/δ=0.222.

Figure 11.- Concluded.
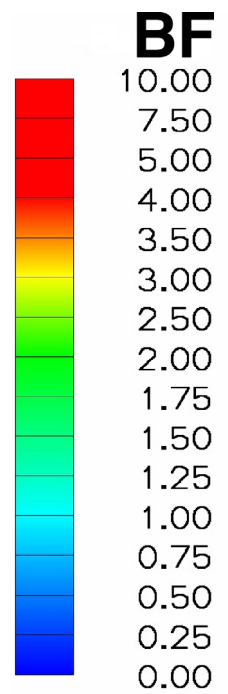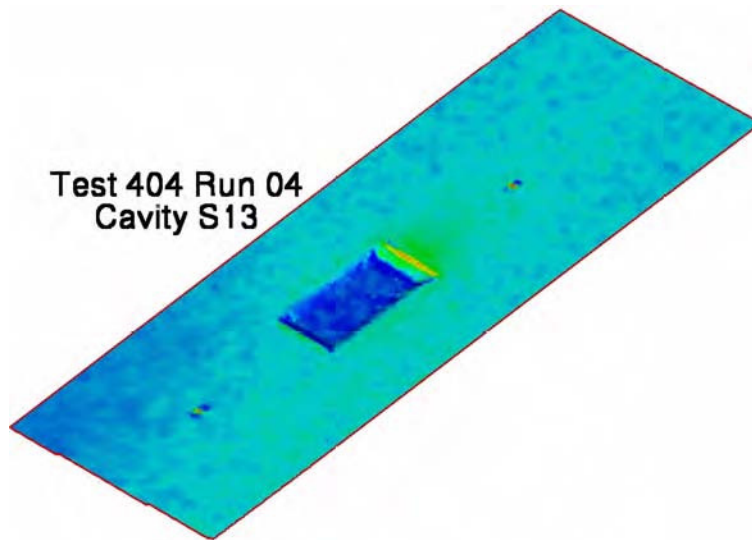
a) Test 404 Run 04 - H/δ=0.324.

Figure 12.- Bump Factor images for Cavity S13 - L/H=8.7, W/H=4.29.
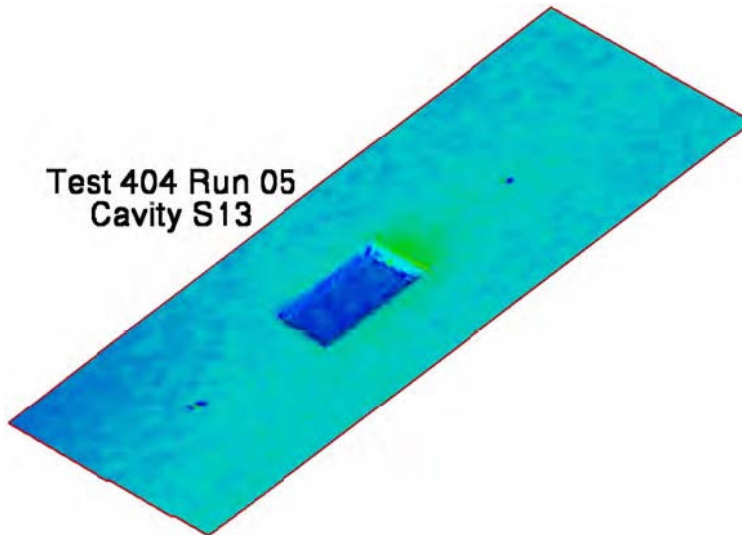
b) Test 404 Run 05 - H/δ=0.356.

Figure 12.- Continued.
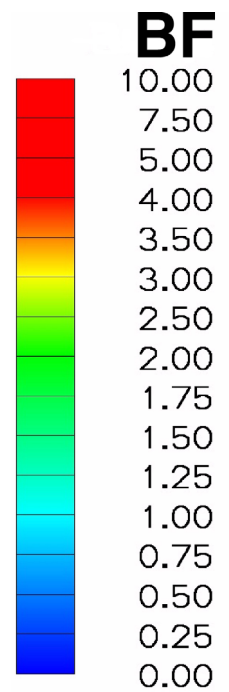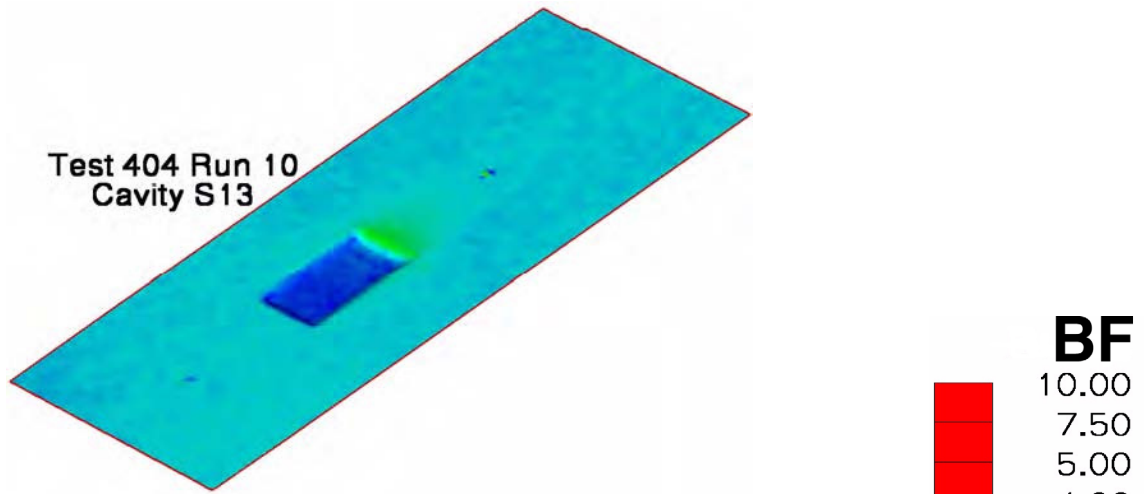
c) Test 404 Run 10 - H/δ=0.419.

Figure 12.- Continued.
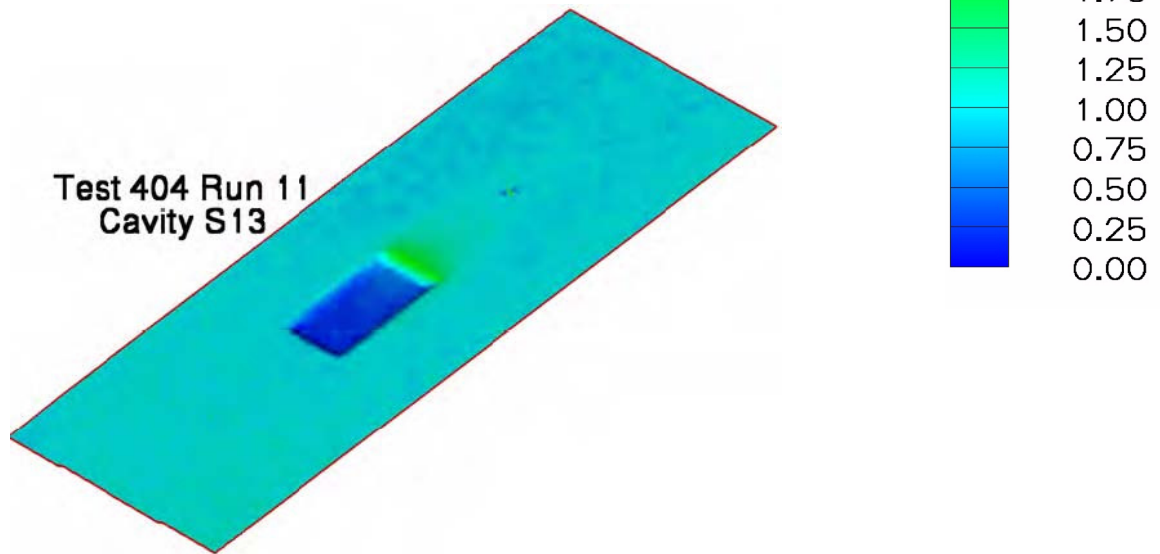
d) Test 404 Run 11 - H/δ=0.419.

Figure 12.- Continued.
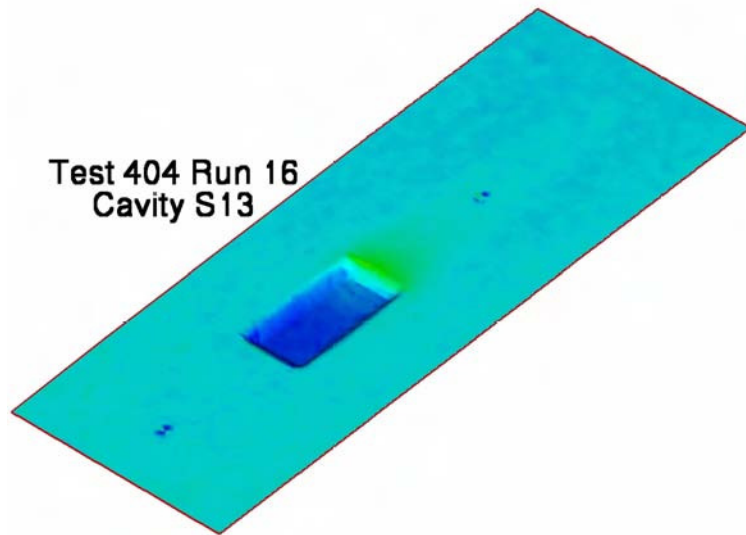
e) Test 404 Run 16 - H/δ=0.631.

Figure 12.- Continued.
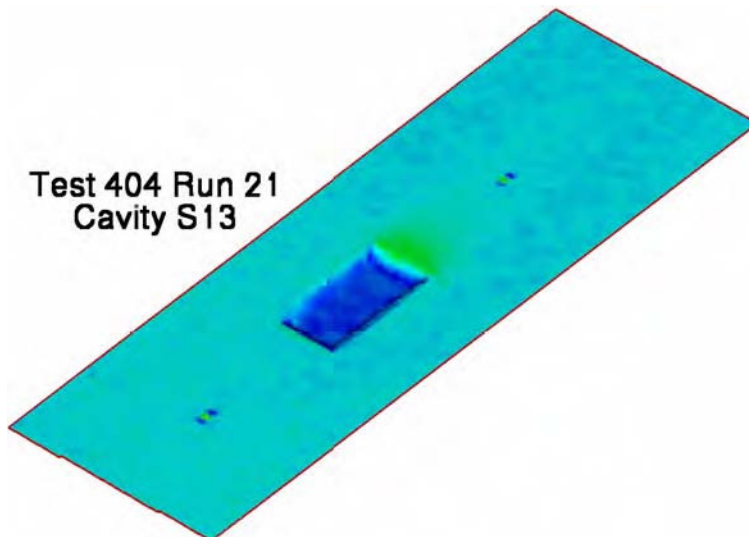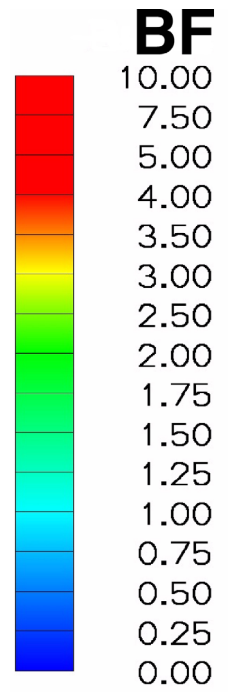
f) Test 404 Run 21 - H/δ=0.505.

Figure 12.- Continued.
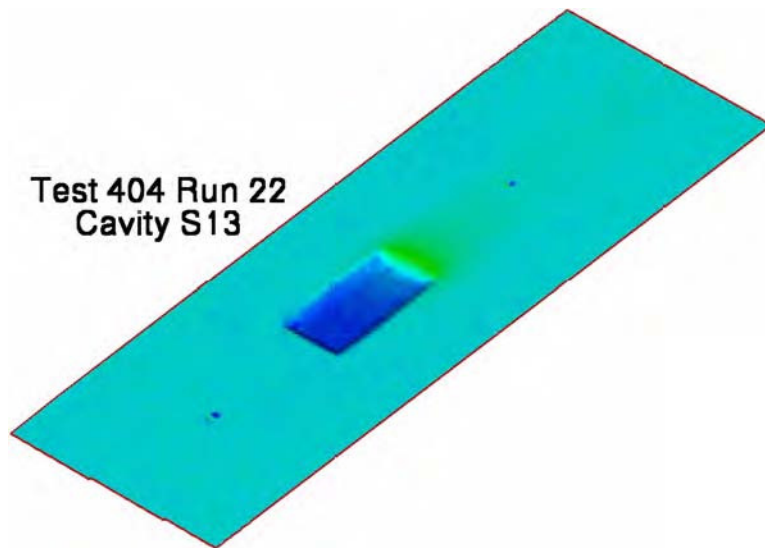
g) Test 404 Run 22 - H/δ=0.566.

Figure 12.- Continued.
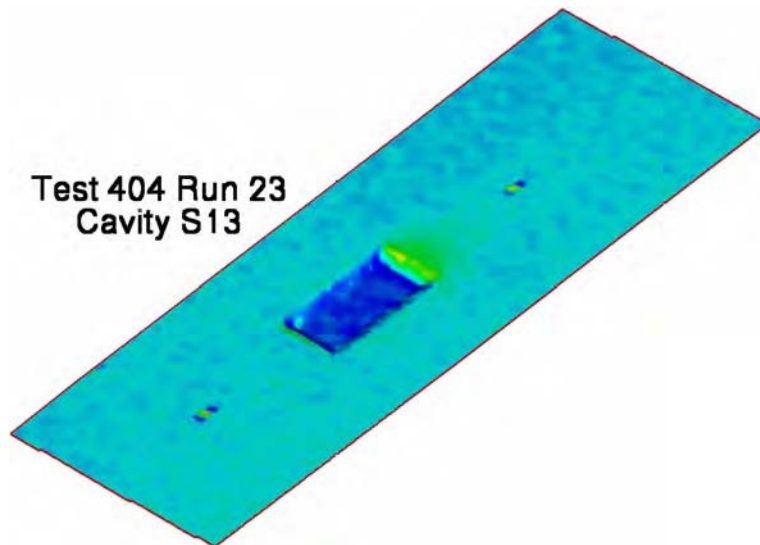
h) Test 404 Run 23 - H/δ=0.388.

Figure 12.- Concluded.
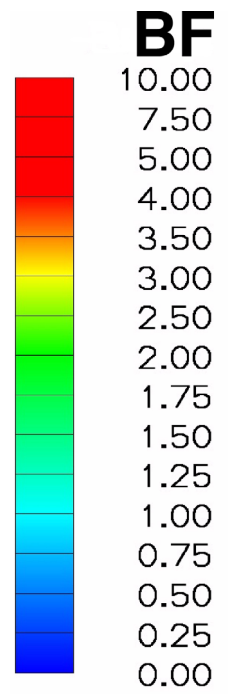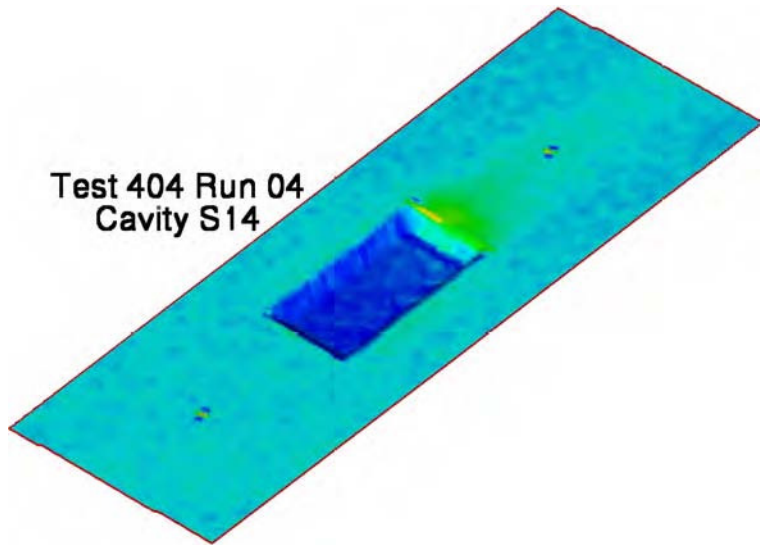
a) Test 404 Run 04 - H/δ=0.324.

Figure 13.- Bump Factor images for Cavity S14 -
L/H=8.1, W/H=3.95.
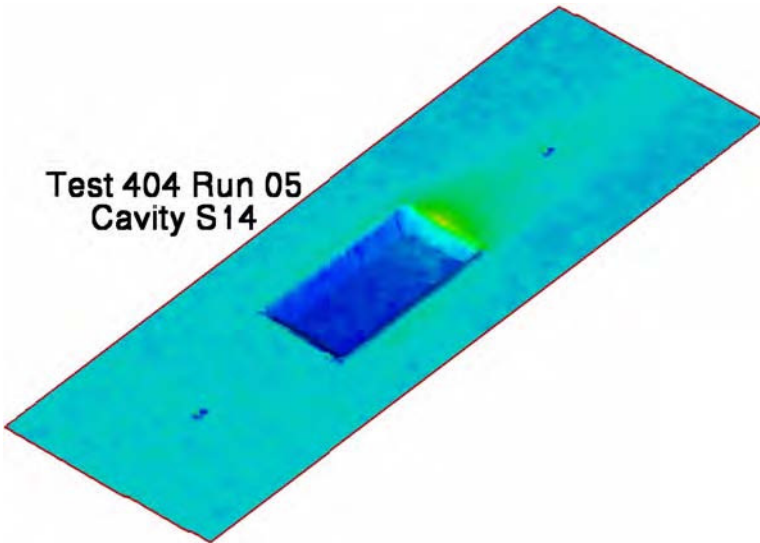
b) Test 404 Run 05 - H/δ=0.356.

Figure 13.- Continued.
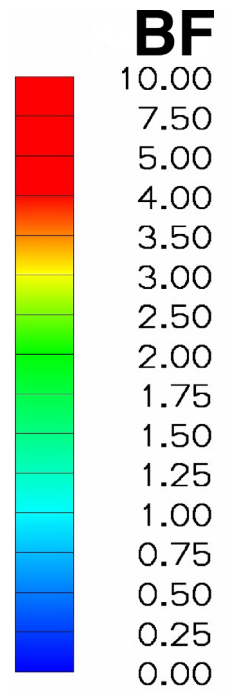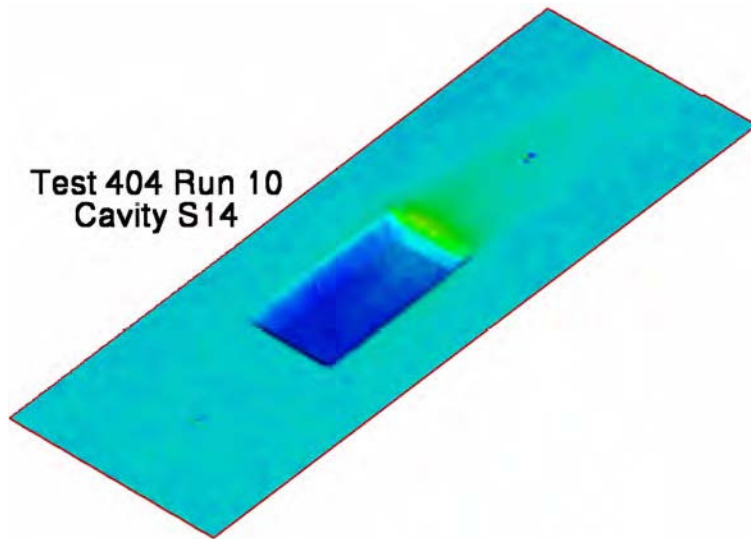
c) Test 404 Run 10 - H/δ=0.658.

Figure 13.- Continued.
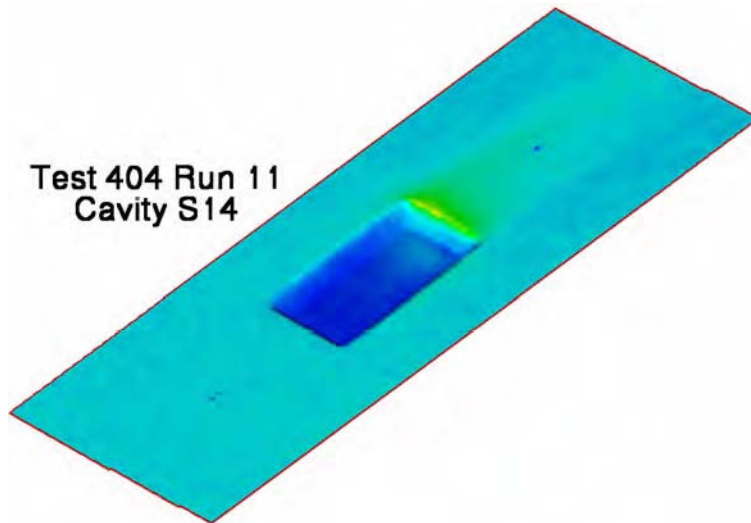
d) Test 404 Run 11 -H/δ=0.737.

Figure 13.- Continued.
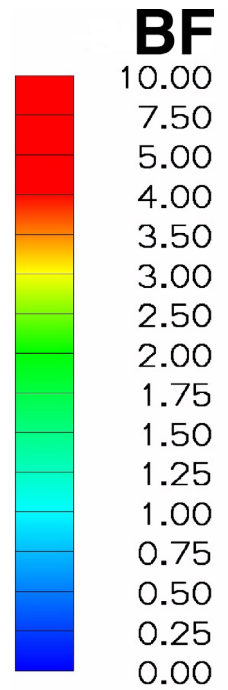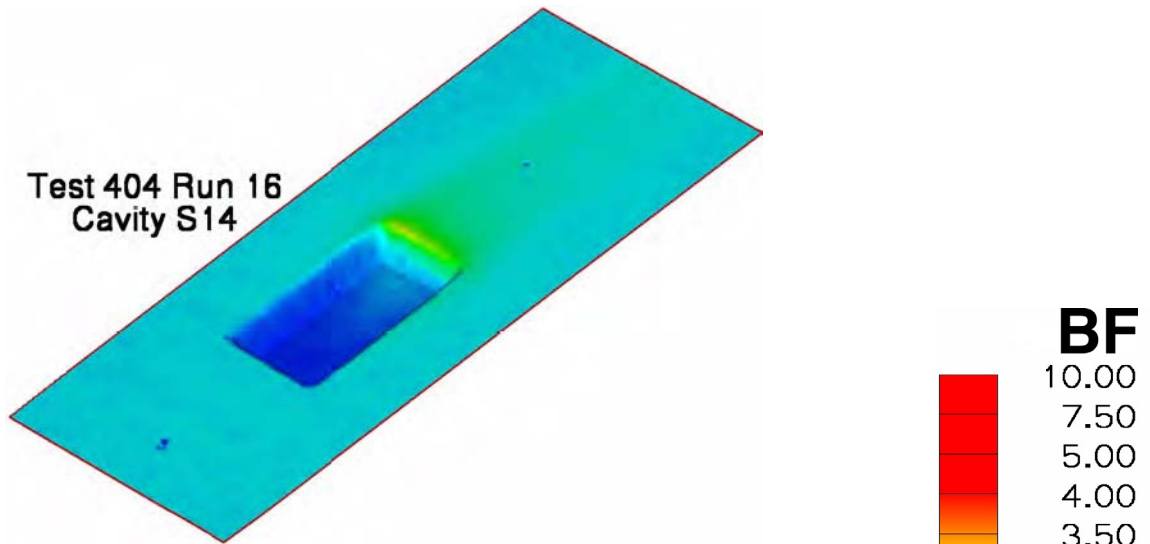
e) Test 404 Run 16 - H/δ=0.992.

Figure 13.- Continued.
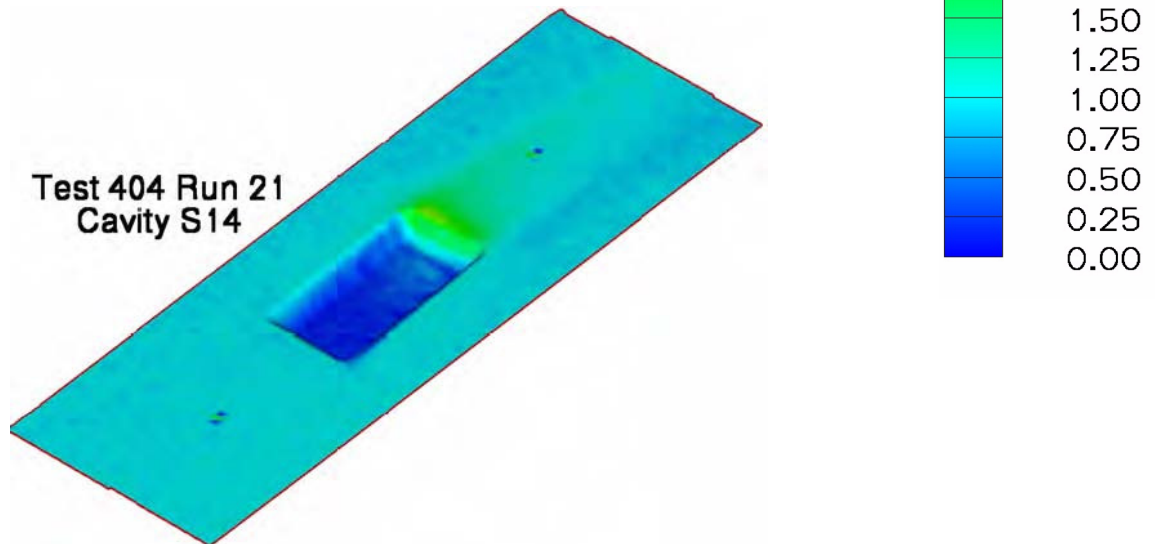
f) Test 404 Run 21 - H/δ=0.794.

Figure 13.- Continued.
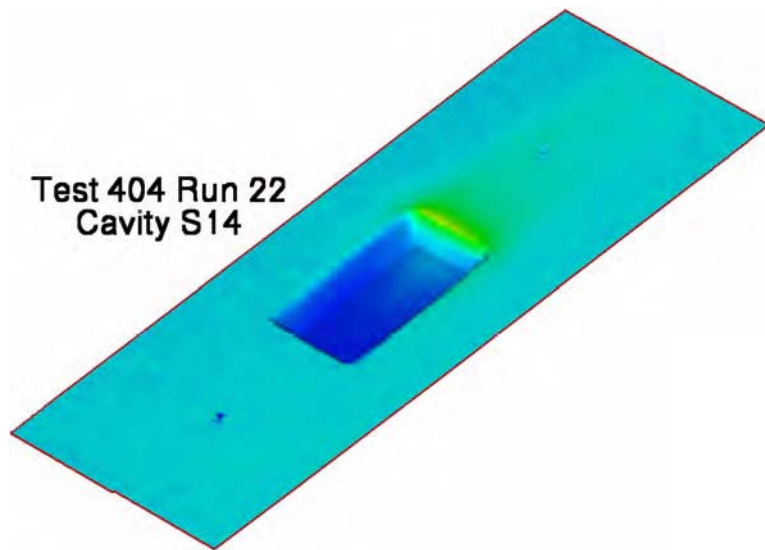
g) Test 404 Run 22 - H/δ=0.889.

Figure 13.- Continued.
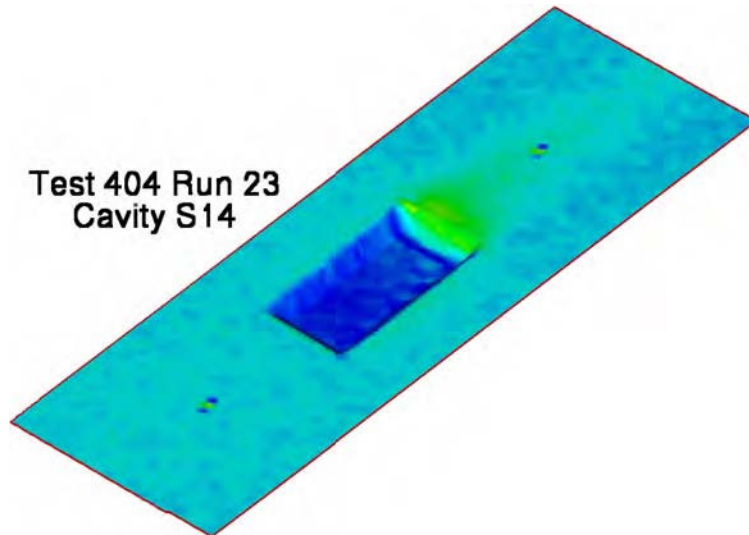
h) Test 404 Run 23 - H/δ=0.610.

Figure 13.- Concluded.
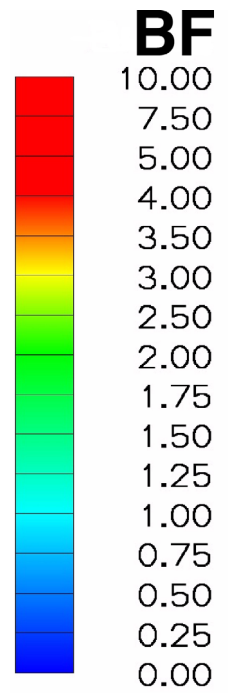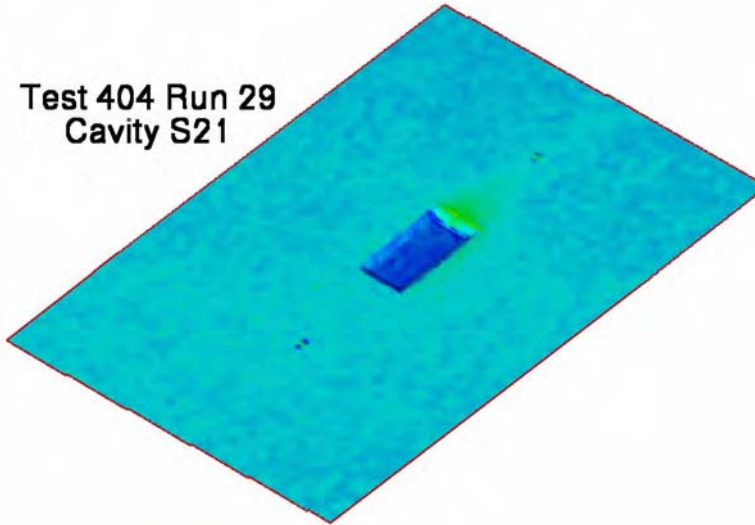
a) Test 404 Run 29 - H/δ=0.350.

Figure 14.- Bump Factor images for Cavity S21 - L/H=10.7, W/H=4.0.
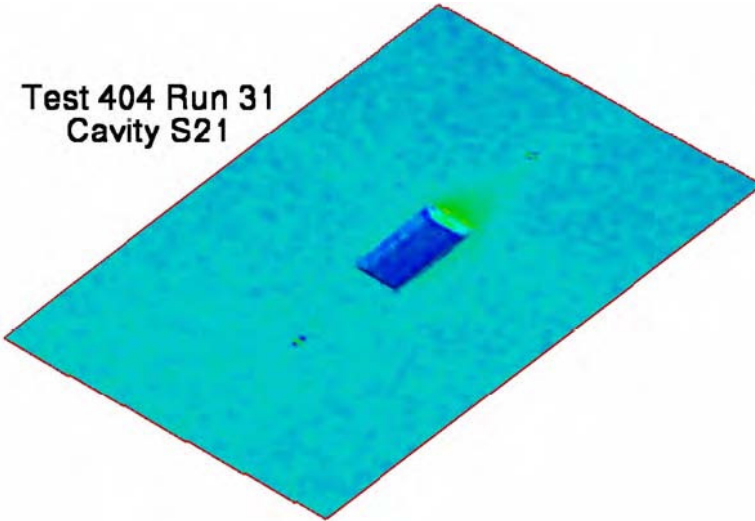
b) Test 404 Run 31 - H/δ=0.384.

Figure 14.- Continued.
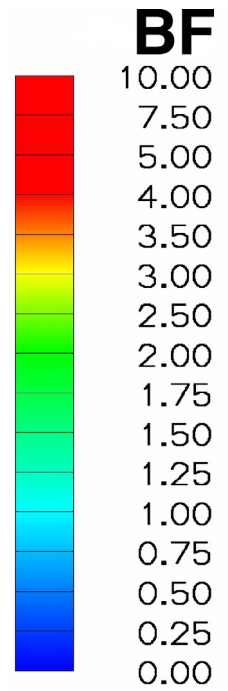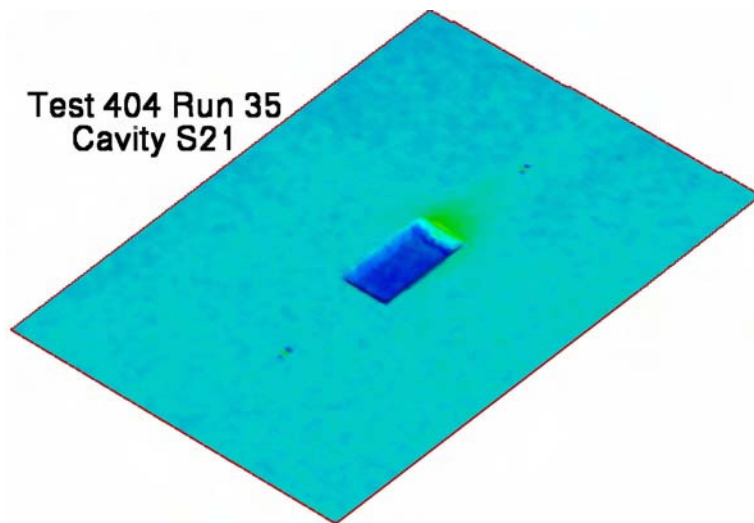
c) Test 404 Run 35 - H/δ=0.506.

Figure 14.- Continued.
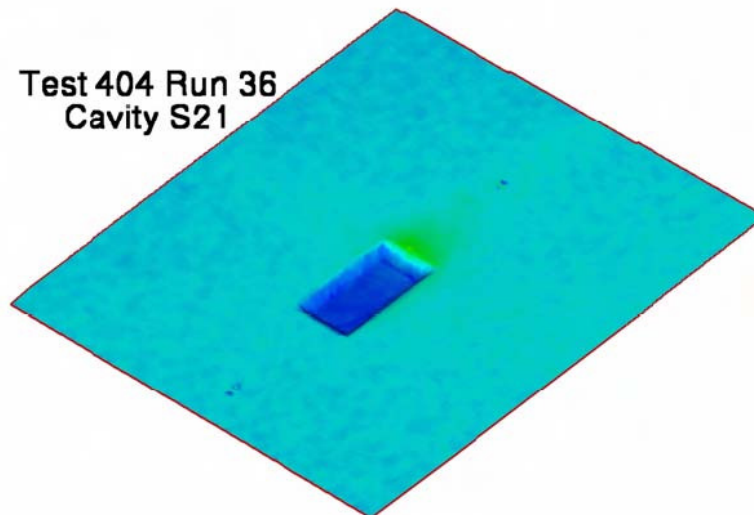
d) Test 404 Run 36 - H/δ=0.451.

Figure 14.- Continued.
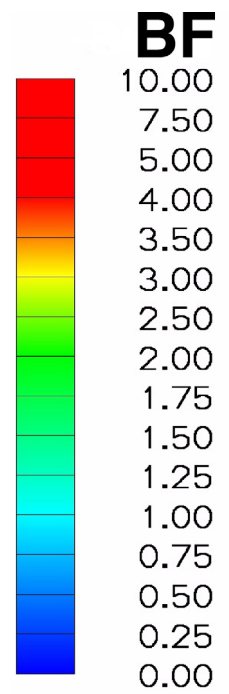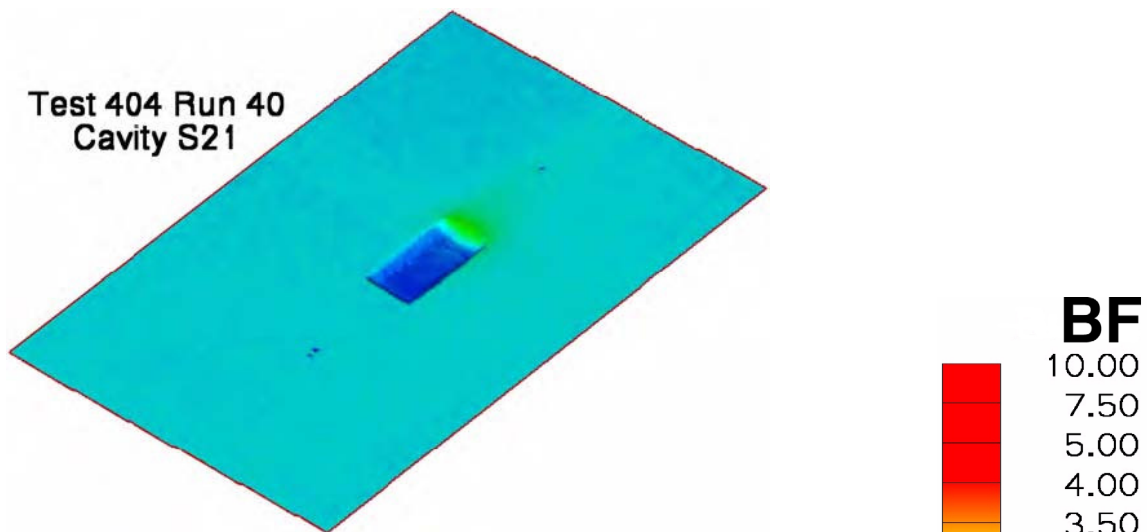
e) Test 404 Run 40 - H/δ=0.682.

Figure 14.- Continued.
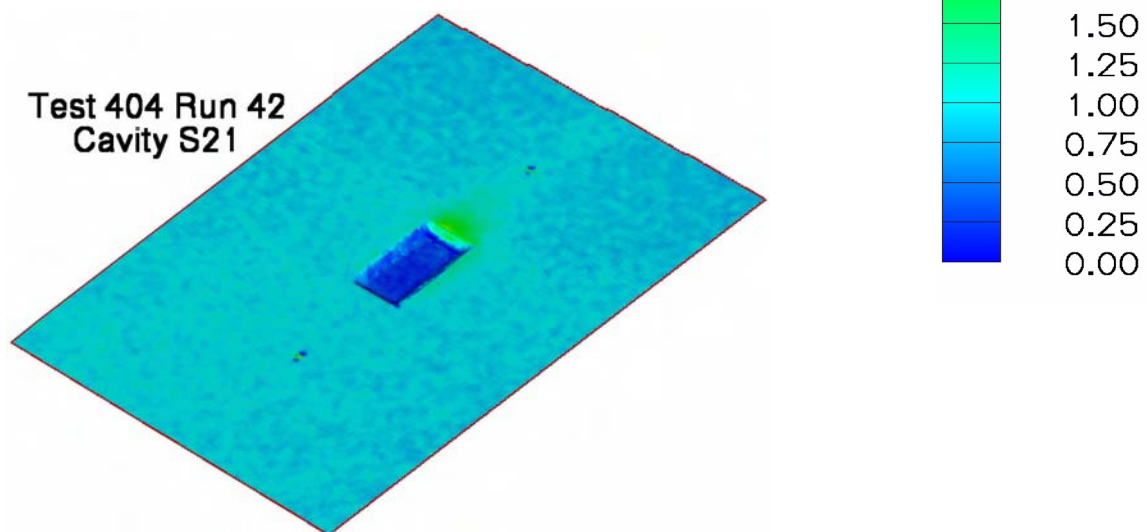
f) Test 404 Run 42 - H/δ=0.419.

Figure 14.- Continued.
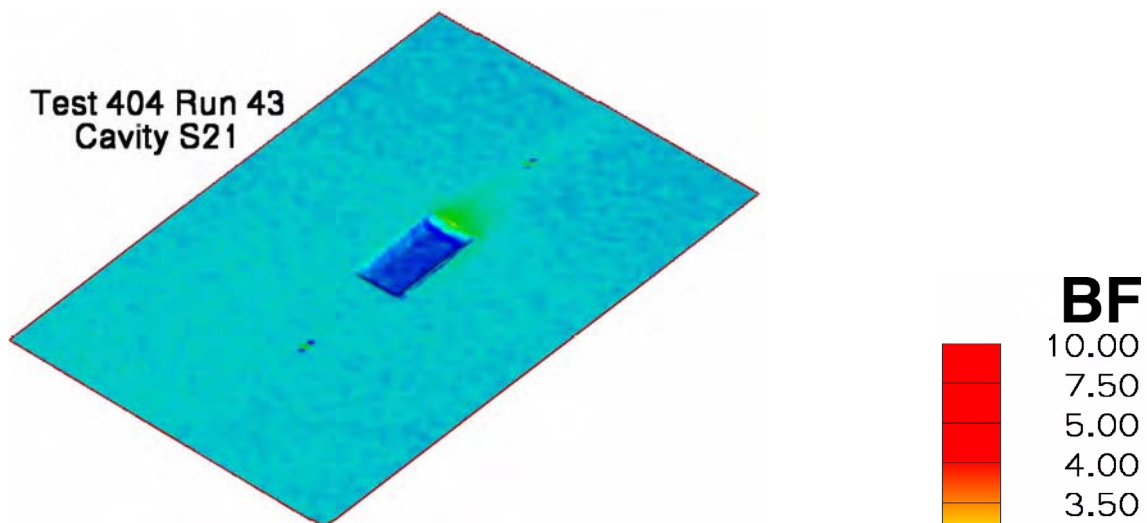
g) Test 404 Run 43 - H/δ=0.453.

Figure 14.- Continued.
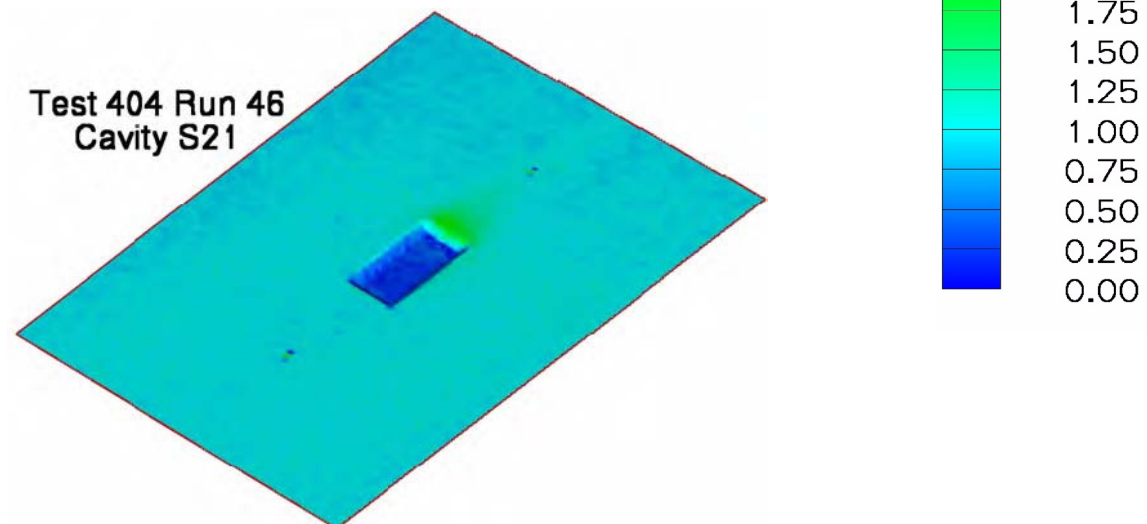
h) Test 404 Run 46 - H/δ=0.545.

Figure 14.- Continued.
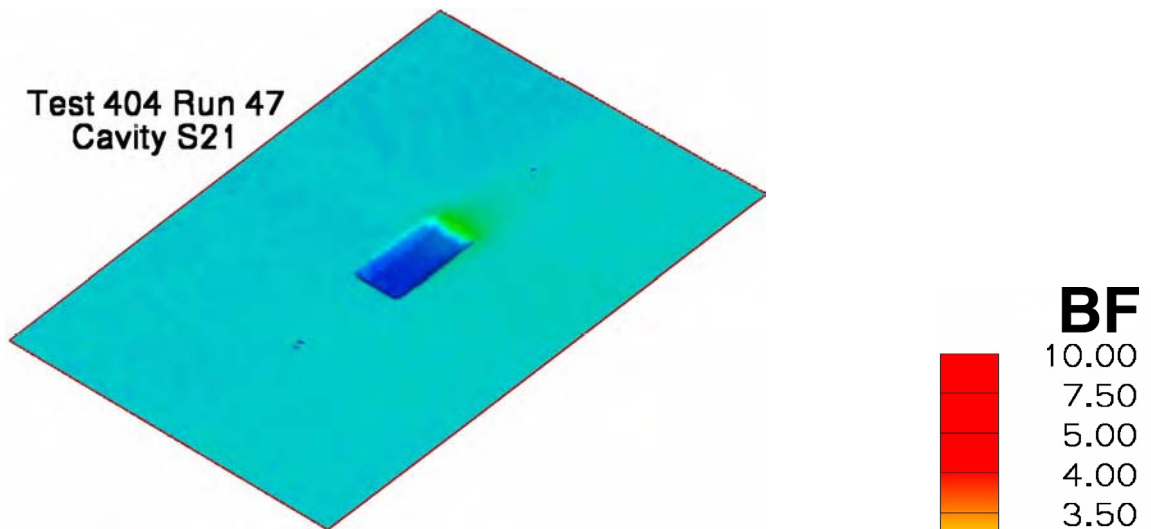
i) Test 404 Run 47 - H/δ=0.610.

Figure 14.- Concluded.
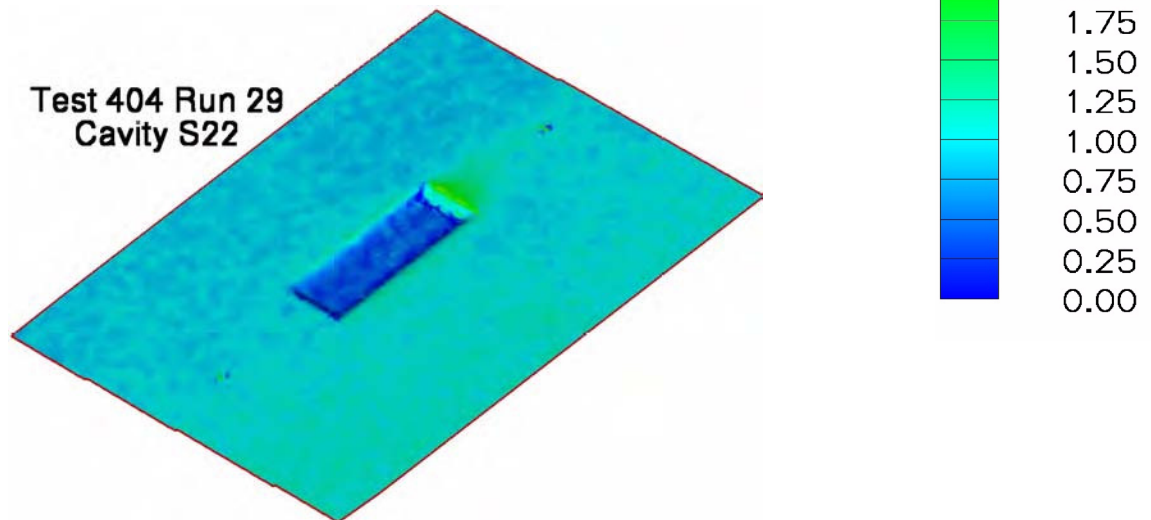
a) Test 404 Run 29 - H/δ=0.381.

**Figure 15.- Bump Factor images for Cavity S22 -
L/H=10.7, W/H=3.74.**
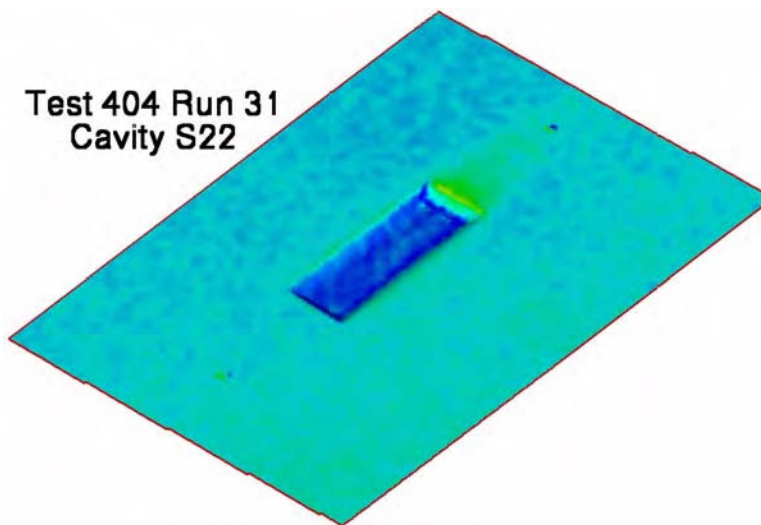
b) Test 404 Run 31 -H/δ=0.418.

Figure 15.- Continued.
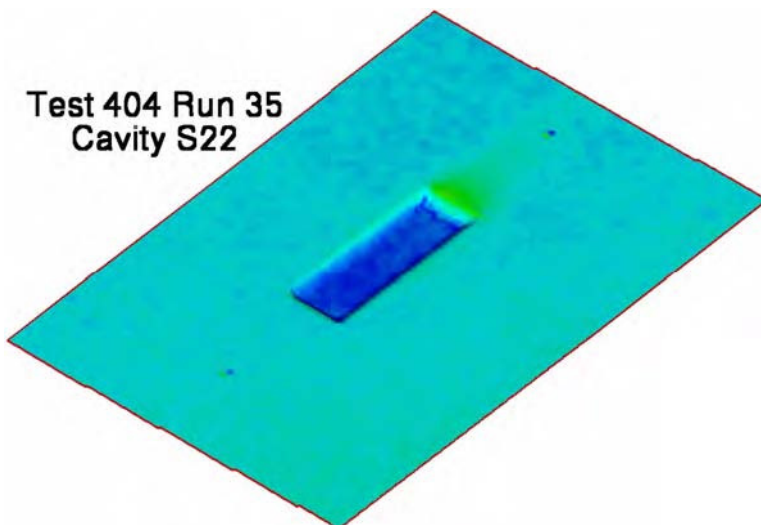
c) Test 404 Run 35 - H/δ=0.551.

Figure 15.- Continued.
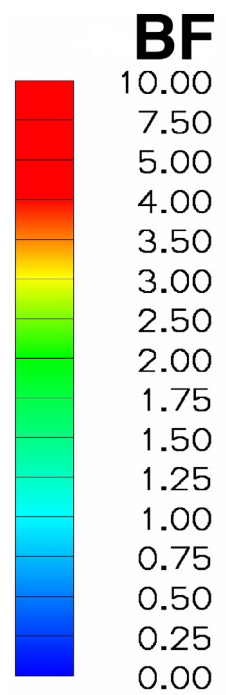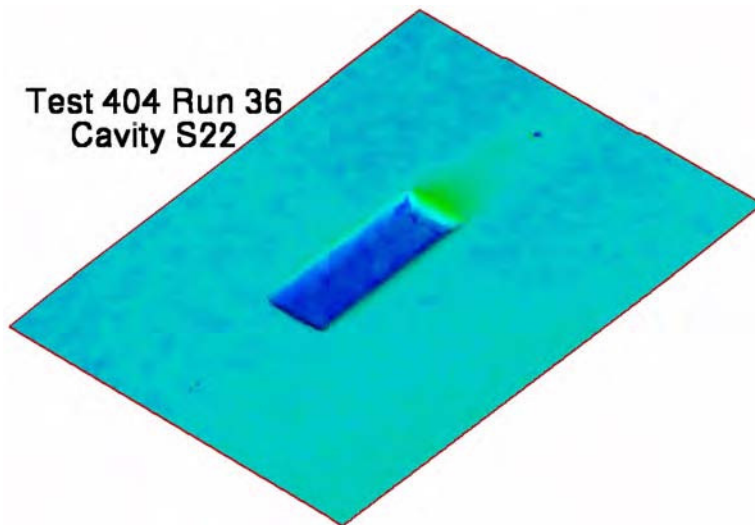
d) Test 404 Run 36 - H/δ=0.491.

Figure 15.- Continued.
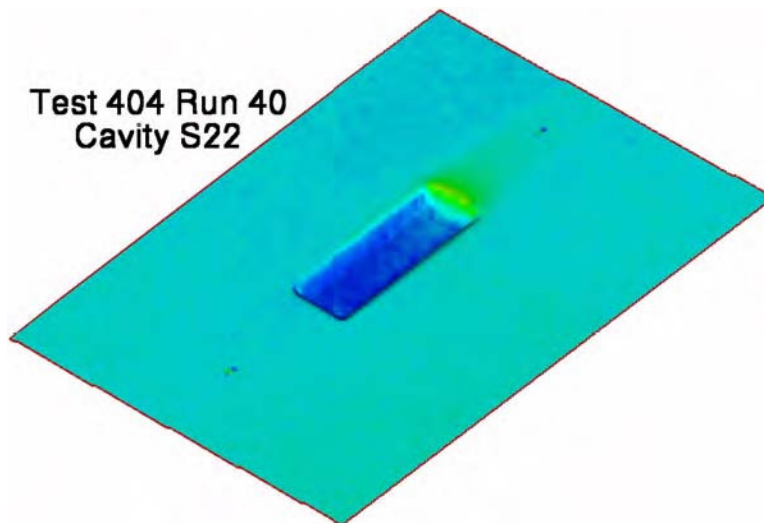
e) Test 404 Run 40 - H/δ=0.742.

Figure 15.- Continued.
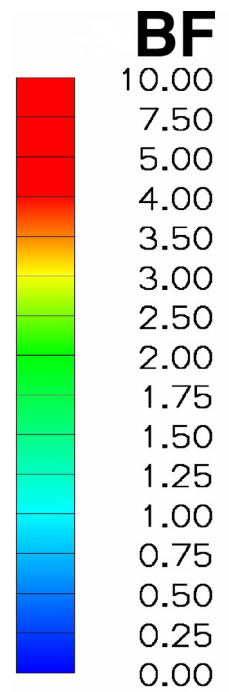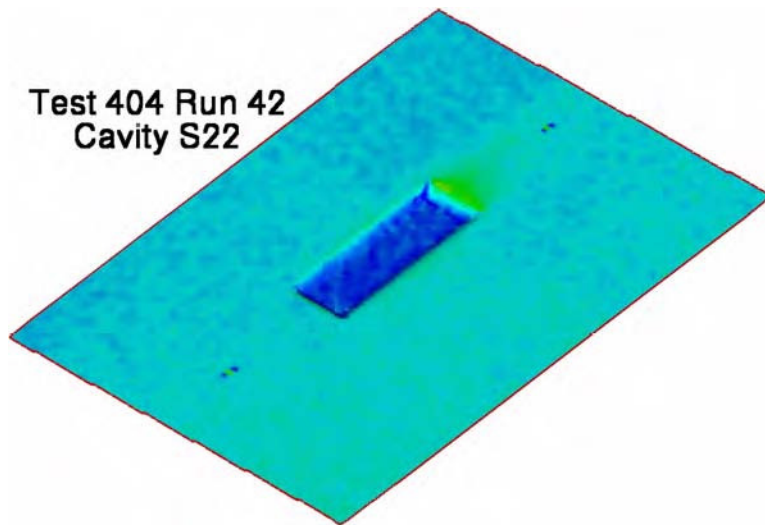
f) Test 404 Run 42 - H/δ=0.456.

Figure 15.- Continued.
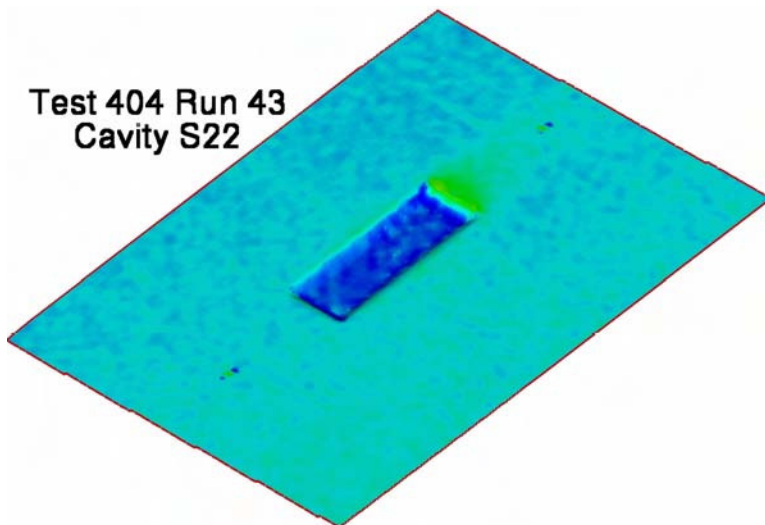
g) Test 404 Run 43 - H/δ=0.493.

Figure 15.- Continued.
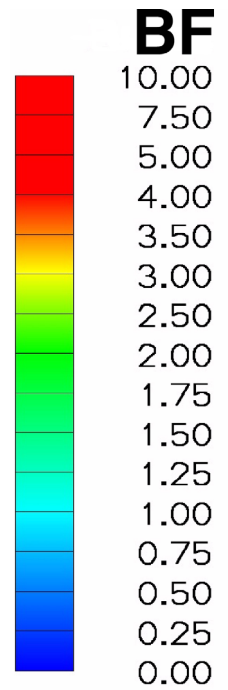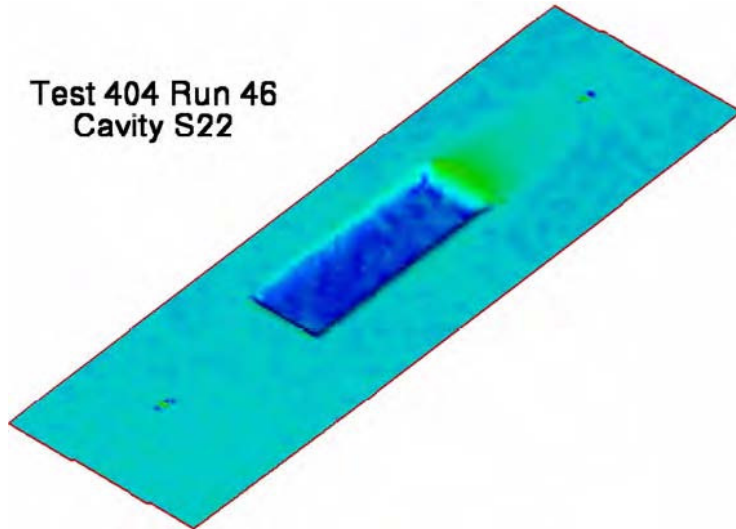
h) Test 404 Run 46 - H/δ=0.593.

Figure 15.- Continued.
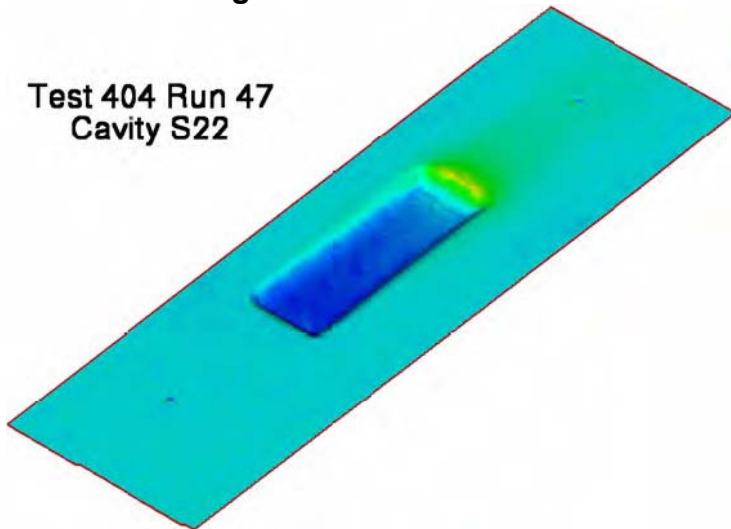
i) Test 404 Run 47 - H/δ=0.664.

Figure 15.- Concluded.
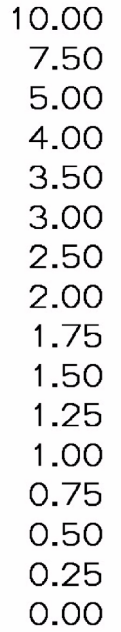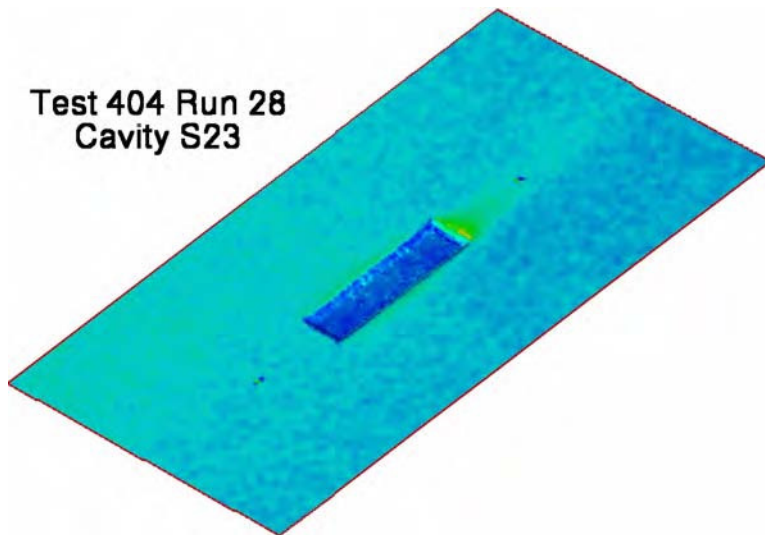
a) Test 404 Run 28 - H/δ=0.365.

Figure 16.- Bump Factor images for Cavity S23 - L/H=15.0, W/H=3.92.
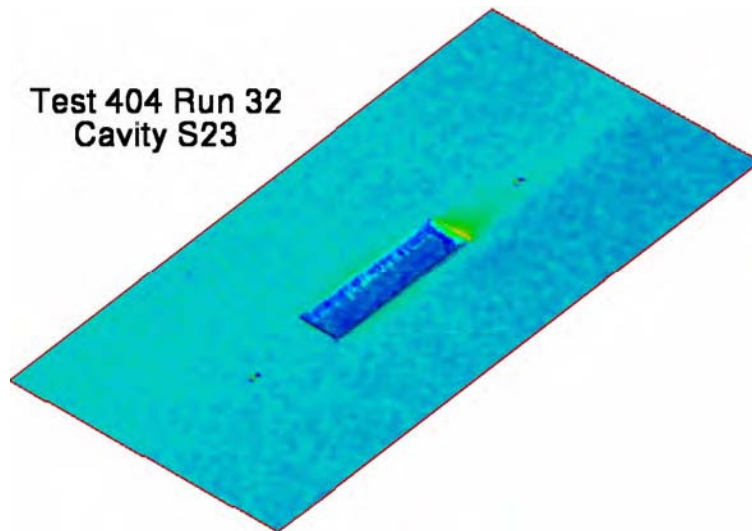
b) Test 404 Run 32 - H/δ=0.529.

Figure 16.- Continued.
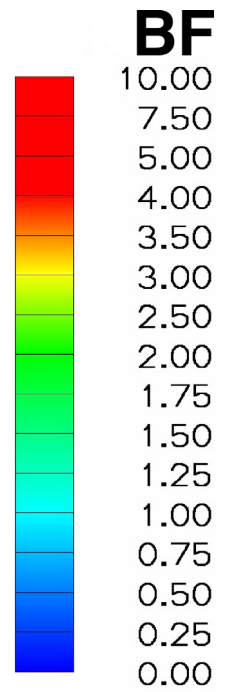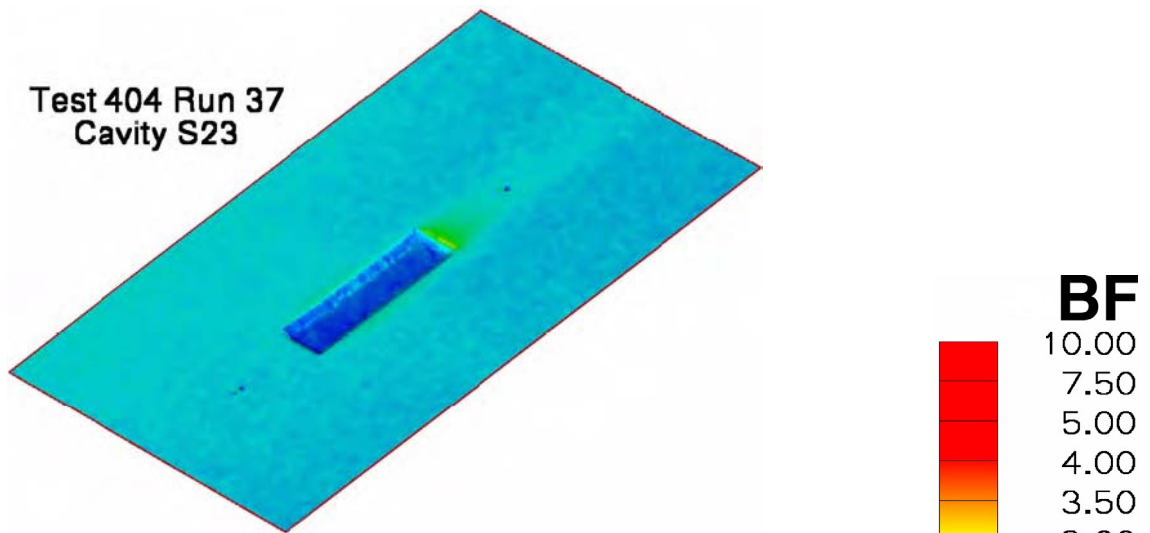
c) Test 404 Run 37 - H/δ=0.472.

Figure 16.- Continued.
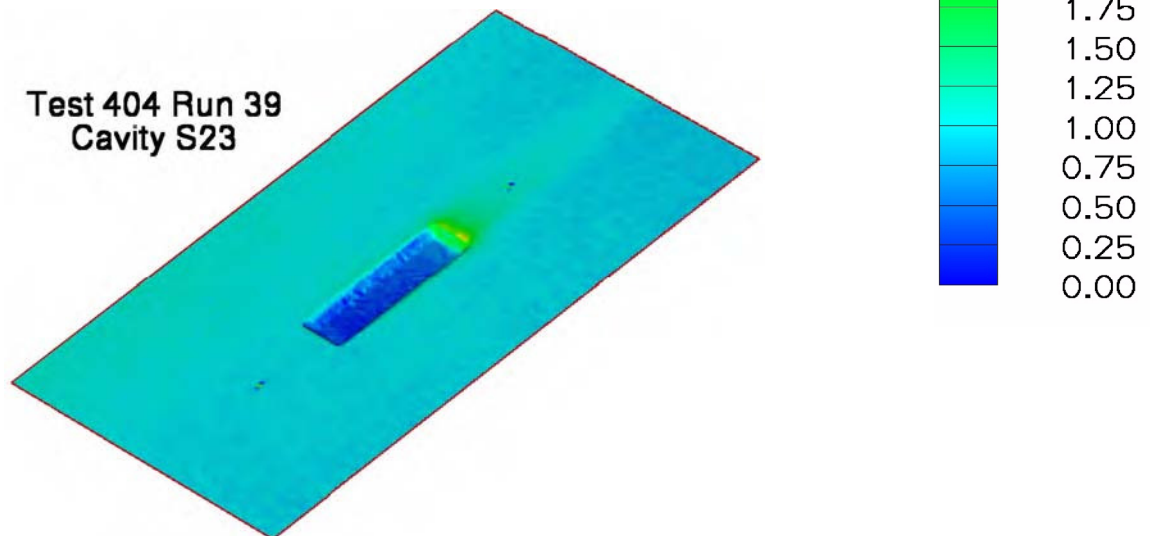
d) Test 404 Run 39 - H/δ=0.711.

Figure 16.- Continued.

64
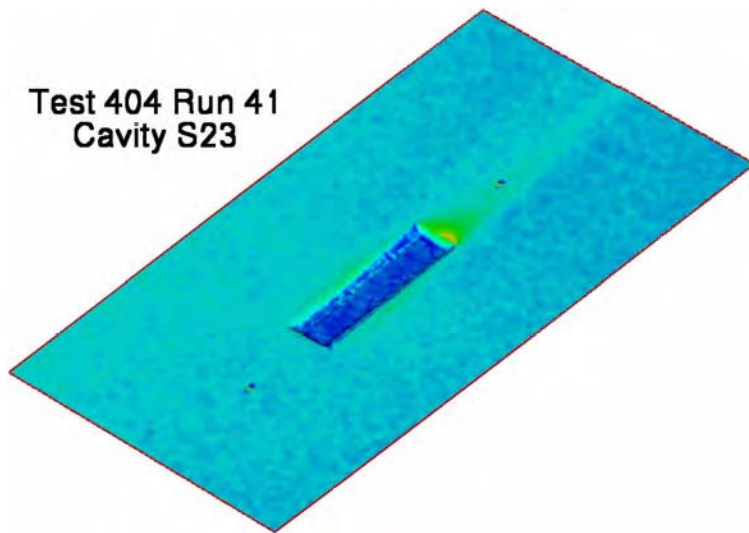
e) Test 404 Run 41 - H/δ=0.437.

Figure 16.- Continued.
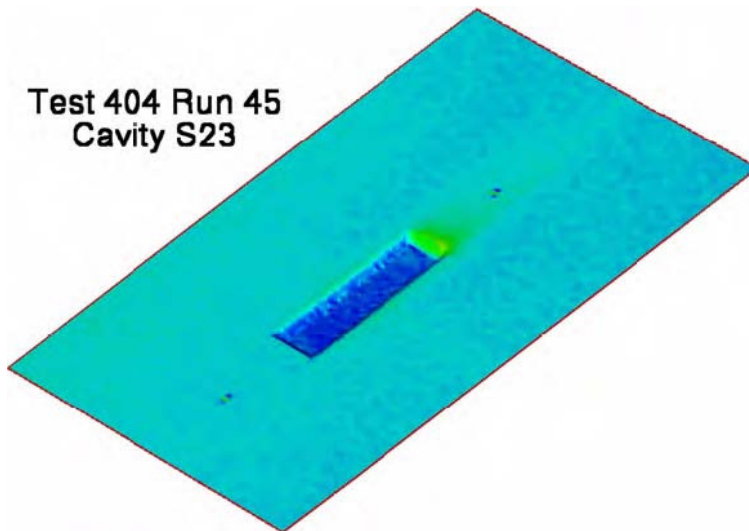
f) Test 404 Run 45 - H/δ=0.569.

Figure 16.- Continued.
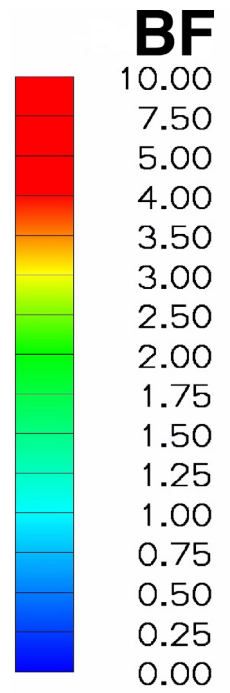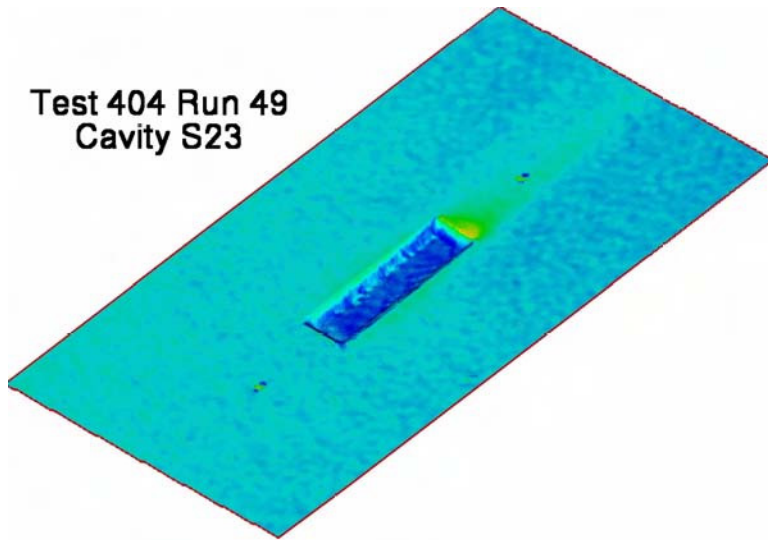
g) Test 404 Run 49 - H/δ=0.753.

Figure 16.- Concluded.
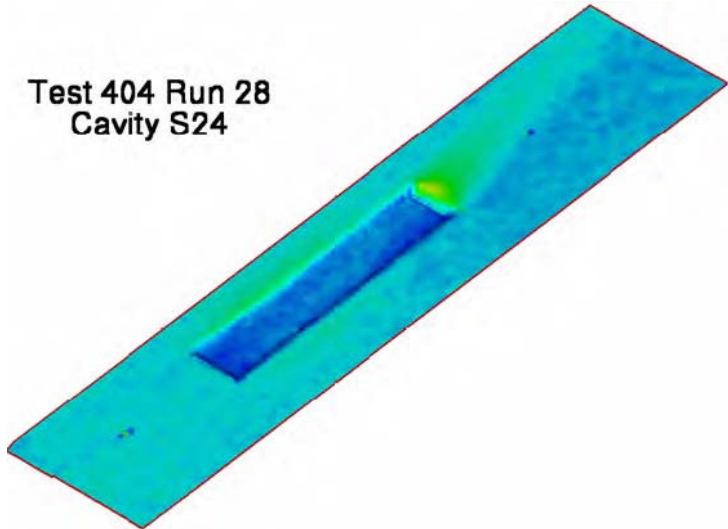
a) Test 404 Run 28 - H/δ=0.345.

**Figure 17.- Bump Factor images for Cavity S24 -
L/H=20.3, W/H=4.21**.
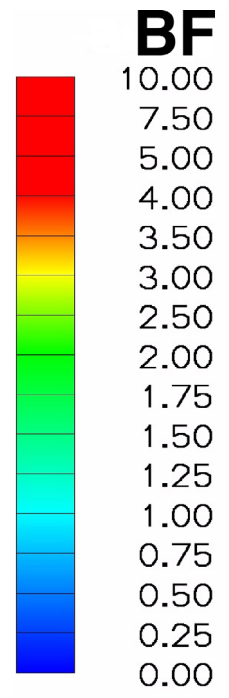
Test 404 Run 32
Cavity S24
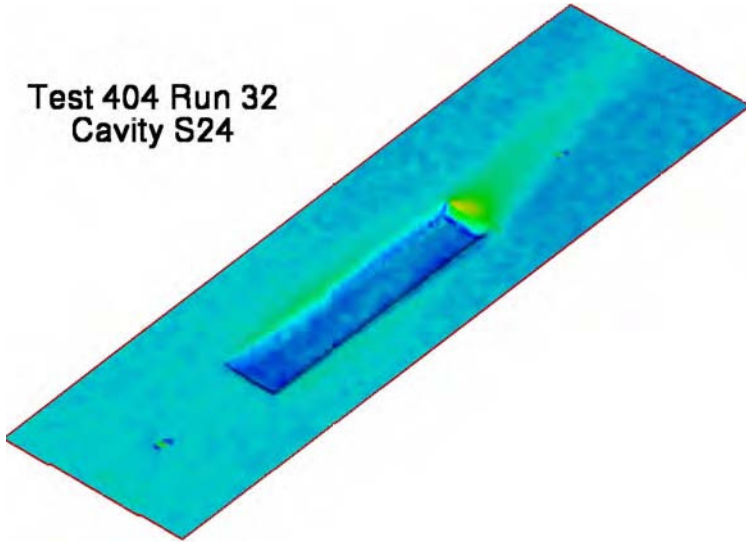
b) Test 404 Run 32 - H/δ=0.298.

Figure 17.- Continued.
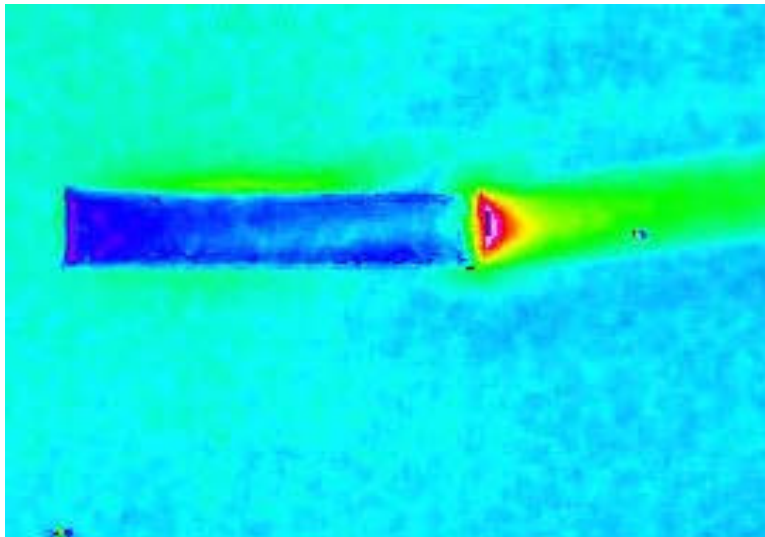
c) Test 404 Run 34 - H/δ=0.403.

Figure 17.- Continued.

BF

10.00
7.50
5.00
4.00
3.50
3.00
2.50
2.00
1.75
1.50
1.25
1.00
0.75
0.50
0.25
0.00
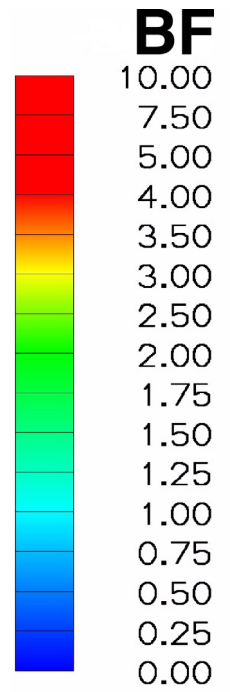
d) Test 404 Run 37 – H/δ=0.472.

Figure 17.- Continued.

e) Test 404 Run 39 - H/δ=0.671.

Figure 17.- Continued.
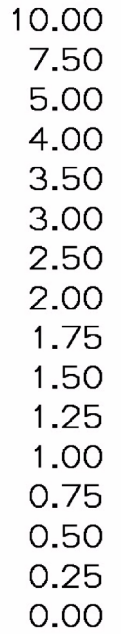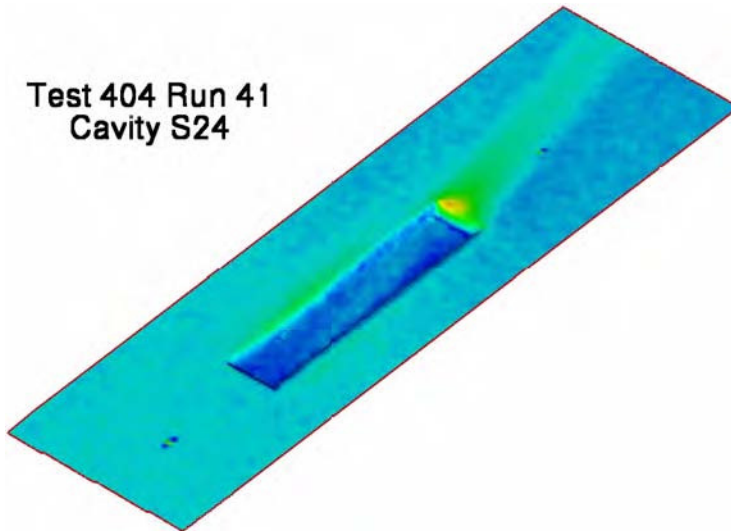
f) Test 404 Run 41 - H/δ=0.413.

Figure 17.- Continued.

g) Test 404 Run 45 - H/δ=0.537.

Figure 17.- Continued.
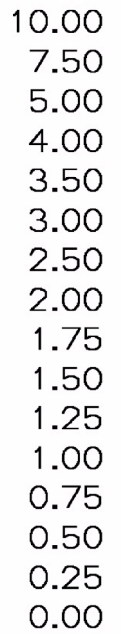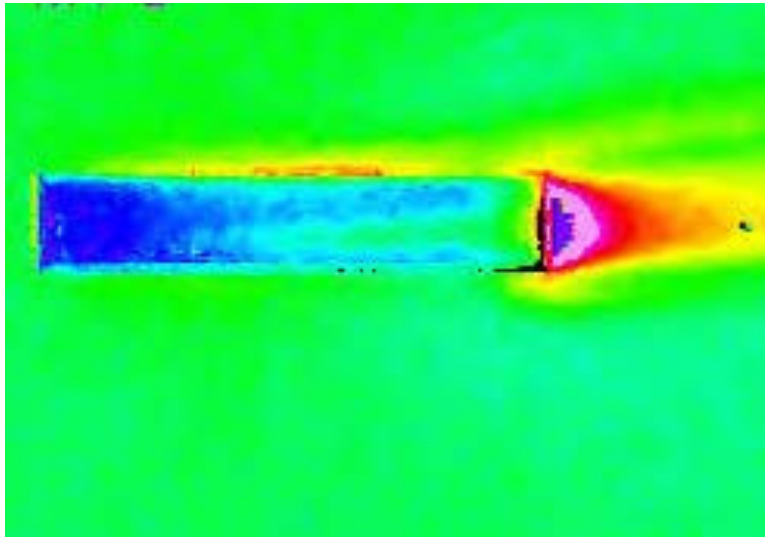
h) Test 404 Run 48 - H/δ=0.458.

Figure 17.- Continued.

Test 404 Run 49
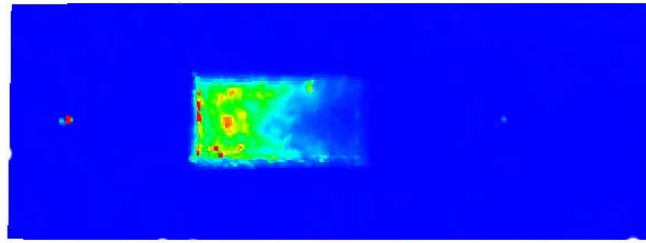Cavity S24
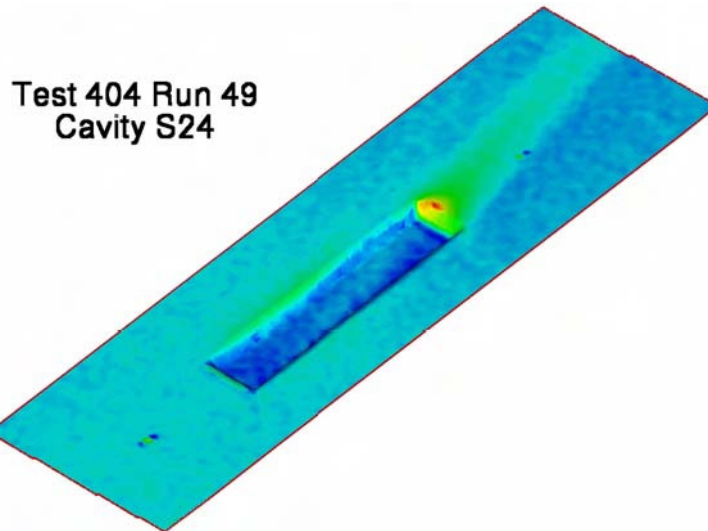
i) Test 404 Run 49 - H/δ=0.711.

Figure 17.- Concluded.

BF
10.00
7.50
5.00
4.00
3.50
3.00
2.50
2.00
1.75
1.50
1.25
1.00
0.75
0.50
0.25
0.00

UNCERTAINTY: 0.0   0.02   0.04   0.06   0.08   0.10

a) Bias uncertainties (% Uncertainty/100).

UNCERTAINTY: 0.0   0.04   0.08   0.12   0.16   0.20

b) Total uncertainties (% Uncertainty/100).

Figure 18.- Bump Factor uncertainties for Cavity S12 - Run 03 -
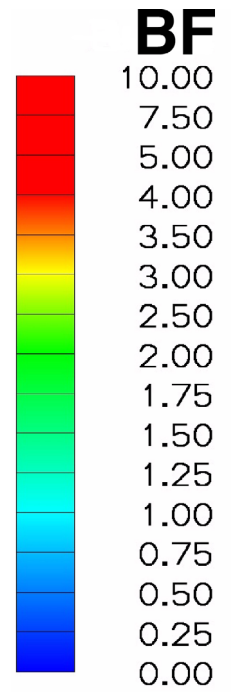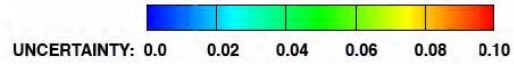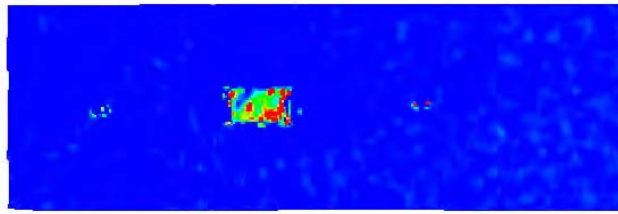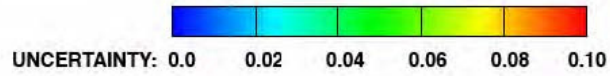
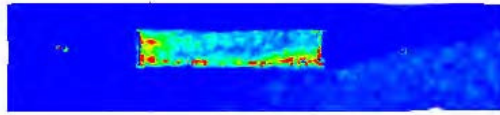**L/H=9.3, W/H=4.58, H/δ=0.185.**
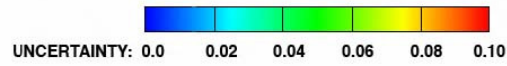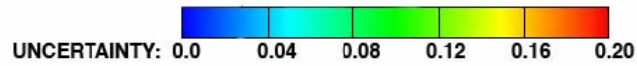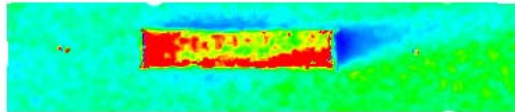
a) Bias uncertainties (% Uncertainty/100).
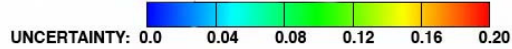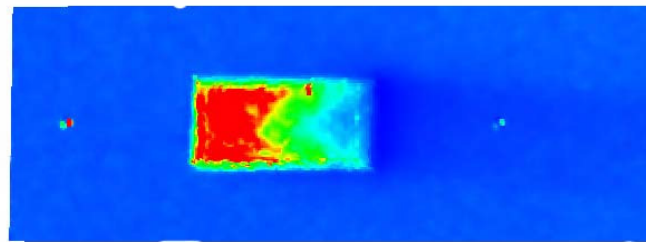
b) Total uncertainties (% Uncertainty/100).

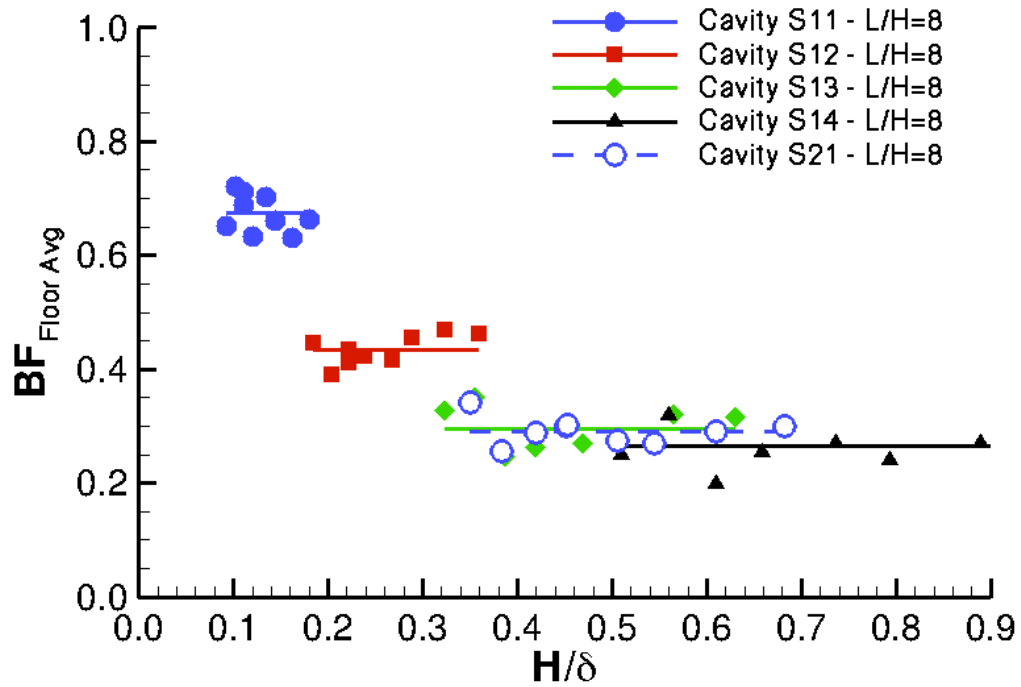**Figure 19.- Bump Factor uncertainties for cavity S14 - Run 16 - L/H=8.1, W/H=3.95, H/δ=0.992.**

UNCERTAINTY: 0.0   0.02   0.04   0.06   0.08   0.10

a) Bias uncertainties (% Uncertainty/100).

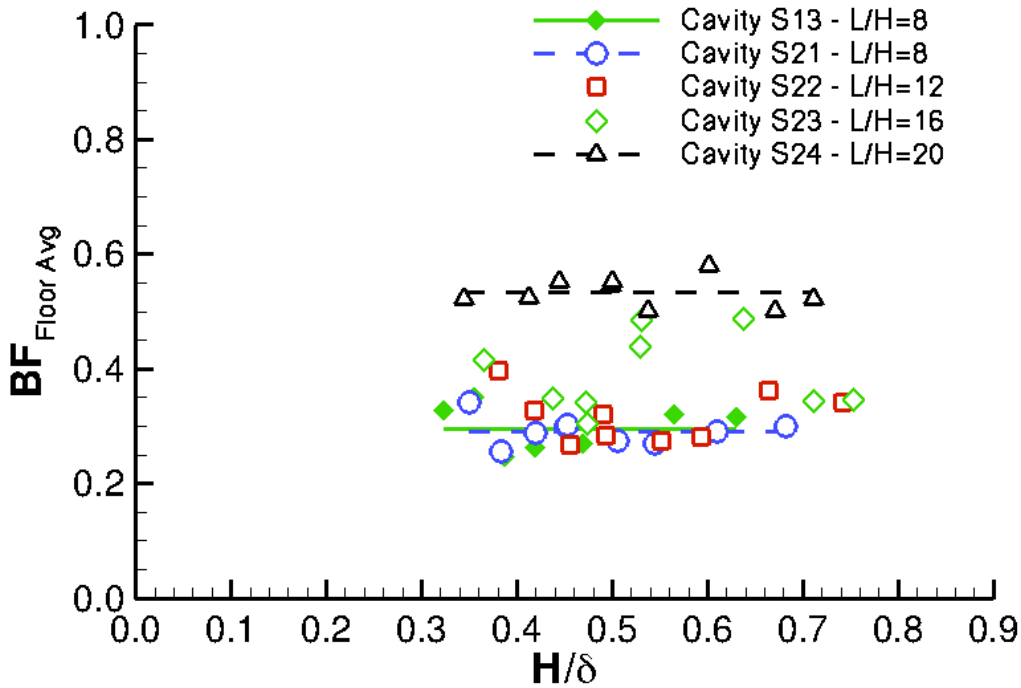UNCERTAINTY: 0.0   0.04   0.08   0.12   0.16   0.20

b) Total uncertainties (% Uncertainty/100).

Figure 20.- Bump Factor uncertainties for cavity S24 - Run 28 - L/H=20.3, W/H=4.21, H/δ=0.345.

a) Open Cavities - Depth Effect.

b) Closed Cavities - Length Effect.

Figure 21.- Variation of Average Bump Factor on cavity floor with H/δ.
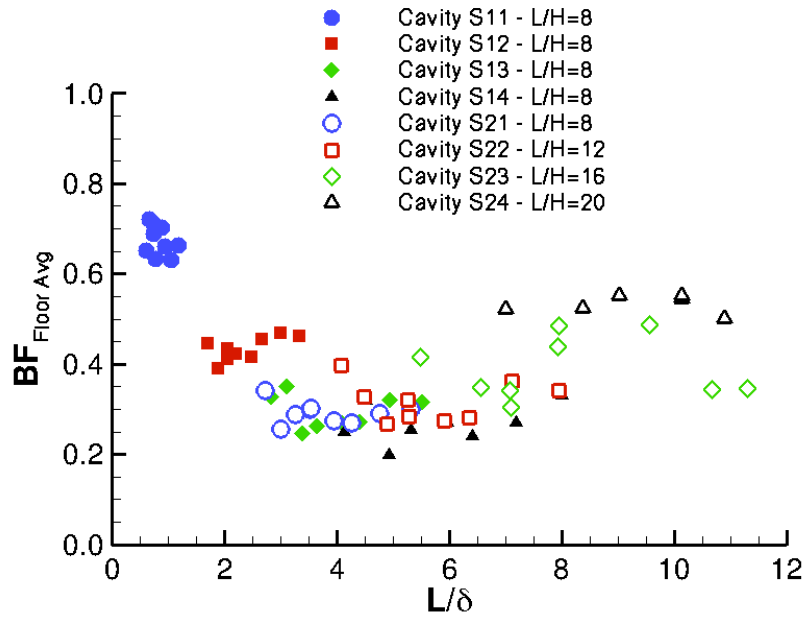
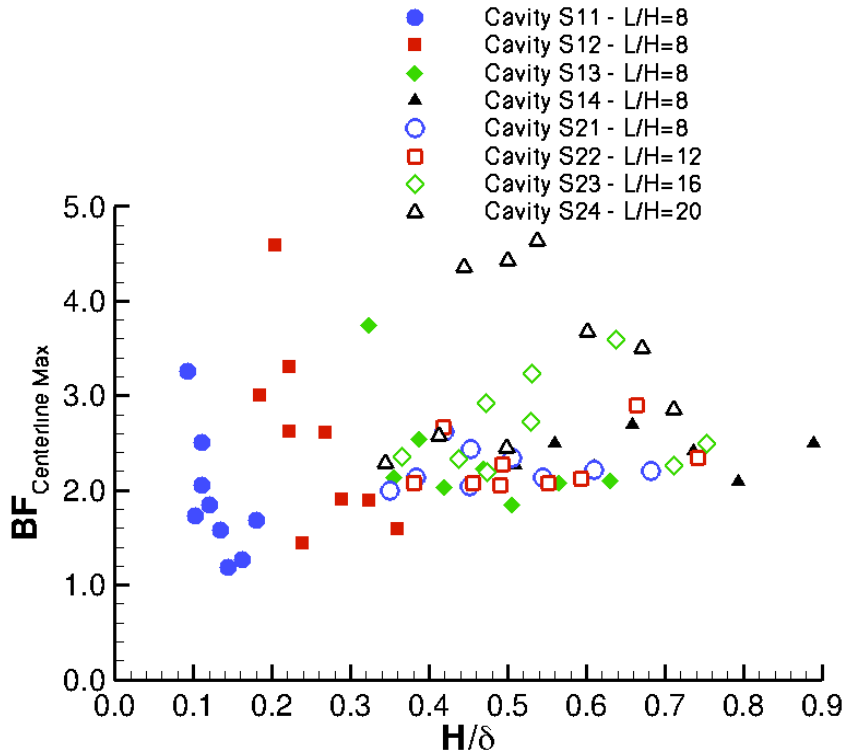**Figure 22.- Variation of Average Bump Factor on cavity floor with L/δ.**

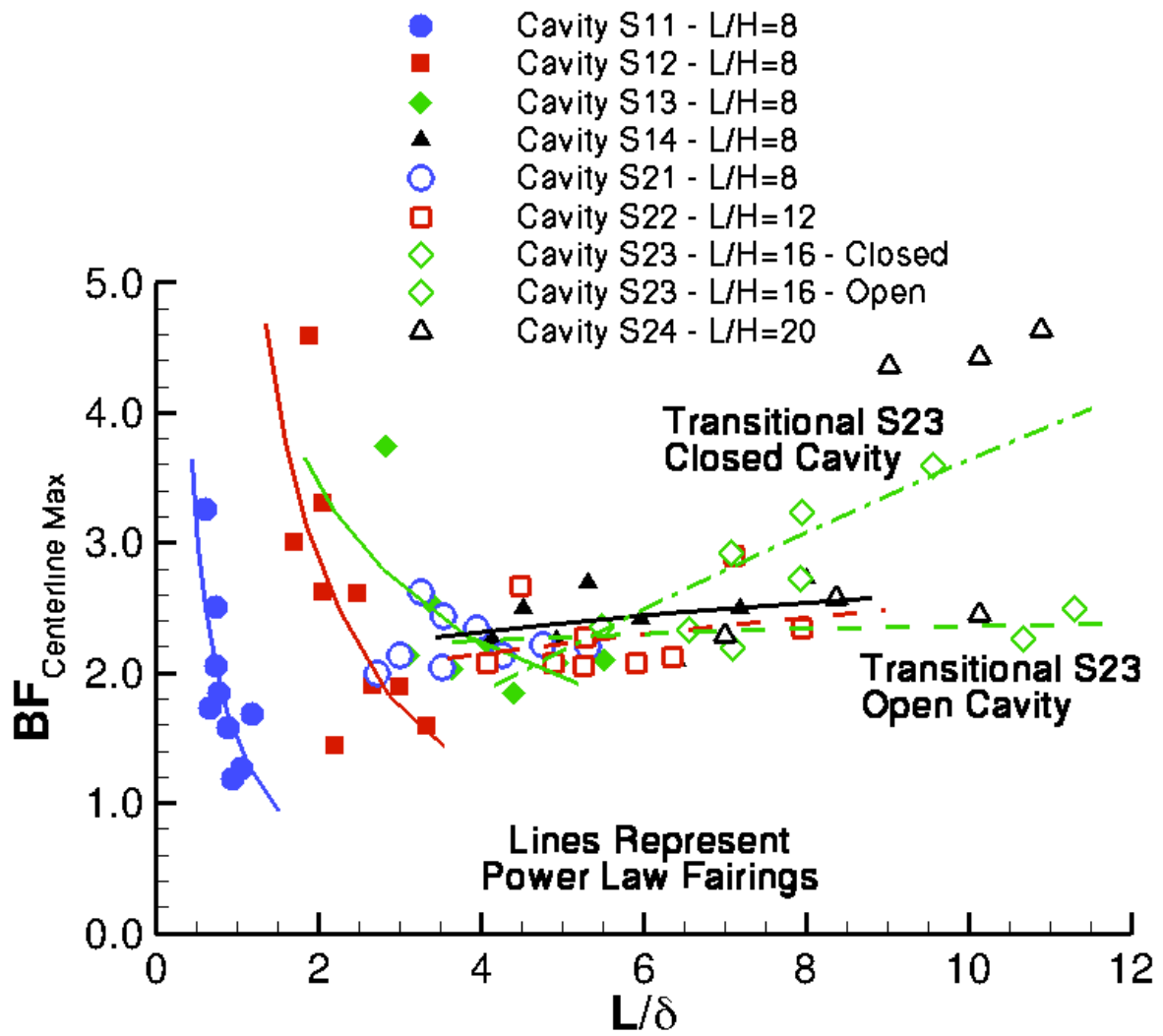**Figure 23.- Variation of maximum centerline endwall Bump Factor with H/δ.**

Figure 24.- Variation of maximum centerline endwall Bump Factor with L/δ.

REPORT DOCUMENTATION PAGE		*Form Approved* *OMB No. 0704-0188*

The public reporting burden for this collection of information is estimated to average 1 hour per response, including the time for reviewing instructions, searching existing data sources, gathering and maintaining the data needed, and completing and reviewing the collection of information. Send comments regarding this burden estimate or any other aspect of this collection of information, including suggestions for reducing this burden, to Department of Defense, Washington Headquarters Services, Directorate for Information Operations and Reports (0704-0188), 1215 Jefferson Davis Highway, Suite 1204, Arlington, VA 22202-4302. Respondents should be aware that notwithstanding any other provision of law, no person shall be subject to any penalty for failing to comply with a collection of information if it does not display a currently valid OMB control number.
PLEASE DO NOT RETURN YOUR FORM TO THE ABOVE ADDRESS.

1. REPORT DATE *(DD-MM-YYYY)* 01-09-2010	2. REPORT TYPE Technical Memorandum	3. DATES COVERED *(From - To)*

4. TITLE AND SUBTITLE Aero-Heating of Shallow Cavities in Hypersonic Freestream Flow	5a. CONTRACT NUMBER
	5b. GRANT NUMBER
	5c. PROGRAM ELEMENT NUMBER

6. AUTHOR(S) Everhart, Joel L.; Berger, Karen T.; Merski, N. Ronald, Jr.; Wood, William A.; Hollingsworth, Kevin E.; Hyatt, Andrew J.; Prabhu, Ramadas K.	5d. PROJECT NUMBER
	5e. TASK NUMBER
	5f. WORK UNIT NUMBER 432938.11.01.07.43.05.01

7. PERFORMING ORGANIZATION NAME(S) AND ADDRESS(ES) NASA Langley Research Center Hampton, VA 23681-2199	8. PERFORMING ORGANIZATION REPORT NUMBER L-19874

9. SPONSORING/MONITORING AGENCY NAME(S) AND ADDRESS(ES) National Aeronautics and Space Administration Washington, DC 20546-0001	10. SPONSOR/MONITOR'S ACRONYM(S) NASA
	11. SPONSOR/MONITOR'S REPORT NUMBER(S) NASA/TM-2010-216846

12. DISTRIBUTION/AVAILABILITY STATEMENT
Unclassified - Unlimited
Subject Category 34
Availability: NASA CASI (443) 757-5802

13. SUPPLEMENTARY NOTES

14. ABSTRACT

The purpose of these experiments and analysis was to augment the heating database and tools used for assessment of impact-induced shallow-cavity damage to the thermal protection system of the Space Shuttle Orbiter. The effect of length and depth on the local heating disturbance of rectangular cavities tested at hypersonic freestream conditions has been globally assessed using the two-color phosphor thermography method. These rapid-response experiments were conducted in the Langley 31-Inch Mach 10 Tunnel and were initiated immediately prior to the launch of STS-114, the initial flight in the Space Shuttle Return-To-Flight Program, and continued during the first week of the mission.

15. SUBJECT TERMS
Thermal protection; Space Shuttle; Heating; Laminar flow; Impact damage

16. SECURITY CLASSIFICATION OF:			17. LIMITATION OF ABSTRACT	18. NUMBER OF PAGES	19a. NAME OF RESPONSIBLE PERSON STI Help Desk (email: help@sti.nasa.gov)
a. REPORT	b. ABSTRACT	c. THIS PAGE			19b. TELEPHONE NUMBER *(Include area code)*
U	U	U	UU	83	(443) 757-5802

Standard Form 298 (Rev. 8-98)
Prescribed by ANSI Std. Z39.18